

2016 | Faculty of Sciences

DOCTORAL DISSERTATION

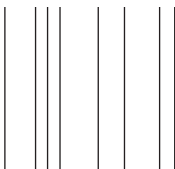
# Model development for image analysis in second harmonic imaging microscopy

Doctoral dissertation submitted to obtain the degree of  
Doctor of Science: Physics, to be defended by

**Rik Paesen**

Promoter: Prof. Dr Marcel Ameloot

Co-promoter: Prof. Dr Dominique Hansen



D/2016/2451/8



---

### **Members of the Jury**

Chair

Prof. Dr M. Ameloot, Hasselt University, Belgium, Promotor

Prof. Dr D. Hansen, Hasselt University, Belgium, Co-promotor

Prof. Dr I. Lambrechts, Hasselt University, Belgium

Prof. Dr B. Brône, Hasselt University, Belgium

Prof. Dr B. Cleuren, Hasselt University, Belgium

Prof. Dr T. Verbiest, KULeuven, Belgium

Dr M.C. Schanne-Klein, Ecole Polytechnique, France

Dr O. Nadyarnykh, VU University Amsterdam, Netherlands



---

*To Oscar*

---

---

---

## Table of contents

<b>1</b>	<b>Introduction</b>	<b>1</b>
1.1	Microscopy . . . . .	2
1.1.1	Fluorescence confocal laser scanning microscopy . . . . .	2
1.1.2	Two-photon microscopy . . . . .	3
1.1.3	SHG microscopy . . . . .	4
1.2	From quantum physics to biology . . . . .	6
1.2.1	A handful of biological structures . . . . .	6
1.2.2	Label free . . . . .	7
1.2.3	Coherent scattering . . . . .	8
1.3	Thesis guide . . . . .	10
<b>2</b>	<b>General theory</b>	<b>13</b>
2.1	Second harmonic generation . . . . .	14
2.1.1	Formalism . . . . .	14
2.1.2	Wave equation . . . . .	15
2.2	Plane wave . . . . .	17
2.2.1	Backward/Forward SHG . . . . .	17
2.2.2	Phase matching . . . . .	19
2.3	Focused Gaussian beam . . . . .	20
2.3.1	Point spread function . . . . .	20
2.3.2	Gouy phase shift . . . . .	21
2.3.3	Numerical aperture considerations . . . . .	23
2.3.4	Gaussian beam SHG . . . . .	24
2.3.5	SHG as a rare process . . . . .	26
2.4	Polarization SHG . . . . .	28
2.4.1	Polarization dependent intensity pattern . . . . .	28
2.4.2	Helical pitch angle . . . . .	31
<b>3</b>	<b>Instrumentation</b>	<b>33</b>
3.1	Microscope system . . . . .	34
3.2	Condenser properties . . . . .	37
3.3	Polarization controller . . . . .	40
3.3.1	Output polarization . . . . .	40
3.3.2	Technical notes . . . . .	42
3.3.3	Validation experiment . . . . .	43
3.4	Noise definition . . . . .	46

---

---

<b>4</b>	<b>Polarization second harmonic generation by image correlation spectroscopy on collagen type I hydrogels</b>	<b>49</b>
4.1	Abstract . . . . .	50
4.2	Introduction . . . . .	51
4.3	Calculations and Modelling . . . . .	53
4.3.1	Simulation framework . . . . .	53
4.3.2	Autocorrelation function . . . . .	53
4.3.3	ACF amplitude . . . . .	55
4.4	Materials and methods . . . . .	57
4.4.1	Hydrogel . . . . .	57
4.4.2	Microscopy . . . . .	57
4.4.3	Simulations . . . . .	57
4.4.4	Analysis . . . . .	58
4.4.5	Point spread function . . . . .	58
4.5	Results . . . . .	59
4.5.1	ACF shape particularities . . . . .	59
4.5.2	Evaluation of parameter recovery by simulations . . . . .	59
4.5.3	Dilution series . . . . .	61
4.6	Discussion . . . . .	65
4.6.1	Addendum . . . . .	66
4.7	Conclusion . . . . .	67
4.8	Acknowledgements . . . . .	68
4.9	Supplementary material . . . . .	69
4.9.1	Correlation amplitude correction due to intensity modulation . . . . .	69
4.9.2	Autocorrelation amplitude for a collagen type I hydrogel . . . . .	69
4.9.3	Model overview . . . . .	71
4.9.4	Coordinate system . . . . .	71
<b>5</b>	<b>On the interpretation of second harmonic generation intensity profiles of striated muscle</b>	<b>73</b>
5.1	abstract . . . . .	74
5.2	Introduction . . . . .	75
5.3	Materials and methods . . . . .	78
5.3.1	Tissue preparation . . . . .	78
5.3.2	Microscopy . . . . .	78
5.3.3	Point spread function . . . . .	78
5.3.4	Sarcomere profile analysis . . . . .	79
5.3.5	Simulations . . . . .	79
5.3.6	The supra-molecular model . . . . .	79
5.4	Results . . . . .	82
5.4.1	Dispersion . . . . .	82
5.4.2	Tight focussing . . . . .	82

---

---

5.4.3	Myosin density distribution . . . . .	84
5.5	Discussion . . . . .	87
5.6	Conclusions . . . . .	91
<b>6</b>	<b>Fully automated muscle quality assessment by Gabor filtering of SHG images</b>	<b>93</b>
6.1	abstract . . . . .	94
6.2	Introduction . . . . .	95
6.3	Materials and methods . . . . .	97
6.3.1	EAE Rat model . . . . .	97
6.3.2	Tissue preparation . . . . .	97
6.3.3	Microscopy . . . . .	97
6.3.4	Sarcomere profile analysis . . . . .	98
6.3.5	Gabor analysis . . . . .	98
6.3.6	Simulations . . . . .	102
6.3.7	Statistics . . . . .	102
6.4	Results . . . . .	104
6.4.1	Typical patterns and their Gabor values . . . . .	104
6.4.2	Gabor value correlates with myosin disorder . . . . .	106
6.4.3	EAE affects sarcomere integrity . . . . .	107
6.5	Discussion and conclusions . . . . .	109
<b>7</b>	<b>Sarcomere second harmonic generation intensity profile depends on sample thickness</b>	<b>113</b>
7.1	Abstract . . . . .	114
7.2	Introduction . . . . .	115
7.3	Methods and material . . . . .	117
7.3.1	Sample preparation . . . . .	117
7.3.2	Microscopy . . . . .	117
7.3.3	Simulations . . . . .	118
7.4	Results . . . . .	120
7.4.1	Simulations of thickness dependence and edge effects . . . . .	120
7.4.2	Experimental verification of slice thickness . . . . .	120
7.5	Discussion and conclusions . . . . .	123
<b>8</b>	<b>General discussion, conclusions and outlook</b>	<b>127</b>
8.1	General considerations . . . . .	128
8.2	Collagen hydrogels . . . . .	129
8.3	Muscle tissue . . . . .	132
8.3.1	Filament lengths . . . . .	132
8.3.2	Muscle degradation assessment . . . . .	134
8.3.3	Point spread function . . . . .	136

---

---

8.4 Far field emission profile imaging . . . . .	137
<b>Reference list</b>	<b>139</b>
<b>Samenvatting</b>	<b>153</b>
<b>Scientific output</b>	<b>157</b>
<b>Dankwoord</b>	<b>161</b>

---

## List of abbreviations

ACF	Auto Correlation Function
BP	Band Pass
CLSM	Confocal Laser Scanning Microscope
EAE	Experimental Autoimmune Encephalomyelitis
EM	Electron Microscopy
FWHM	Full Width at Half Maximum
HRS	Hyper Rayleigh Scattering
ICS	Image Correlation Spectroscopy
IHC	Immuno-histochemical
IR	Infra Red
LCP	Left Circularly Polarized
LP	Long Pass
NA	Numerical Aperture
NDD	Non-Descanned Detection
P-SHG	Polarization Second Harmonic Generation
PBS	Phosphate Buffered Saline
PFA	Para-Formaldehyde
PMT	Photo Multiplier Tube
PSF	Point Spread Function
RCP	Right Circularly Polarized
RI	Refractive Index
SHG	Second Harmonic Generation
SNR	Signal-to-Noise Ratio
SOD	Second Order Derivative
TPEF	Two-Photon Excited Fluorescence
UV	Ultra Violet

---

## List of symbols

$E_0$	Electric field amplitude
$I$	Intensity
$\beta$	First order hyperpolarizability
$\chi^{(2)}$	Second order susceptibility
$\epsilon_0$	Vacuum permittivity
$\lambda$	Wavelength
$\mathcal{P}$	Radiation power
$\omega$	Electromagnetic wave angular frequency
$\vec{E}$	Electric field
$\vec{P}$	Polarization field
$\vec{k}$	Wave vector
$\zeta$	Gouy phase shift
$c$	Speed of light
$d$	Second order susceptibility, contracted notation
$k$	Wave number
$n$	Refractive index
$w_0, w_{xy}$	Gaussian beam waist size
$w_z$	Gaussian beam axial waist size
$z_R$	Rayleigh range

# CHAPTER 1

---

## Introduction

---

This chapter is partially based on the following publications:

- De Meulenaere, E., **Paesen, R.**, Psilodimitrakopoulos, S., Ameloot, M., Loza-Alvarez, P., Vanderleyden, J. & Clays, K. Probing live samples in second-harmonic generation microscopy using specific markers and fluorescent proteins. *Proc. SPIE* **8226**, 82263C–82263C–9 (2012)
- De Meulenaere, E., Chen, W.-Q., Van Cleuvenbergen, S., Zheng, M.-L., Psilodimitrakopoulos, S., **Paesen, R.**, Taymans, J.-M., Ameloot, M., Vanderleyden, J., Loza-Alvarez, P., Duan, X.-M. & Clays, K. Molecular engineering of chromophores for combined second-harmonic and two-photon fluorescence in cellular imaging. *Chem. Sci.* **3**, 984–995 (4 2012)
- Martens, T. F., Vercauteren, D., Forier, K., Deschout, H., Remaut, K., **R. Paesen**, Ameloot, M., Engbersen, J. F., Demeester, J., De Smedt, S. C. & Braeckmans, K. Measuring the intravitreal mobility of nanomedicines with single-particle tracking microscopy. *Nanomedicine* **8**, 1955–1968 (2013)
- Bruneel, B., Mathä, M., **Paesen, R.**, Ameloot, M., Weninger, W. & Huyseunne, A. Imaging the Zebrafish Dentition: From Traditional Approaches to Emerging Technologies. *Zebrafish* **12**, 1–10 (2015)
- Glas, D., **R. Paesen**, Depuydt, D., Binnemans, K., Ameloot, M., De Vos, D. E. & Ameloot, R. Cellulose Amorphization by Swelling in Ionic Liquid/Water Mixtures: A Combined Macroscopic and Second-Harmonic Microscopy Study. *ChemSusChem* **8**, 82–86 (2014)
- Fanton, Y., Robic, B., Rummens, J.-L., Daniëls, A., Windmolders, S., Willems, L., Jamaer, L., Dubois, J., Bijnens, E., Heuts, N., Notelaers, K., **Paesen, R.**, Ameloot, M., Mees, U., Bito, V., Declercq, J., Hensen, K., Koninckx, R. & Hendrik, M. Cardiac atrial appendage stem cells engraft and differentiate into cardiomyocytes in vivo: A new tool for cardiac repair after MI. *Int. J. Cardiol.* **201**, 10–19 (2015)

## 1.1 Microscopy

Since the development of the 17th century first compound microscope, an optically magnifying device consisting of more than one lens, the microscope has been around and is known as one of the most applied devices in research. Biology was one of the first research areas to apply microscopy for studying micro-organism and obtaining detailed structural information of supra-molecular structures such as muscle fibers [1]. Early microscopes were solely based on the absorption and transmission of white (sun)light. Although transmission microscopes are convenient in resolving morphology on a micrometer scale, the viewed structures are only specific by their intrinsic optical density, leaving no choice to which structure should be visualized.

### 1.1.1 Fluorescence confocal laser scanning microscopy

It lasted until the 1940s to allow specific microscopic visualization by means of immuno-histochemical (IHC) staining. One of the first records on IHC staining was mentioning the use of a fluorescent probe [2]. Using fluorescent immunohistochemistry or immunofluorescence introduces two major leaps in microscopy. First, the fluorescent particles serve as light sources, providing a huge contrast with respect to its surrounding, similar to stars in the night sky. Secondly, by tagging fluorescent probes with specific antibodies, structures of interest can be visualized individually.

Ever since the hurdle of structure specific visualization has been tackled, the main concern of development in microscopy is related to getting the best resolution possible. Overcoming Abbe's fundamental resolution limit is not possible using standard optical configuration, but important improvements to image quality and resolution have been obtained by the development of confocal fluorescence microscopes. In this, a pinhole at the light source causes the sample to be only illuminated at a single point. Today, the combination of an isotropic light source (lamp) and illumination pinhole has been replaced by lasers. They allow for a plane wave illumination of the objective back aperture, resulting in optimal focusing to a diffraction limited illumination volume. Moreover, since the introduction of solid state lasers, a wide range of distinct wavelengths (laser lines) can be selected, making the illumination filter redundant.

Although the majority of the resulting signal comes from the diffraction limited focal volume originating from the focused laser, there is still a lot of background signal due to the focusing cone below and above (axially) the focal point. A second pinhole was introduced at the optically conjugate focal (confocal) plane at the detector site to reject any signal not coming from the focal plane. Besides a factor of about  $\sqrt{2}$  increase in resolution in the lateral direction [3], a major increase in the axial direction is obtained, making so-called optical sectioning feasible. There are two downsides of this approach, making confocal microscopy extremely slow compared to wide field microscopy. First, up to 85% of the fluorescence signal is rejected by the

pinhole, requiring high integration times to increase the signal-to-noise ratio. Second, only one point of the sample is illuminated and imaged at a time, so the entire sample can only be visualized by point-by-point scanning. This is typically done by scanning the laser instead of the sample, but requires an additional optical setting to de-scan the signal, such that it can pass the confocal pinhole correctly for each position on the sample. Despite the technical challenges and the unavoidable signal losses, the increased resolution and the ability of three-dimensional imaging by optical sectioning has made the confocal laser scanning microscope (CLSM) a highly desired tool, not only for biologist but also physicists, engineers and in medical environments.

### 1.1.2 Two-photon microscopy

Considering the excitation of a fluorescent dye as the transition from the ground quantum state ( $S_0$ ) to the first excited state ( $S_1$ ), a single photon with appropriate energy is said to be required to cause this transition (Fig. 1.1a). Many fluorescent probes have excitation wavelengths in the blue and ultra-violet (UV) range. In a biological context this is often undesired since high energy UV photons cause damage to cells, induce genetic mutations [4], and are heavily absorbed by water. Instead of using a single photon to excite a fluorophore, later developments in microscopy have made it possible to use two simultaneously arriving photons with half the energy required (Fig. 1.1b). This means wavelengths toward infra-red (IR) can be used to excite that exact same fluorescent probe. Since IR light is less absorbed and scattered by water, and thus biological features, incident photons penetrate deeper and damage is less likely to occur [5].

Similar to the previously introduced two-photon excited fluorescence (TPEF) microscopy, another interesting two-photon process is known to occur in certain biolog-

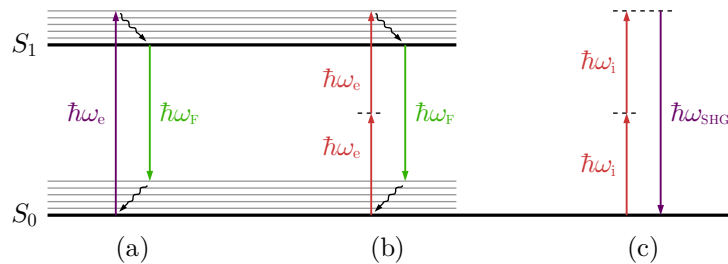


**Figure 1.1:** Jablonski diagram of (a) single photon excitation (regular) fluorescence, and (b) TPEF. In (c), a Jablonski like diagram of SHG is shown. The solid lines represent real energy levels, the dashed lines are virtual levels.  $\hbar$  is the reduced Planck constant,  $\omega_e$  is the frequency of the excitation wavelength,  $\omega_F$  that of the fluorescence emissions wavelength,  $\omega_i$  the frequency related to the illumination wavelength and  $\omega_{SHG}$  is the frequency related to the SHG wavelength.

ical structures: Second Harmonic Generation (SHG) (Fig. 1.1c). Instead of exciting a fluorophore, SHG relies on the loss-less transition from the ground state to a higher virtual state via an intermediate virtual state. When the system relaxes to the ground state, a photon with twice the energy, or half the wavelength of the incoming wave, is emitted. SHG strictly occurs in media which have no center of inversion symmetry, referred to as non-centrosymmetric [6]. This can be a bulk medium having a non-centrosymmetric crystal-like structure, a collection of ordered polar molecules or it can occur at an interface between two media [6]. In this work, we mainly study biological tissues which we consider as bulk non-centrosymmetric media, or as a collection of polar molecules. We will often refer to these SHG sources as non-linear scatterers, anharmonic scatterers or harmonophores.

Both TPEF and SHG are two-photon processes of which the occurrence is known to be very rare, which we shortly discuss later in section 2.3.5. The only way of increasing the probability of a two-photon process is increasing the instantaneous illumination intensity. This is achieved in two ways. First, laser light is temporally confined in ultra short pulses. Second, the light is spatially confined as much as possible. We previously mentioned that the latter typically occurs in a CLSM, making a laser scanning microscope the ideal device to perform multi-photon microscopy. Moreover, the scarceness of the two-photon processes makes the "C" in CLSM redundant. Only at the focal point of the focused illumination beam is the intensity sufficiently high to obtain detectable signals originating from two-photon processes. This yields an intrinsic confocal behavior without the use of confocal pinhole, and thereby avoiding the previously mentioned 85% signal rejection. Two-photon processes also make non-descanned imaging possible, not only excluding the complicated descanning optics, but also allowing for easy forward detection. This is of utmost importance when performing SHG microscopy of (semi)thick specimen. Due to the coherent nature of SHG, the strongest detectable signal are emitted in forward. We will elaborate on this in section 2.2.1.

Besides the temporal and spatial confinement of light, increasing the laser source power also yields higher probabilities for two-photon processes to occur. This is well known for single photon excitation fluorescence, for which a linear response is observed in the fluorescence signal when fluorophore concentrations are not too high. On the other hand, for two-photon process a quadratic increase is observed in the emitted signal intensity when linearly increasing the illumination power [6]. This feature can be used to test whether detected signals are originating from two-photon processes or not.

### 1.1.3 SHG microscopy

In this introduction, the development of SHG microscopy sounds like a coincidence, or a side effect of the more widely applicable TPEF. Even if it was so, SHG has found its way in biology, mainly enriching the field of biophysics. In the following

sections, we will discuss the circumstance in which SHG occurs and elaborate on the applicability of SHG in the context of biology and biomedical/biophysical research.

## 1.2 From quantum physics to biology

A nice historical overview of theoretical and experimental developments of two-photon processes in general is given in the book *Biomedical nonlinear optical microscopy* by Masters and So [5]. Briefly, the discussions on the existence of two-photon process such as SHG go back to before 1931, which is the year in which physics Nobel prize winner Maria Göpert-Mayer published her doctoral dissertation on the theory of two-photon quantum transitions [5]. It took until 1961 before the group of Franken experimentally proved the existence of SHG by irradiating a non-centrosymmetric quartz crystal with a pulsed ruby laser exhibiting electric fields of  $10^7$  V/m [7]. Biological specimen are prone to damage when illuminated by these extreme high fields. However, together with the development of femto-second pulsed lasers, allowing peak electric fields up to  $10^9$  V/m with low average power, advances in confocal scanning laser microscopy created the opportunity to use SHG as a novel tool to image and study biological structures.

### 1.2.1 A handful of biological structures

Due to the requirement of non-centrosymmetry, only a handful of biological structures are suitable for SHG imaging (Fig 1.3). Collagen type I and II (Fig. 1.3.a), the main proteins present in mammalian connective tissue, consists of highly ordered and tightly packed SHG active tropo-collagen, a coiled-coil triple  $\alpha$ -helix [8, 9]. Myosin (Fig. 1.3.b), a partially coiled-coil  $\alpha$ -helical structure, again tightly packed into ordered filaments [10], produces strong SHG signals and can for instance be use to verify the presence of newly synthesized sarcomeres [11]. Since sarcomeres are discussed extensively in this work, a typical EM-image of a sarcomere is shown in Fig. 1.2 as a reference.

Microtubules (Fig. 1.3.d), yet another structure characterized by its helical shape, produce detectable SHG signals, but only when tightly packed in for instance axons

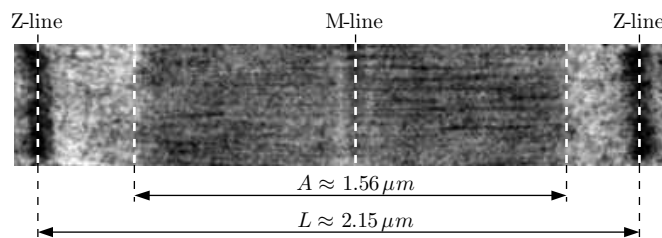


**Figure 1.2:** Typical EM image of a sarcomere with the indication of the Z-lines defining the sarcomere length  $L$ , and the myosin region known as the A-band indicated by  $A$ . Also the central M-line of M-region of the sarcomere is indicated. The sample was prepared as described in section 7.3.1 (in collaboration with prof. Ivo Lambrechts, UHasselt).

or mitotic spindles [12]. Also plant material is known to form helices on molecular level, resulting in SHG active structures. Amylopectin (Fig. 1.3.c) inside starch is one of them [13]. The starch can easily be extracted from a potato by sweeping a slice over a microscope cover glass, and often serves as an easy test sample to check the functioning of the SHG microscope. SHG arising from crystalline cellulose (Fig. 1.3.e) is for instance used to study its amorphization by means of an ionic liquid [14]. Two common factors appear to provide the minimal requirements for biological tissue to exhibit SHG activity: the individual molecules cannot exhibit a center of symmetry, which is typically related to their helical shape, and the molecules need to be highly ordered. Intuitively, the tight ordering can be considered to be of essence to induce constructive interference of individual harmonophores, yielding a strong and detectable SHG signal.

### 1.2.2 Label free

Visualizing specific structures without the addition of targeting labels is one of the main advantages of SHG microscopy of biological tissue. Because there are only a few endogenous sources, one can almost exclusively link the SHG signal to one of these sources using prior morphology knowledge of the imaged tissue or sample. Contrarily, contrast based SHG microscopy forces us to focus the study to only one SHG active structure of interest at a time, ruling out multiple source tissue such as muscle-tendon transitions. Nevertheless, the structures of interest can be studied in their most native form and environment, omitting often tedious and probably biasing sample preparation steps such as fixation and staining. SHG has therefore been used extensively to for instance study remodeling of collagen rich cancerous tissue in a non-invasive manner [15–19]. When sufficiently small, even whole and live organisms can be visualized and studied by SHG microscopy. Typically, roundworms or zebrafish (Fig. 1.3.b) are used to characterize for instance muscle tissue or tooth formation [13, 20].

Although it is not possible to spectroscopically distinguish SHG signals originating from different sources, other characteristic features of the SHG signal can be employed. In case of combined SHG and two-photon excited fluorescence with a spectroscopically overlapping dye, fluorescence lifetime imaging can be used to separate instantaneous SHG signals from simultaneously emerging fluorescence [21]. A more interesting feature is the polarization fingerprint of each SHG source, which will be discussed fully in section 2.4. The polarization fingerprint was for instance used by Su *et al.* [22] to distinguish between SHG signals originating from collagen type I and II, and by Psilodimitrakopoulos *et al.* [23] to separate the signals of muscle tissue and tendon. Initially this technique was based on sequentially imaging a sample by at least 10 different orientations of the illumination polarization, and then performing a pixel-by-pixel data fitting. Recently, a single scan approach with direct calculation of the polarization fingerprint was described [24]. In this technique,

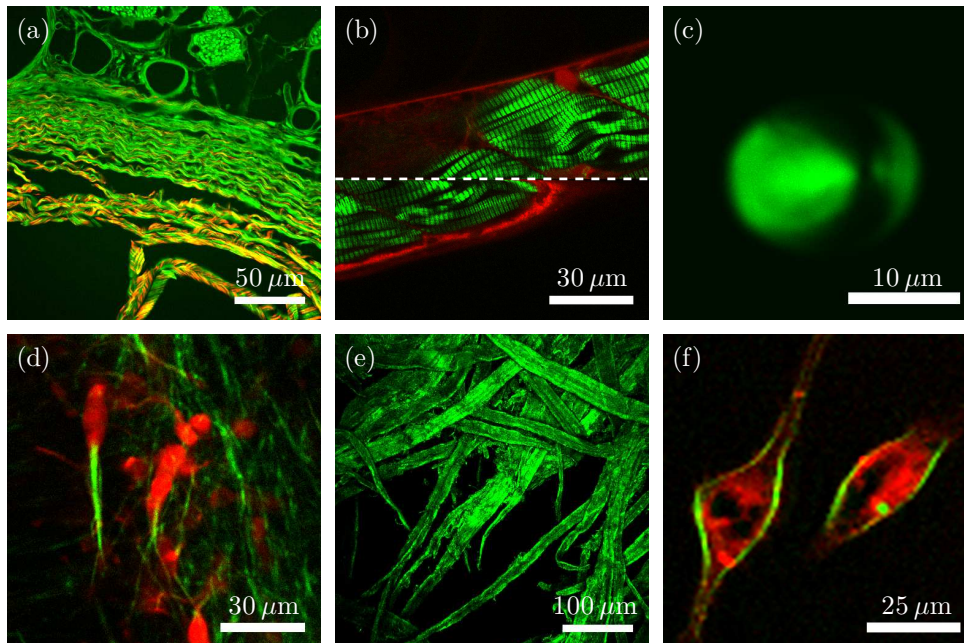


**Figure 1.3:** Overview of personally gathered, typical biological structures suited for SHG microscopy. The green channel represent SHG, the red channel TPEF of endogenous (a,b,e) or added (d,f) fluorophores. For all images, the polarization is along the scale bar. (a) Collagen in rat tail tendon. (b) Sarcomeres in the tail section of zebrafish (in collaboration with Marc Muller, ULg). The dashed line indicates a movement of the live fish during scanning. (c) Patoto starch granule. (d) Microtubules inside mouse cortical neurons (in collaboration with Ariel Avila Macaya, UHasselt). (e) Cellulose present in paper tissue. (f) Highly hyperpolarizable dye (Compound 14 in [25]) in cell membrane (in collaboration with Evelien de Meulenaere, KUL).

the sample is illuminated by a circularly polarized light, and by means of polarizing beam splitters, three different polarization states are acquired simultaneously.

### 1.2.3 Coherent scattering

Besides biological tissue-like structures, detectable SHG signals also originate from highly ordered polar molecules having a sufficiently large first order hyperpolarizability  $\beta$ , a measure for the strength of the first order non-linear response. Examples of these polar molecules are for instance a range of fluorescent proteins such as enhanced green or yellow fluorescent protein (eGFP, eYFP) [26–29]. Each free molecule individually emits a second order signal, and the resulting incoherent signal is referred to as hyper Rayleigh scattering (HRS) [30]. By locking the molecules in a parallel arrangement, constructive interference of these non-linear scatterers takes

place causing detectable SHG signals to arise. This alignment for instance occurs when functionalizing the proteins such that they arrange on the outer surface of the cellular membrane [31] (Fig. 1.3.f). Employing the hyperpolarizability properties of fluorescent proteins allows for simultaneous SHG and two-photon excited fluorescence imaging of the same structure. This effect has for instance been used to probe changes in membrane potential, or study protein internalization [32–35].

Instead of modeling collagen and myosin as non-centrosymmetric crystal-like structures, they can also be considered as a collection of anharmonic scatterers. Peptide bonds forming the backbone of the helical shape are also SHG active dipoles. This approach is used in section 2.4 to be able to estimate the pitch angle of these helical structures.

### 1.3 Thesis guide

Although bio-related SHG microscopy has been around for a while now, it is still not as often and commonly used as for instance fluorescence microscopy which can be considered as the golden standard. However, at first glance, both techniques rely on same basic feature: providing a huge optical contrast between the structure or region of interest and its surroundings. There is one major disadvantage of SHG microscopy compared to its fluorescence sister. The required non-centrosymmetry through tight packing of helical molecules makes SHG microscopy only applicable to just that handful of biological structures. On the other hand, the exploding developments of conjugated primary-secondary antibody assays allows for highly specific fluorescent staining of almost any type of molecule. In order to increase the applicability and output of SHG in biology, the emphasis is therefore often shifted towards obtaining detailed insight in the biological origin and physical properties of the generated signals. In this context, many biophysical models have recently appeared in literature [36–39], often involving molecular origins of the SHG signal. The models comprise spatial harmonophore distributions which are studied either by spatial imaging to obtain information on the supra-molecular level or by performing polarization SHG microscopy to assess properties on the molecular level. In this thesis a contribution is given to the biophysical developments by

- studying the applicability of existing models in the context of specific biological questions and typically used sample preparation techniques;
- designing data analysis techniques which are based on these existing models to obtain biologically relevant information in an unbiased and unambiguous way.

To understand why SHG signals arise under certain circumstances, it is crucial to have thorough knowledge on physical properties of the signal. In a general theory chapter (**Chapter 2**) the basic calculations on which model developments are based in general are given. This chapter contains a few additional theoretical considerations that are not further used in this thesis, but rather serve as a reference for future work. Additionally a chapter is devoted to the commercial microscope system used in this work (**Chapter 3**), and especially to the modifications that were done to increase its SHG performance.

The focus in **Chapter 4** lies on the field of tissue engineering. In this chapter we introduced a new method to unambiguously study the structural properties of SHG active collagen type I hydrogels. Typical SHG images of these structures contain a collection of randomly oriented fibrils, akin for a statistical approach to quantify this randomness. Triggered by the expertise of the biophysics research group on all kind of variations of fluorescence correlation spectroscopy, it was sought to which extent these techniques could be applied to the static SHG images of hydrogels. Since the existing correlation techniques are typically based on point sources, we had to

develop a new mathematical model of the autocorrelation function to include fibre like sources.

**Chapters 5, 6 and 7** deal with the highly ordered and - for biological tissue - extremely well defined skeletal muscle. This work was set off by a very interesting and elegant supra-molecular SHG model developed by Denis Rouède (Institut de Physique de Rennes) [36]. The model basically explains the structural origin of double band skeletal muscle striations, and relates these double band patterns to muscle proteolysis. We tried to use this model as such to study the effect of muscle disuse and experimental autoimmune encephalomyelitis (EAE) on the structural integrity of muscle tissue. The hypothesis was simple: the amount of double band patterns is related to the amount of muscle degradation. Yet, as there was no expertise on this topic in our biophysics research group, we first performed a thorough study on the applicability of the supra-molecular model. This yielded fundamental insights in using the supra-molecular model for analyzing SHG patterns of striated muscle, which are discussed in **Chapter 5**. The chapter contains a critical evaluation of Rouède's model, and serves as a guide on how to interpret the obtained information.

In **Chapter 6**, we introduce a new method to automatically analyze SHG images of muscle tissue for obtaining the same structural information as returned by the analysis using Rouède model. Basically, the algorithm is used to quantify the amount of double band patterns and is based on a Gabor wavelet transform of the complete SHG image [40]. The algorithm is explained in full detail for easy reproduction, and a biomedical relevant EAE case study is included to illustrate the applicability of the algorithm.

In **Chapter 7** it is shown that muscle degradation is not the only cause of double band patterns. The work was mainly initiated by an invariable return of double band SHG patterns when imaging healthy individual myofibrils and cardiac muscle tissue. As opposed to bulk skeletal muscle, individual myofibrils have limited dimensions ( $1 - 2 \mu\text{m}$ ) with respect to the focused illumination field size. By varying the sample thickness of bulk skeletal muscle tissue, we studied the effect of axial sample size on the SHG intensity profiles, and show that SHG active region dimensions influence the shape of the intensity profiles.

In the final **Chapter 8** a general conclusion and discussion is given, together with some considerations for follow up work.

As the work presented in this thesis is of interdisciplinary nature, chapters 4 to 7 were made possible through collaborations with biomedical colleagues, who were responsible for the sample dissection, collection, preparation, and slicing. My contribution focused on the biophysical model developments, model implementations and adaptations, microscopy, data analysis and data interpretation.



**CHAPTER 2**

---

**General theory**

---

## 2.1 Second harmonic generation

Multiple sources introducing the theoretical formalism for non-linear optical light-matter interactions are available [6, 41, 42]. The work *Second-order Nonlinear Optical Characterization Techniques: An Introduction* by Verbiest, Clays and Rodriguez [42] gives a good introduction on second harmonic generation used for thin film characterization, and is written in an understandable way for biologist and chemist. The book *Nonlinear optics* by Robert W. Boyd [6] treats SHG in a more physical and mathematical way. Unless a different reference is given, we adopted Boyd's method and notation to give the minimally needed equations and expressions for this thesis. Note that some numerical estimations are also shown in this chapter. For this, the selected parameter values are related to the experimental setup used in this work, in which we used an illumination wavelength of 810 nm.

### 2.1.1 Formalism

Optical second harmonic generation is a type of non-linear interactions between light and a non-centrosymmetric medium. In general, the electric field  $\vec{E}$  of an electromagnetic wave induces a polarization field  $\vec{P}$  inside a medium as [6]

$$\vec{P} = \epsilon_0 \chi \vec{E}, \quad (2.1)$$

with  $\chi$  the electric susceptibility of the medium,  $\epsilon_0$  the permittivity of free space and  $\vec{P}$  the induced polarization field inside the medium. For linear optical processes,  $\chi$  is either a scalar or a tensor of rank 2, while for non-linear optics,  $\chi$  becomes a higher rank tensor. In general, the induced polarization field is given by

$$\vec{P} = \epsilon_0 [\chi^{(1)} \cdot \vec{E} + \chi^{(2)} : \vec{E}\vec{E} + \chi^{(3)} \vdots \vec{E}\vec{E}\vec{E} + \dots] \quad (2.2)$$

where  $\chi^{(q)}$  represents the susceptibility of the  $q$ -th order process, and " $\cdot$ ", " $:$ " and " $\vdots$ " represent tensor products.  $q = 1$  refers to first order processes such as absorption, fluorescence or Rayleigh scattering. Second harmonic generation is a second order process for which the related polarization field,  $\vec{P}_{2\omega}$  is given by

$$\vec{P}_{2\omega} = \epsilon_0 \chi^{(2)} \vdots \vec{E}\vec{E}. \quad (2.3)$$

In this,  $\chi^{(2)}$  represents a  $3 \times 3 \times 3$  tensor of rank 3. Although this tensor contains 27 elements, most of them vanish under specific symmetry conditions. We will elaborate on this in section 2.4.

Classically, second harmonic generation can be considered to be a consequence of an anharmonic oscillator (Fig. 2.1 a). Formally this is treated by introducing a non-linear restoring force exerted on the electron in the Lorentz atom model. By representing a non-centrosymmetric medium as an asymmetric potential well  $U(x)$  in

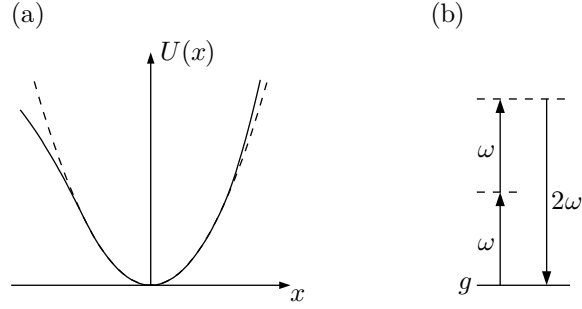


**Figure 2.1:** (a) Classical representation of SHG. The dashed line shows a symmetric potential well  $U(x)$ , while the solid line depicts an asymmetric potential well. (b) Quantum mechanical representation of SHG where the dashed lines represent virtual states and  $g$  indicates the ground state.

which atomic electrons oscillate, the resulting oscillating polarization field comprises higher modes, including the second order mode. A quantum mechanical representation is given in Fig. 2.1 b, where an incoming electric field with frequency  $\omega$  excites atoms from their ground state  $g$  to a first and second virtual or resonant state (dashed lines). Emission of a photon from the first virtual state represents linear scattering. Emission from the second virtual state resembles the second order non-linear scattering or second harmonic generation. A full quantum mechanical description to define the second order susceptibility is given in the book by Boyd [6].

### 2.1.2 Wave equation

The emitted electric field produced by the anharmonic oscillating polarization field is obtained by solving the wave equation derived from the Maxwell equations,

$$\nabla \times \nabla \times \vec{E}_{2\omega} - \frac{n^2}{c^2} \frac{\partial^2 \vec{E}_{2\omega}}{\partial t^2} = \frac{1}{\epsilon_0 c^2} \frac{\partial^2 \vec{P}_{2\omega}}{\partial t^2}, \quad (2.4)$$

with  $\vec{E}_{2\omega}$  the electric field component of the SHG signal,  $n$  the refractive index (RI), and  $c$  the speed of light in vacuum. Assuming that both the illumination wave and the SHG wave consist of a spatial and temporal part,

$$\vec{E}_{q\omega} = \vec{E}_{q\omega}(\vec{r}) \exp(-iq\omega t), \quad (2.5)$$

the wave equation can be recast to

$$\nabla^2 \vec{E}_{2\omega}(\vec{r}) + k_{2\omega}^2 \vec{E}_{2\omega}(\vec{r}) = -\frac{\pi\omega^2}{\epsilon_0 c^2} \vec{P}_{2\omega}(\vec{r}) \quad (2.6)$$

## CHAPTER 2

---

with  $k_{2\omega}$  the wave number related to the SHG wavelength. The Laplace operator ( $\nabla^2$ ) appears due to the vector identity  $\nabla \times \nabla \times \vec{E}_{2\omega}(\vec{r}) = \nabla(\nabla \cdot \vec{E}_{2\omega}(\vec{r})) - \nabla^2 \vec{E}_{2\omega}(\vec{r})$ , and under the assumption that no free charges are present and no currents exist ( $\nabla \cdot \vec{E}_{2\omega}(\vec{r}) = 0$ ) [6]. Eq. (2.6) is also referred to as the inhomogeneous Helmholtz equation or the wave equation. In section 2.3.4 we show a solution of this wave equation for a focused Gaussian illumination beam. In the next section, a solution for plane wave illumination is given in the context of forward versus backward SHG intensities.

## 2.2 Plane wave

### 2.2.1 Backward/Forward SHG

Due to the coherent nature of the SHG process, the thickness of a sample defines the amount of forward directed signal relative to the backward directed signal. This is depicted in Fig. 2.2a for a non-dispersive medium for which  $\Delta k = k_{2\omega} - 2k_\omega = 0$ , with  $k_\omega$  the wave number related to the illumination wavelength. In this figure, the illumination waves and SHG waves of three different scatterers (harmonophores), which can be regarded as oscillating dipoles emitting an SHG wave in all transverse directions, are shown. Independent of the position of a scatterer, the waves travelling in forward are always in phase with those of the other scatterers. In backward however, the waves are shifted in phase such that it is mirrored with respect to the forward travelling wave, resulting in destructive interference when scatterers are separated by  $(2q + 1)\lambda_\omega/8$  with  $q$  an integer and  $\lambda_\omega$  the illumination wavelength.

To derive an expression for the backward-to-forward intensity ratio, the SHG intensity within the sample is calculated by solving the wave equation (2.6). In this, it is assumed that the sample does not absorb or scatters SHG light. Using Green's theorem, the solution of the inhomogeneous Helmholtz equation (2.6) is obtained by the convolution product of Green's function and the right hand side of eq. (2.6). When assuming a plane illumination wave travelling in the  $z$ -direction, the one-dimensional Green function for our wave equation is given by

$$G(x) = \frac{e^{ik_{2\omega}|z|}}{2k_{2\omega}} \quad (2.7)$$

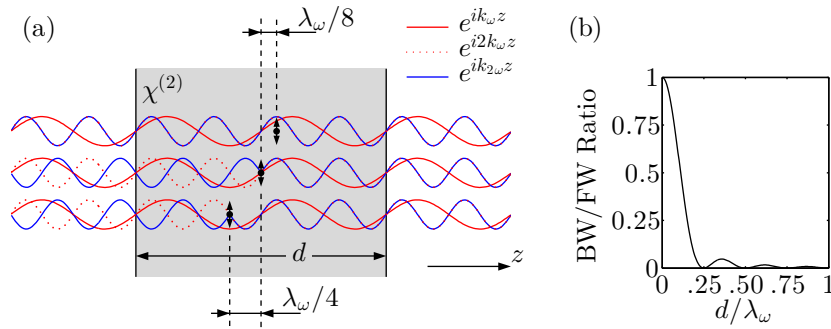


**Figure 2.2:** (a) Depiction of the coherence of the SHG signal in forward and backward. The illumination waves (red) and SHG waves (blue) are shown for three scatterers. (b) The backward (BW) to forward (FW) SHG intensity ratio as function of sample thickness  $d$ .

such that the second harmonic electric field is obtained by the convolution product

$$E_{2\omega}(z) = \frac{k_\omega E_0^2}{8\pi} \int \frac{e^{ik_{2\omega}|z-z_0|}}{2k_{2\omega}} \chi^{(2)}(z_0) e^{i2k_\omega z_0} dz_0. \quad (2.8)$$

As Green's function also represents the SHG wave emitted by a single scatterer, this method can alternatively be considered as a coherent summation of all scatterers within the non-centrosymmetric medium. When the non-centrosymmetric medium has infinite dimensions in the  $x$ - and  $y$ -direction, but is limited from  $z = 0$  to  $z = d$  in the  $z$ -direction, then the SHG field at a position  $0 \leq z \leq d$  is proportional to

$$E_{2\omega}(z) \propto e^{ik_{2\omega}z} \int_0^z e^{i\Delta k z_0} dz_0 + e^{-ik_{2\omega}z} \int_z^d e^{i\Sigma k z_0} dz_0 \quad (2.9)$$

$$\propto \frac{e^{ik_{2\omega}z}}{i\Delta k} \left( e^{i\Delta kd} - e^{i\Delta kz} \right) + \frac{e^{-ik_{2\omega}z}}{i\Sigma k} \left( e^{i\Sigma kz} - 1 \right) \quad (2.10)$$

with  $\Sigma k = k_{2\omega} + 2k_\omega$  and  $\Delta k = k_{2\omega} - 2k_\omega$ . One can interpret this equation as the coherent sum of all forward directed waves of the preceding scatterers ( $z_0 < z$ ) and all backward directed waves of the upcoming scatterers ( $z_0 > z$ ). Using this, the backward-to-forward SHG intensity ratio can be calculated,

$$\frac{I_{2\omega}^{\text{BW}}}{I_{2\omega}^{\text{FW}}} = \frac{|E_{2\omega}(0)|^2}{|E_{2\omega}(d)|^2} = \left[ \frac{\Delta k \sin(\Sigma kd/2)}{\Sigma k \sin(\Delta kd/2)} \right]^2. \quad (2.11)$$

For sake of completeness, the case of a dispersion-less medium ( $\Delta k = 0$ ) is shown. The backward-to-forward intensity ratio is then given by

$$\frac{I_{2\omega}^{\text{BW}}}{I_{2\omega}^{\text{FW}}} = \left[ \frac{\sin(2k_\omega d)}{2k_\omega d} \right]^2. \quad (2.12)$$

This backward to forward intensity ratio is plotted in Fig. 2.2b, showing that for  $d \ll \lambda_\omega$  the backward SHG intensity approaches the forward one. In this limit, the sample is infinitely thin with respect to the illumination wavelength, and can be considered as a single sheet of oscillating dipoles. In practice most biological specimen have a thickness well beyond the illumination wavelength, for which almost no backward signal can be detected relative to the forward one. Conversely, imaging is typically done using a focused laser beam, or focused Gaussian beam, which we will discuss in detail in the following section. Focused Gaussian beams typically have a limited *SHG active range* defined by the Rayleigh range  $z_R$  which related to the Gaussian beam waist size  $w_0$  and is given by

$$z_R = \frac{\pi w_0^2}{\lambda_\omega}. \quad (2.13)$$

This range is determined by the tightness of focusing through the objective, and is about  $0.4\ \mu\text{m}$  for a  $40\times 1.1$  objective and a wavelength of  $810\ \text{nm}$ . According to equation (2.12), this yields a forward signal about 100 times greater than the backward signal. Yet, when working with specimen of a few  $\mu\text{m}$  thick, the forward signal becomes scattered and absorbed, often leading to (slightly) higher backward-to-forward ratios.

### 2.2.2 Phase matching

Dispersion properties of an illuminated SHG active material may result in decreased SHG signals [6, 43]. In a slow varying plane wave approximation, the forward directed SHG intensity  $I_{2\omega}$  at position  $d$  (along  $\vec{k}_\omega$ ) within the SHG source is related to the material dispersion by [6]

$$I_{2\omega} \propto \left( \frac{\sin(\Delta kd/2)}{\Delta kd/2} \right). \quad (2.14)$$

Here  $\Delta k$  is the same one as given in the previous section. For a refractive index at the illumination wavelength of  $n_\omega = 1.39$ , a typical dispersion of  $\Delta n = n_{2\omega} - n_\omega = 0.02$  and an interaction length  $d = 0.4\ \mu\text{m}$  as estimated by the Rayleigh range, the SHG intensity drops by about 0.03% compared to the intensity for zero dispersion. Although this is only a small change, the RI mismatch will have detrimental effects on the spatial SHG intensity patterns, which we will show in chapter 5.

Intuitively the intensity loss due to phase mismatch can be considered to be a consequence of incoherence of successive scatterers. The phase mismatch causes successive scatterers to be slightly phase shifted with respect to each other. In this context, the coherence length  $l_c$  for the SHG process is defined by [6]

$$l_c = \frac{\pi}{\Delta k} \quad (2.15)$$

For the considered parameter values, the coherence length is about  $10\ \mu\text{m}$ , which is well beyond the Rayleigh range of a focused Gaussian beam, explaining the slight decreased intensity of 0.03%. For increasing sample thickness (or Rayleigh range), the effect of the phase mismatch becomes more pronounced, and for  $l_c = d$  the forward directed SHG signal completely vanishes according to equation (2.14).

## 2.3 Focused Gaussian beam

In a laser scanning microscope system, a plane laser wave passes through an objective resulting in a focusing of the plane wave. The three dimensional Gaussian approximation of the electric field of the focused beam is often used [6, 31, 36], and for a wave travelling in the  $z$ -direction this field is given by

$$E_\omega(x, y, z) = E_0 e^{-\frac{x^2+y^2}{w_0^2} - \frac{z^2}{w_z^2} + ik_\omega z - i\zeta(z)} \quad (2.16)$$

with  $E_0$  the amplitude of the electric field. The beam has radial and axial sizes determined by respectively  $w_0$ <sup>a</sup> and  $w_z$  which are further discussed in section 2.3.1, and  $\zeta(z)$  is the Gouy phase shift which is treated in section 2.3.2. In the following sections, we address properties of the Gaussian beam that are crucial in defining the SHG signal.

### 2.3.1 Point spread function

For many applications [36, 44–47], accurate information on the effective dimensions of the optical system point spread function (PSF) is crucial. A first and good approximation to the lateral dimensions of this PSF is still obtained by the optical resolution law introduced by Abbe, defined by the ratio of the excitation wavelength ( $\lambda$ ) and twice the numerical aperture (NA) of the illumination objective [48]. For confocal and multi-photon microscopy, the point spread function is often referred to as the confocal volume, excitation volume or illumination volume. This volume is generally approximated by a 3D Gaussian profile given by

$$I(x, y, z) = I_0 e^{-2q \frac{x^2+y^2}{w_0^2} - 2q \frac{z^2}{w_z^2}} \quad (2.17)$$

with  $q = 1$  for regular fluorescence and  $q = 2$  for two-photon effects such as TPEF and SHG. Defining the PSF in this way,  $w_0$  and  $w_z$  represent respectively the radial and axial half width at  $e^{-2}$  of the maximum  $I_0$ , and resembles the associated resolution of the imaging system. Using a Gaussian PSF is not only a good approximation for the effective PSF shape, but also greatly simplifies many calculations used, for instance, in quantitative fluorescence imaging [49].

The relation between the Gaussian PSF dimensions and the illumination wavelength, the system NA and the specimen refractive index ( $n$ ) have been empirically obtained [41, 50]. Yet, to take system variability such as beam misalignment, optical edge effects or scanning effects into account it is imperative to experimentally determine the PSF for each microscope. This is typically done by imaging a set of sub-diffraction beads or particles, preferably having diameters below 100 nm. For

---

<sup>a</sup> $w_0$  is often also denoted as  $w_{xy}$  (see Chapter 5)

fluorescence, several commercial point source kits are available. For obtaining the SHG PSF, commercially available nanoparticles such as zinc oxide is a good sample, although the SHG PSF should be the same as a TPEF PSF. Having a good estimate on the effective system resolution is also helpful in choosing an appropriate pixel size. In order to fulfill the Nyquist theorem and take most advantage of the imaging resolution,  $w_0$  should be covered by at least 2.4 pixels [51].

### 2.3.2 Gouy phase shift

Focusing through an objective imposes the Gouy phase shift which refers to a phase shift of the coherent light wave upon passing through the focal point. This phenomenon arises when spatially confining light waves into a Gaussian beam, and can be considered to be a consequence of momentum conservation [52]. The Gouy phase-shift of the electric field traveling in the  $z$ -direction is given by [6],

$$\zeta(z) = \arctan\left(\frac{z}{z_R}\right). \quad (2.18)$$

This means a tighter focusing of the light by means of an higher numerical aperture objective results in a faster phase reversal at the focal point.

For incoherent and isotropic processes such as fluorescence, the Gouy phase shift does not affect the properties of the emitted light. In case of second harmonic generation, all emitters inherit and preserve the phase of the illumination wave. Successive emitters are therefore not in phase along the illumination wave vector ( $\vec{k}_\omega$ ), but at a certain angle. To estimate this angle, consider two SHG emitters separated a distance  $d$  along  $\vec{k}_\omega$  (Fig. 2.3). Since  $E_{2\omega} \sim E_\omega^2$ , the phase difference between the emitters is given by  $2k_\omega d - 2\zeta(d)$ . Complete constructive interference of the SHG signal from both emitters then occurs under the angle  $\theta$  (Fig. 2.3) if

$$dk_{2\omega} \cos \theta = 2dk_\omega - 2\zeta(d). \quad (2.19)$$

Assuming zero refractive index mismatch between the illumination and emission wavelength ( $k_{2\omega} = 2k_\omega$ ), and using the first order approximation of the Gouy phase shift [6, 31], one obtains that

$$\cos \theta \approx 1 - \frac{1}{z_R k_\omega}. \quad (2.20)$$

It appears that the optimal emission angle does not depend on the distance between the emitters. When tight focusing by high NA objectives is present, higher orders of the Gouy phase shift approximation become more significant, resulting in a distance dependent optimal emission angle. This can for instance be used to detect changes in emitter density. We come back to this in chapter 8.

We estimated the optimal emission angle based on interference of SHG signal from only two emitters. The angle dependent far field emission intensity profile

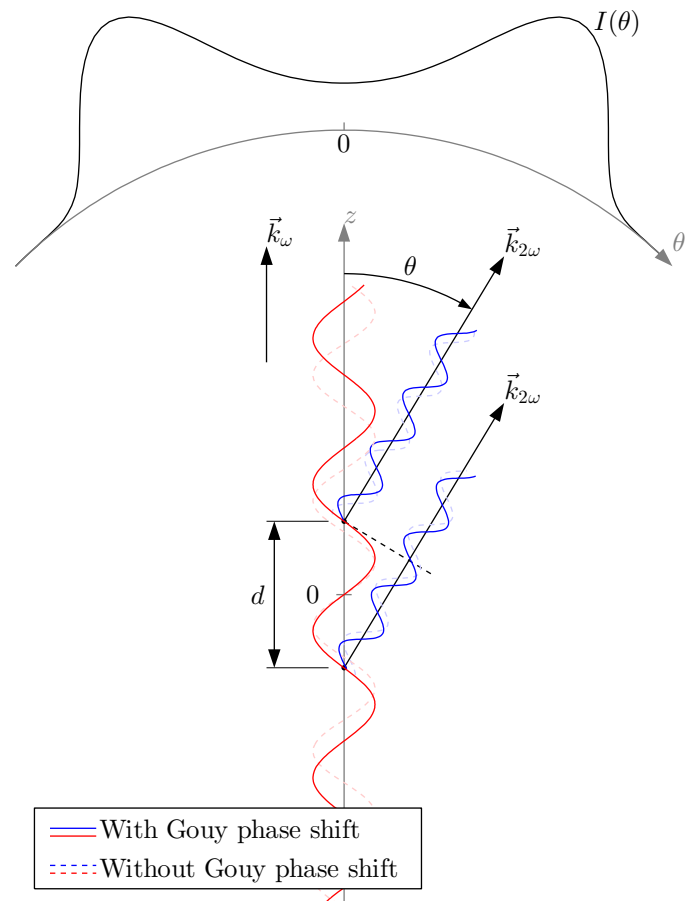


**Figure 2.3:** Depiction of the optimal angle for successive SHG emitters separated a distance  $d$ . The profile denoted by  $I(\theta)$  represent the angular dependence of the far field SHG intensity. The dashed lines indicate the case without Gouy phase shift to emphasize the impact of the Gouy phase shift.

$I(\theta)$  in Fig. 2.3 is calculated for a one dimensional, infinitely long SHG source positioned along the illumination wave-vector, at the radial center of the illumination beam. It shows that also for a homogeneous SHG source an optimal SHG emission angle arises due to the Gouy phase shift.

### 2.3.3 Numerical aperture considerations

As indicated previously, the numerical aperture of the illumination objective dictates the resolution of the imaging system. For epi-fluorescence imaging however, the NA also determines the collection cone for the isotropically radiated fluorescence [53], and partially prescribes the measured signal intensity. Although epi-detection is advantageous for fluorescence microscopy in terms of rejecting illumination light, also transmission schemes exist in which the resulting signals are collected by a condenser lens. Again, the NA prescribes the signal detection cone, and maximizing it will result in higher signals, up to a theoretical maximum of 50% of the total intensity.

Opposed to the isotropic nature of fluorescence emission, the coherent SHG process is known to result in directed signal emission. Whether the backward (epi) or forward (transmission) direction is favoured depends on the degree of phase matching, and is related to the dimension and dispersion properties of the imaged sample (see previous sections). Independent of the direction, the far field radiated SHG signal resulting from dispersionless media has a peak intensity at an angle that can be estimated from equation (2.20). This imposes a minimum collection angle is needed to detect the majority of the SHG signal. Using equation (2.20), the NA of the collection optics ( $\text{NA}^C$ ) for which the maximum SHG intensity is just collected can be estimated by

$$\text{NA}^C = n \sin \theta = \sqrt{\frac{2}{z_R k_\omega} - \left(\frac{1}{z_R k_\omega}\right)^2} \quad (2.21)$$

This implies that  $\text{NA}^C$  depends on the waist size of the focused illumination beam through  $z_R$  (see eq. (2.13)). This waist size is in turn related to the NA of the illumination objective ( $\text{NA}^I$ ). Although a good rule of thumb for selecting an appropriate collection condenser states that  $\text{NA}^C \geq \text{NA}^I$ , obtaining a good estimate of the PSF size ( $w_0$ ) can help to determine the feasibility of any illumination and collection NA combination. Since decreasing the beam waist size results in even higher emission angles, assume the limiting case of a beam waist of  $w_0 \approx 0.5\lambda/\text{NA}$  [31]. In the first order approximation,

$$\text{NA}^C \approx \frac{2\text{NA}^I}{\pi} \approx 0.64\text{NA}^I \quad (2.22)$$

estimates the aperture at which the far field emission profile reaches maximum intensity. Although in theory a part of the SHG signal is emitted beyond this aperture, two reasons can be given why equation (2.22) can be used to estimate  $\text{NA}^C$  such that the majority of the experimental SHG signal is collected. First, the actual beam

waist is typically larger than the proposed limiting case. This results in a lower angle for the peak intensity of the emission profile. Second, for high  $\text{NA}^I$  values,  $\text{NA}^C$  is overestimated by to first order approximation used in equation (2.22).

### 2.3.4 Gaussian beam SHG

To obtain the electric field of an oscillating dipole at position  $\vec{r}_0$ , the wave equation (2.6) has to be solved for  $\vec{E}_{2\omega}$  for each position in space  $\vec{r}$ . In the work by Rouède *et al.* [36], a solution is proposed in the form

$$\vec{E}_{2\omega}(\vec{r}) = -\frac{\pi\omega^2}{\epsilon_0 c^2} \int \frac{e^{ik_{2\omega}|\vec{r}-\vec{r}_0|}}{4\pi|\vec{r}-\vec{r}_0|} (I - \hat{s}\hat{s}) \cdot \vec{P}_{2\omega}(\vec{r}_0) d\vec{r}_0 \quad (2.23)$$

where  $\hat{s}\hat{s}$  is the dyadic product of the unit vector  $\hat{s}$  along  $\vec{k}_{2\omega}$ , and  $I$  is a second order unit tensor<sup>b</sup>. This solution can be viewed at in two ways. The argument of the integral is the far field approximation of electric field caused by a single radiating dipole, which is known to be a solution of the inhomogeneous wave equation. The integration represent a coherent summation over all dipoles in space. For the alternative interpretation, the fractional part inside the argument is know as Green's function for the Helmholtz equation. Green's theorem states that the solution of the inhomogeneous Helmholtz equation (2.6) is given by the convolution of the Green function and the non-zero right hand side of equation (2.6). In either way, due to the far field approximation ( $|\vec{r}| \gg |\vec{r}_0|$ ),

$$|\vec{r} - \vec{r}_0| = |\vec{r}| - \frac{\vec{r} \cdot \vec{r}_0}{|\vec{r}|} = |\vec{r}| - \frac{\vec{k}_{2\omega} \cdot \vec{r}_0}{k_{2\omega}} \quad (2.24)$$

equation (2.23) can be further approximated as

$$\vec{E}_{2\omega}(\vec{r}) = -\frac{\omega^2}{4\epsilon_0 c^2} \frac{e^{ik_{2\omega}|\vec{r}|}}{|\vec{r}|} \int e^{-i\vec{k}_{2\omega} \cdot \vec{r}_0} (I - \hat{s}\hat{s}) \cdot \vec{P}_{2\omega}(\vec{r}_0) d\vec{r}_0 \quad (2.25)$$

We assume that the illumination electric field  $E_\omega(\vec{r}_0)$  is polarized such that the second harmonic polarization  $\vec{P}_{2\omega}$  field only has a non-zero component in the  $x$ -direction (Fig. 2.4),

$$\vec{P}_{2\omega} = \epsilon_0 \chi^{(2)} g(\vec{r}_0) \vec{E}_\omega^2(\vec{r}_0) \hat{x}. \quad (2.26)$$

The function  $g(\vec{r}_0)$  introduces a spatial modulation function for the second order susceptibility  $\chi^{(2)}$ , which can be used to model any structure of interest. Then the SHG intensity is given by

$$I_{2\omega}(r, \theta, \phi) = \frac{n_{2\omega} c \epsilon_0}{2} \left( \frac{\chi^{(2)} k_\omega^2}{4r} \right)^2 (1 - \sin^2 \theta \cos^2 \phi) \left| \int e^{-i\vec{k}_{2\omega} \cdot \vec{r}_0} g(\vec{r}_0) \vec{E}_\omega^2(\vec{r}_0) d\vec{r}_0 \right|^2 \quad (2.27)$$

---

<sup>b</sup> $(I - \hat{s}\hat{s}) \cdot \vec{P}_{2\omega} = (\hat{s} \times \vec{P}_{2\omega}) \times \hat{s}$

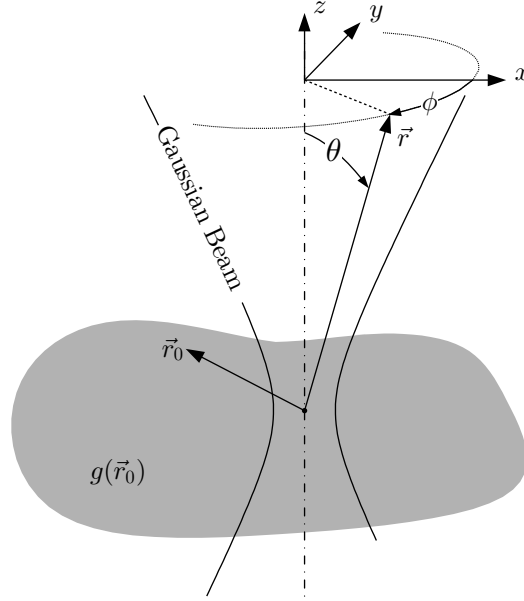


**Figure 2.4:** Coordinate system for solving the wave equation when using a Gaussian illumination profile.

If  $g(\vec{r}_0)$  can be decoupled into the three Cartesian coordinates  $g_x(x)g_y(y)g_z(z)$ , the integral can be split into three components,

$$E_{2\omega}^X = \int g_x(x) e^{-ik_{2\omega}x \sin \theta \cos \phi - \frac{2x^2}{w_0^2}} dx \quad (2.28)$$

$$E_{2\omega}^Y = \int g_y(y) e^{-ik_{2\omega}y \sin \theta \sin \phi - \frac{2y^2}{w_0^2}} dy \quad (2.29)$$

$$E_{2\omega}^Z = \int g_z(z) e^{-ik_{2\omega}z \cos \theta - \frac{2z^2}{w_z^2} + 2ik_{\omega}z - 2i\zeta(z)} dz \quad (2.30)$$

such that

$$I_{2\omega}(r, \theta, \phi) = \frac{n_{2\omega}c\epsilon_0}{2} \left( \frac{\chi^{(2)}k_{\omega}^2 E_0^2}{4r} \right)^2 (1 - \sin^2 \theta \cos^2 \phi) I^X I^Y I^Z \quad (2.31)$$

with  $I^X \equiv |E_{2\omega}^X|^2$ ,  $I^Y \equiv |E_{2\omega}^Y|^2$  and  $I^Z \equiv |E_{2\omega}^Z|^2$ . This set of equations is not only a solution of the wave equation under Gaussian beam illumination, but also allows to introduce spatial variations of the second order susceptibility. This is used in chapter 5. The total radiated SHG power  $\mathcal{P}_{2\omega}$  is obtained by integrating  $I(r, \theta, \phi)$  in the solid angle  $\Omega$ ,

$$\mathcal{P}_{2\omega} = \int_{\Omega} I(r, \theta, \phi) r^2 \sin \theta d\theta d\phi. \quad (2.32)$$

As discussed in the previous section,  $\Omega$  is defined by the signal collection aperture defined by the numerical aperture of either the illumination objective or the condenser. Finally, in imaging systems, the power  $\mathcal{P}_{2\omega}$  is converted into a pixel intensity value by the detector.

### 2.3.5 SHG as a rare process

Typical values for second order susceptibility are in the order of  $10^{-12}$  m/V in crystal structures [6], making the second harmonic generation an extremely inefficient process. For biological structures such as collagen, the  $\chi^{(2)}$  is typically one or two orders of magnitude smaller [54]. To more appreciate the presence of SHG in biological tissue, it is illustrative to estimate the conversion efficiency by evaluating equation (2.32), based on the set-up used in this thesis (see Chapter 5). For a 40x oil immersion objective with a numerical aperture of 1.3, the Gaussian beam dimension are  $w_0 = 0.467 \mu\text{m}$  and  $w_z = 1.946 \mu\text{m}$ . For *e.g.* a biological sample, the refractive indexes  $n_\omega = 1.39$  and  $n_{2\omega} = 1.41$  (see Chapter 5) are used. The illumination wavelength is 810 nm. Making use of

$$E_0 = \sqrt{\frac{2I_{\omega,0}}{n_\omega \epsilon_0 c}} = \sqrt{\frac{2\mathcal{P}_\omega}{\pi w_0^2 n_\omega \epsilon_0 c}} \quad (2.33)$$

with  $\mathcal{P}_\omega$  the illumination power, the SHG power by equation (2.32) equals

$$\mathcal{P}_{2\omega} = \frac{n_{2\omega} k_\omega^4}{8\pi^2 n_\omega^2 \epsilon_0 c w_0^4} [\chi^{(2)}]^2 \mathcal{V} \mathcal{P}_\omega^2 \quad (2.34)$$

with  $\mathcal{V}$  the spatial integration part of which the value is primarily defined by the focal volume of the Gaussian illumination beam,

$$\mathcal{V} = \int_{\Omega} (1 - \sin^2 \theta \cos^2 \phi) I^X I^Y I^Z \sin \theta d\theta d\phi. \quad (2.35)$$

For the given parameter values,  $\mathcal{V} \approx 10^{-38} \text{m}^6$  when taking all emission directions into account. This results in a final output power (in Watts) given by

$$\mathcal{P}_{2\omega} \approx 10^{16} [\chi^{(2)} \mathcal{P}_\omega]^2. \quad (2.36)$$

Assuming a continuous wave illumination with a typical average illumination power of about 0.01 W and  $\chi^{(2)} = 10^{-13}$  m/V, the SHG power is only about  $10^{-14}$  W, or the conversion efficiency is only about  $\eta \approx 10^{-10}$ . This output power is below the detection limit of  $10^{-12}$  W for an analogue photo-multiplier tube (PMT) in the 1 MHz range dictated by the typical scan speed of the used microscope [55]<sup>c</sup>. Using

<sup>c</sup>The analogue PMTs used in this work were delivered by Zeiss, for which no specifications are available. We therefore based our calculations on parameters of a Hamamatsu detector.

a pulsed laser with repetition rate  $f = 80$  MHz and pulse duration  $\tau = 100$  fs, the relation between the average power  $\mathcal{P}^{\text{ave}}$  and peak power  $\mathcal{P}^{\text{peak}}$  is given by

$$\mathcal{P}^{\text{ave}} \approx f\tau\mathcal{P}^{\text{peak}}, \quad (2.37)$$

such that the conversion efficiency for the pulsed system is given by

$$\eta = \frac{\mathcal{P}_{2\omega}^{\text{ave}}}{\mathcal{P}_{\omega}^{\text{ave}}} \approx 10^{16} [\chi^{(2)}]^2 \mathcal{P}_{\omega}^{\text{peak}}. \quad (2.38)$$

The conversion thus linearly depends on the peak power of the ultra short pulses, allowing for increasing the efficiency without increasing the average power and the chance of photo-damage. In the work by Koester *et al.* [56], photo-damage for varying average power and pulse length was explored more in detail. Nevertheless, using the 0.01 W average illumination power, the output power is approximately  $10^{-9}$  W for  $\chi^{(2)} = 10^{-13}$  m/V. In order to achieve a certain signal-to-noise ratio (SNR) by a PMT, the signal power should be  $\text{SNR}^2$  times that of the detection limit [55]. Then, assuming 100% detection efficiency, the output power obtained by the ultra short pulses results in  $\text{SNR} \approx 30$ . This example elucidates why pulsed lasers are crucial to perform SHG microscopy on biological tissue.

## 2.4 Polarization SHG

Here we present a derivation of the polarization response of the SHG signal when illuminating with purely linearly polarized light. This implies that we assume that imaging is done through low to moderate NA ( $< 0.7$ ) objectives, as tight focusing through high NA objectives is known to induce additional polarization components [57, 58]. We have moreover assumed that optical effects such as birefringence, polarization cross-talk or diattenuation are negligible, which is known to be not the case for e.g. tendon tissue [59], or muscle tissue (see chapter 5).

### 2.4.1 Polarization dependent intensity pattern

In the classical treatment, SHG is assumed to originate from oscillating polarization fields inside a material with a non-zero second order susceptibility (see previous sections). Instead of dipoles, the material is often considered as a non-centrosymmetric crystal belonging to a specific point group [6, 42]. A point group of chiral symmetry ( $C_\infty$  in the Schoenflies notation) is such a non-centrosymmetric group, and is often used to approximate the symmetry properties of helical polymers such as collagen or myosin [38, 60–63]. Neumann’s principle states that the tensor must remain invariant under any operation belonging to a symmetry group [42]. This often reduces the number of non-zero susceptibility tensor elements to only a few. Both 2-fold and 4-fold rotational operations are subgroups of the cylindrical symmetry of the chiral type, such that the cylindrical symmetry group with axis along the  $x$ -direction (Fig. 2.5) has to abide the following rules,

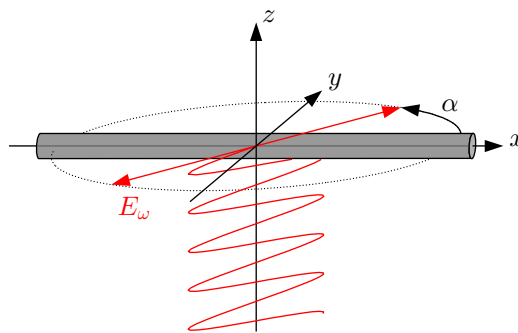


**Figure 2.5:** Coordinate system used for deriving the intensity variation of the SHG signal for varying polarization.  $E_\omega$  is the electric field component of the illumination light, and  $\alpha$  is the angle between  $E_\omega$  and the symmetry axis of the cylinder depicted in grey.

$$\begin{array}{ll}
 \text{2-fold: } & x \rightarrow x \\
 & y \rightarrow -y \\
 & z \rightarrow -z \\
 \text{4-fold: } & x \rightarrow x \\
 & y \rightarrow z \\
 & z \rightarrow -y.
 \end{array}$$

Note that we use the coordinate system in Fig. 2.5 in accordance with that in Fig. 2.4. For 2-fold symmetry, the mentioned rules lead to the following restrictions for all 27 tensor elements,

$$\begin{array}{llll}
 \chi_{xxx}^{(2)} = \chi_{xxx}^{(2)} & \chi_{yxx}^{(2)} = -\chi_{yxx}^{(2)} = 0 & \chi_{zxx}^{(2)} = -\chi_{zxx}^{(2)} = 0 \\
 \chi_{xxy}^{(2)} = -\chi_{xxy}^{(2)} = 0 & \chi_{yyx}^{(2)} = \chi_{yyx}^{(2)} & \chi_{zxy}^{(2)} = \chi_{zxy}^{(2)} \\
 \chi_{xxz}^{(2)} = -\chi_{xxz}^{(2)} = 0 & \chi_{yxz}^{(2)} = \chi_{yxz}^{(2)} & \chi_{zxz}^{(2)} = \chi_{zxz}^{(2)} \\
 \chi_{xyx}^{(2)} = -\chi_{xyx}^{(2)} = 0 & \chi_{yyx}^{(2)} = \chi_{yyx}^{(2)} & \chi_{zyx}^{(2)} = \chi_{zyx}^{(2)} \\
 \chi_{xyy}^{(2)} = \chi_{xyy}^{(2)} & \chi_{yyy}^{(2)} = -\chi_{yyy}^{(2)} = 0 & \chi_{zyy}^{(2)} = -\chi_{zyy}^{(2)} = 0 \\
 \chi_{xyz}^{(2)} = \chi_{xyz}^{(2)} & \chi_{yyz}^{(2)} = -\chi_{yyz}^{(2)} = 0 & \chi_{zyz}^{(2)} = -\chi_{zyz}^{(2)} = 0 \\
 \chi_{xzx}^{(2)} = -\chi_{xzx}^{(2)} = 0 & \chi_{yzx}^{(2)} = \chi_{yzx}^{(2)} & \chi_{zzx}^{(2)} = \chi_{zzx}^{(2)} \\
 \chi_{xzy}^{(2)} = \chi_{xzy}^{(2)} & \chi_{yzy}^{(2)} = -\chi_{yzy}^{(2)} = 0 & \chi_{zzy}^{(2)} = -\chi_{zzy}^{(2)} = 0 \\
 \chi_{xzz}^{(2)} = \chi_{xzz}^{(2)} & \chi_{yzz}^{(2)} = -\chi_{yzz}^{(2)} = 0 & \chi_{zzz}^{(2)} = -\chi_{zzz}^{(2)} = 0.
 \end{array}$$

It is assumed that the order in which the tensor works on the applied electric field does not affect the results ( $\chi_{ijk}^{(2)} = \chi_{ikj}^{(2)}$ ). Using this technique, one can easily show that for materials with a center of symmetry ( $x \rightarrow -x, y \rightarrow -y, z \rightarrow -z$ ), all second order tensor elements cancel each other out such that no SHG can exist. Two fold rotation symmetry already cancels out 14 elements. The remaining non-zero elements also have to fulfil the conditions related to 4-fold symmetry,

$$\begin{array}{llll}
 \chi_{xxx}^{(2)} = \chi_{xxx}^{(2)} & \chi_{yxy}^{(2)} = \chi_{zxx}^{(2)} & \chi_{zxy}^{(2)} = -\chi_{yxx}^{(2)} \\
 \chi_{xyy}^{(2)} = \chi_{xzz}^{(2)} & \chi_{yxz}^{(2)} = -\chi_{zxy}^{(2)} & \chi_{zxx}^{(2)} = \chi_{yxy}^{(2)} \\
 \chi_{xyz}^{(2)} = -\chi_{xzy}^{(2)} = 0 & \chi_{yyx}^{(2)} = \chi_{zxx}^{(2)} & \chi_{zyx}^{(2)} = -\chi_{yxx}^{(2)} \\
 \chi_{xzy}^{(2)} = -\chi_{xyz}^{(2)} = 0 & \chi_{yzz}^{(2)} = -\chi_{zyx}^{(2)} & \chi_{zxx}^{(2)} = \chi_{yxy}^{(2)} \\
 \chi_{xzz}^{(2)} = \chi_{xyy}^{(2)}
 \end{array} \quad (2.39)$$

This again cancels out 2 elements, and careful inspection of the indices reveals that the number of independent elements reduced to only 4. For convenience, the remaining tensor elements are denoted in the contracted notation  $d_{ij}$  with  $i = 1, 2, 3$  for  $x, y, z$ , and  $j = 1, 2, 3, 4, 5, 6$  for  $xx, yy, zz, yz = zy, xz = zx, xy = yx$  respectively. By convention,  $\chi_{ijk}^{(2)} = 2d_{ijk}$ . This finally results in an induced polarization field  $\vec{P}_{2\omega}$  given by

$$\vec{P}_{2\omega}(\vec{r}_0) = 2\epsilon_0 \begin{pmatrix} d_{11} & d_{12} & d_{12} & 0 & 0 & 0 \\ 0 & 0 & 0 & 0 & d_{25} & d_{26} \\ 0 & 0 & 0 & 0 & d_{26} & -d_{25} \end{pmatrix} \begin{pmatrix} E_{\omega}^x(\vec{r}_0)E_{\omega}^x(\vec{r}_0) \\ E_{\omega}^y(\vec{r}_0)E_{\omega}^y(\vec{r}_0) \\ E_{\omega}^z(\vec{r}_0)E_{\omega}^z(\vec{r}_0) \\ 2E_{\omega}^y(\vec{r}_0)E_{\omega}^z(\vec{r}_0) \\ 2E_{\omega}^x(\vec{r}_0)E_{\omega}^z(\vec{r}_0) \\ 2E_{\omega}^x(\vec{r}_0)E_{\omega}^y(\vec{r}_0) \end{pmatrix}. \quad (2.40)$$

Assuming the illumination field lies in the  $x - y$ -plane,  $E_\omega^x(\vec{r}_0) = E_0(\vec{r}_0) \cos \alpha$ ,  $E_\omega^y(\vec{r}_0) = E_0(\vec{r}_0) \sin \alpha$  and  $E_\omega^z(\vec{r}_0) = 0$ ,  $\vec{P}_{2\omega}(\vec{r}_0)$  reduces further to

$$\vec{P}_{2\omega}(\vec{r}_0) = 2\epsilon_0 E_\omega^2(\vec{r}_0) \begin{pmatrix} d_{11} \cos^2 \alpha + d_{12} \sin^2 \alpha \\ 2d_{26} \sin \alpha \cos \alpha \\ -2d_{25} \sin \alpha \cos \alpha \end{pmatrix}. \quad (2.41)$$

To obtain the final SHG electric field, this polarization field is plugged into equation (2.25),

$$\vec{E}_{2\omega}(\vec{r}) = -\frac{\omega^2}{2c^2} \frac{e^{ik_{2\omega}|\vec{r}|}}{|\vec{r}|} (I - \hat{s}\hat{s}) \cdot \begin{pmatrix} d_{11} \cos^2 \alpha + d_{12} \sin^2 \alpha \\ d_{26} \sin 2\alpha \\ -2d_{25} \sin 2\alpha \end{pmatrix} \int e^{-i\vec{k}_{2\omega} \cdot \vec{r}_0} E_\omega^2(\vec{r}_0) d\vec{r}_0 \quad (2.42)$$

Mostly it is assumed that the SHG is only emitted along  $\hat{z}$ , such that  $\hat{s} = \hat{z}$  and the resulting SHG intensity  $I_{2\omega}(\vec{r})$  is given by

$$I_{2\omega}(\alpha) = [d_{26}^2 \sin^2 2\alpha + (d_{11} \cos^2 \alpha + d_{12} \sin^2 \alpha)^2] \int_0^\Theta C(\theta) \sin \theta d\theta \quad (2.43)$$

with  $\Theta = \text{asin}(\text{NA}/n_\omega)$  and

$$C(\theta) = 2\pi \left( \frac{k_\omega}{2} \right)^2 \left| \int e^{-ik_{2\omega}z_0} E_\omega^2(\vec{r}_0) d\vec{r}_0 \right|^2. \quad (2.44)$$

Equation (2.43) shows that for a given material with tensor elements  $d_{11}$ ,  $d_{12}$  and  $d_{26}$ , the SHG intensity varies only when changing the angle between the polarization of the illumination light and the symmetry axis of the crystal. By performing an experiment in which the illumination field is rotated, the resulting intensity profile can be used to estimate  $d_{11}/d_{26}$  and  $d_{12}/d_{26}$ . The result of equation (2.43) is used in chapter 4, though a different system is used such that  $d_{11} \rightarrow d_{33}$ ,  $d_{12} \rightarrow d_{32}$  and  $d_{26} \rightarrow d_{15}$ .

Although eq. (2.43) is often used in literature, the assumption that the SHG signal is only emitted along the  $k$ -vector of the illumination beam does not agree with the emitted oscillation dipole field. For the sake of completeness, and to provide a reference for future work, we continue with the full derivation of the SHG signal. The SHG intensity without the assumption of uni-axial SHG emission is given by

$$I_{2\omega}(\alpha, \Theta) = d_{25}^2 \sin^2 2\alpha \int_0^\Theta D(\theta) \sin \theta d\theta + [d_{26}^2 \sin^2 2\alpha + (d_{11} \cos^2 \alpha + d_{12} \sin^2 \alpha)^2] \int_0^\Theta C(\theta) \sin \theta d\theta \quad (2.45)$$

with

$$C(\theta) = \pi(1 + \cos^2 \theta) \left( \frac{k_\omega^2}{2} \right)^2 \left| \int e^{-i\vec{k}_{2\omega} \cdot \vec{r}_0} E_\omega^2(\vec{r}_0) d\vec{r}_0 \right|^2 \quad (2.46)$$

$$D(\theta) = -2\pi \sin^2 \theta \left( \frac{k_\omega^2}{2} \right)^2 \left| \int e^{-i\vec{k}_{2\omega} \cdot \vec{r}_0} E_\omega^2(\vec{r}_0) d\vec{r}_0 \right|^2. \quad (2.47)$$

In the limit for  $\Theta \rightarrow 0$ , uni-axial emission along the illumination direction is mimicked. For a collection angle defined by a condenser with NA = 0.8, and for an imaging system with  $w_{xy} = 0.48 \mu\text{m}$ ,  $w_z = 1.95 \mu\text{m}$ ,  $\lambda = 810 \text{ nm}$ ,  $n_\omega = 1.39$ ,  $n_{2\omega} = 1.42$ , the  $D(\theta)$  integral is only about 10 times smaller than the  $C(\theta)$  integral and can thus not be ignored. An alternative assumption to obtain the same angular intensity dependence as in eq. (2.43) is Kleinman symmetry. This symmetry condition holds when the medium is lossless for both the illumination and emissions wavelength, such that full permutation of indices should not affect the susceptibility tensor. Based on the identities in (2.39), Kleinman symmetry dictates that  $d_{25} = 0$ , ruling out the first term of eq. (2.45). Additionally,  $d_{12} = d_{26}$  reduces the number of independent tensor elements to only 2. Whether or not Kleinman symmetry is a valid assumption is still under debate [64]. Using the eqn. (2.45)-(2.47) the effect of  $d_{25}$  on the angular intensity profile can be studied in the context of Kleinman symmetry by varying the numerical aperture of the signal collection optics.

### 2.4.2 Helical pitch angle

In biological tissue, the SHG signal is often originating from coiled-coil  $\alpha$ -helical filaments. It was suggested and verified by simulations that the  $\alpha$ -helix possesses a non-zero hyper-polarizability with the main component oriented along the  $C_\alpha$ -N-C bond of the backbone [8, 9]. Instead of considering the filament axis as the cylindrical symmetry axis, the helix is therefore considered as a collection of harmonophores with second order polarizability  $\beta$  for which only the tangential  $\beta_{x'x'x'}$  is non-zero (Fig. 2.6). It is assumed that the harmonophores are oriented along the path of the helix, indicated by  $x'$  in Fig. 2.6. The density of covalent bonds ( $N$ ) simultaneously contributing to the SHG signal is sufficiently high to consider a continuous spatial average of all orientations. This is done by first transforming  $\beta_{x'x'x'}$  from the harmonophore system  $(x', y', z')$  to the helix system  $(x, y, z)$  using the transformation matrix

$$T = \begin{pmatrix} \cos \theta & -\sin \theta & 0 \\ \sin \theta \sin \phi & \cos \theta \sin \phi & -\cos \phi \\ \sin \theta \cos \phi & \cos \theta \cos \phi & \sin \phi \end{pmatrix}. \quad (2.48)$$

The second order susceptibility for the entire helix is then obtained by

$$\chi_{ijk}^{(2)} = \frac{N}{2\pi} \int_0^{2\pi} T_{ix'} T_{jx'} T_{kx'} \beta_{x'x'x'} d\phi \quad (2.49)$$

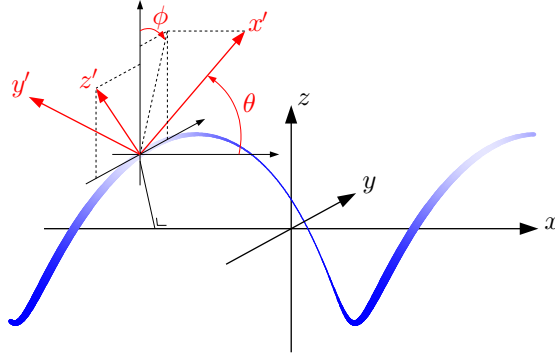


**Figure 2.6:** Helical pitch angle obtained from harmonophores oriented along the path of the helix.  $x'$  is tangential to the helix,  $\theta$  is the helical pitch angle which is constant along the helix, and  $\phi$  is the angle between the  $z$ -axis and the projection of  $x'$  on the  $y$ - $z$ -plane.

for all elements  $ijk$ . There is no need to average for helical pitch angle  $\theta$  since it does not vary in space. The susceptibility tensor results in

$$\chi^{(2)} = \frac{N\beta_{x'x'x'} \cos \theta}{2} \begin{pmatrix} 2 \cos^2 \theta & \sin^2 \theta & \sin^2 \theta & 0 & 0 & 0 \\ 0 & 0 & 0 & 0 & 0 & \sin^2 \theta \\ 0 & 0 & 0 & 0 & \sin^2 \theta & 0 \end{pmatrix}. \quad (2.50)$$

This resembles the susceptibility tensor for cylindrical symmetry, under the assumption of Kleinman symmetry (eq. (2.40)). Additionally, the values of  $d_{11}$  and  $d_{12}$  contain information on the helical pitch angle of the molecule of interest. From the experimentally obtained values for these two non-zero tensor elements, obtained by fitting experimental polarization dependent intensity profiles with eq. (2.43), the helical pitch angle can be estimated by

$$\cos^2 \theta = \frac{d_{11}/d_{12}}{2 + d_{11}/d_{12}} \quad (2.51)$$

## **CHAPTER 3**

---

### **Instrumentation**

---

### 3.1 Microscope system

All microscopy in the work presented in this thesis is done on a Zeiss confocal microscope. The scan head is the LSM510 META module, and is mounted on a motorized Axiovert 200M. For multi-photon purposes, the microscope is extended with a tunable femto-second pulsed MaiTai laser (Spectra Physics), combined with a DeepSee pre-dispersion controller. Although the commercial system allows for many possible light paths, multi-photon microscopy typically relies on the basic path shown in Fig. 3.1. We will discuss some important features of this path from the excitation to the detection side, bearing in mind that the system is only used for SHG microscope.

The illumination is done by the tunable pulsed laser. For SHG imaging, typical illumination wavelengths reported in literature range from 750 nm to 950 nm [65], which is a range in which the MaiTai performs optimally. For our experiments, the laser is always tuned at 810 nm. This is mainly based on the performance parameters of the device: at 800 nm, the output power is maximum and the shortest pulses are delivered which should result in the brightest SHG signals (see Sec. 2.3.5). The reason we select 810 nm instead of 800 nm is based on the choice of the 400–410 nm SHG band pass filter.

After passing the scanning mirrors, the pulsed laser passes through a long pass dichroic mirror with an edge at 680 nm (NDD-Di). This dichroic is used to later on reflect the signal to the backward non-descanned detection (NDD) system. The NDD method is possible because of the intrinsic confocal behaviour of multi-photon processes as a consequence of the required high illumination intensities. The pulsed laser is assumed to be a plane wave focussed to a specimen using an imaging objective. Typically, a high resolution objective is used that is optimized for wavelengths ranging from ultra-violet to the near infra red region, being crucial for SHG microscopy. In this work, a 20x/0.75 air objective (Plan-Apochromat 20x/0.75, Carl Zeiss), a 40x/1.1 water immersion objective (LD C-Apochromat 40x/1.1 W Korr UV-VIS-IR, Carl Zeiss), and a 40x/1.3 oil immersion objective (Plan-Neofluar 40x/1.3 Oil DIC, Carl Zeiss) are used.

For the epi, or backward detection, the signal is collected by the illumination objective. By the NDD dichroic (NDD-Di) mirror, the signal is projected to the NDD system. The NDD system contains two analogue photo-multipliers (Zeiss) allowing for simultaneously two-channel detection. By a secondary long pass dichroic (LP-Di) mirror with an edge at 442 nm, the SHG signal is reflected to one of the detectors where it has to pass a narrow band-pass 400 – 410 nm filter (BP-SHG) before reaching the detector. Any high wavelength signal, such as two-photon (auto)fluorescence can be simultaneously detected by the second detector. In front of this detector, a wide band pass 450 – 650 nm (BP-TPEF) is installed to make sure no SHG and no illumination light is detected.

The same NDD set can be used for forward detection, for instance by repositioning the NDD set. To make sure sufficient signal reaches the forward positioned NDD

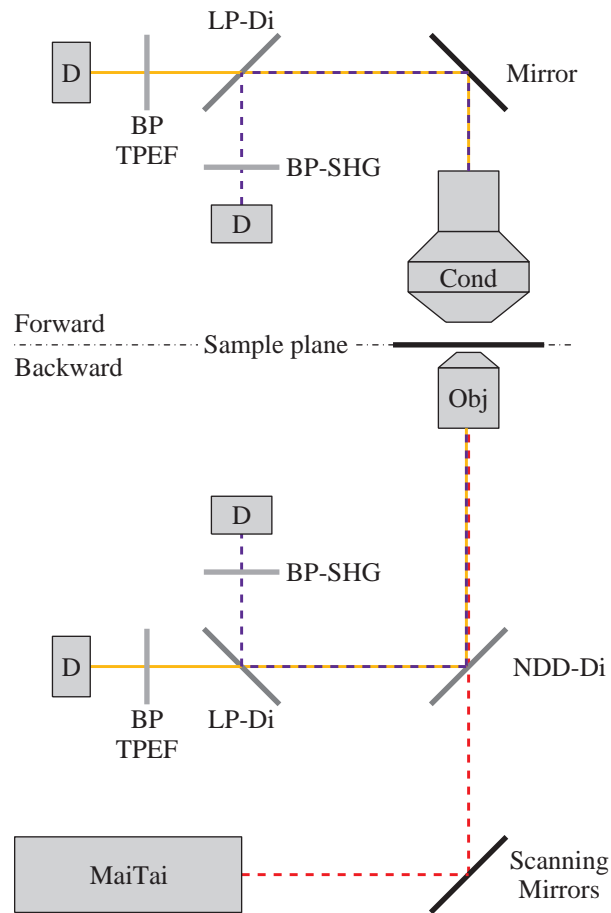


**Figure 3.1:** Light path of the microscope setup used in this thesis. The dashed lines represent the illumination process and the scattered SHG signal. The solid lines represent fluorescent signals. NDD-Di is the non-descanned dichroic mirror, LP-Di is a long pass dichroic mirror, BP-SHG is a narrow band pass filter used to filter the SHG signal and BP-TPEF is the band pass filter used for the two-photon fluorescence signal. Obj is the illumination objective and Cond is the condenser. D stands for detector.

## CHAPTER 3

---

set, a decent condenser is required. Decent refers to the optimal NA of the condenser, defined by the SHG process (see Sec. 2.3). A rule of thumb in SHG imaging states that the signal collection NA should be at least that of the objective [66], although in section 2.3.3 we showed a more stringent rule.

## 3.2 Condenser properties

The used microscope is designed for a condenser with an NA= 0.55, but was equipped with a condenser having an adaptable NA up to 0.8 (provided by Zeiss). This high NA condenser consists of two parts: a light collecting part with a built in diaphragm to control the effective NA, and an additional optical part to connect the condenser to the microscope body (Fig. 3.2 a). The additional optical part is a beam reducer which should convert the  $\sim 45$  mm output diameter of the collecting part to a diameter of 24 mm dictated by the clear aperture of typical optical components such as band pass filters. However, the output diameter of the beam reducing part is 32 mm (Fig. 3.2.a). Assuming that the signal uniformly exits the beam reducer over the full diameter of the output lens, this leads to a 44% loss of collected signal relative to the clear aperture of filters.

We tested the collected intensity as function of increasing NA. A stationary beam was used to non-linearly excite a fluorescent dye in a solution, serving as an isotropic emitting light source. Assuming the condenser with a certain NA collects photons over the surface of spherical cap defined by the angle  $\theta = \text{asin}(\text{NA}/n)$ , with  $n$  the refractive index of the condenser immersion medium, the detected intensity  $I$  is given by

$$I(\text{NA}) \propto 1 - \sqrt{1 - (\text{NA}/n)^2}. \quad (3.1)$$

For the air-condenser,  $n = 1$ . The intensity as function of NA for the condenser provided by Zeiss is shown by the open circles in Fig. 3.3. The solid line indicates the expected trend according to equation 3.1, using the intensity at NA= 0 as offset value and using a proportionality factor obtained by fitting the intensity as function of the NA up to NA= 0.3. The experimental trend deviates from the expected trend at an NA between 0.3 and 0.4, and slightly increases to an intensity related to an NA of  $\sim 0.4$  as indicated by the dashed line. Assuming the collecting part of the condenser performs optimally, the lower than expected NA is caused by insufficient beam reduction (Fig. 3.2.a). We therefore designed a new beam reduction part, consisting of two lenses (Fig. 3.2.b): a 2" lens with a 100 mm focal distance, separated 60 mm from a 1" lens with a  $-40$  mm focal distance. This reduces the beam diameter by a factor of 2.5, resulting in an output diameter of 18 mm. For this home made beam reducer, the intensity as function of NA follows the expected theoretical behavior up to an NA of about 0.5. For increasing NA, the intensity increases slightly more to a value related to an NA of about 0.63 as indicated by the dotted line. Compared to the commercial beam reducer, the collected signal intensity increases by a factor of 2, which is closely related to the previously mentioned 44% signal loss. Note a slightly higher dark noise level is present when using the home made beam reducing part. This could be explained by the missing coverage of the beam reducer, allowing more stray light and environmental light to leak into the beam path and reach the detector.

Besides the effective collection angle of the condenser, a proper condenser align-

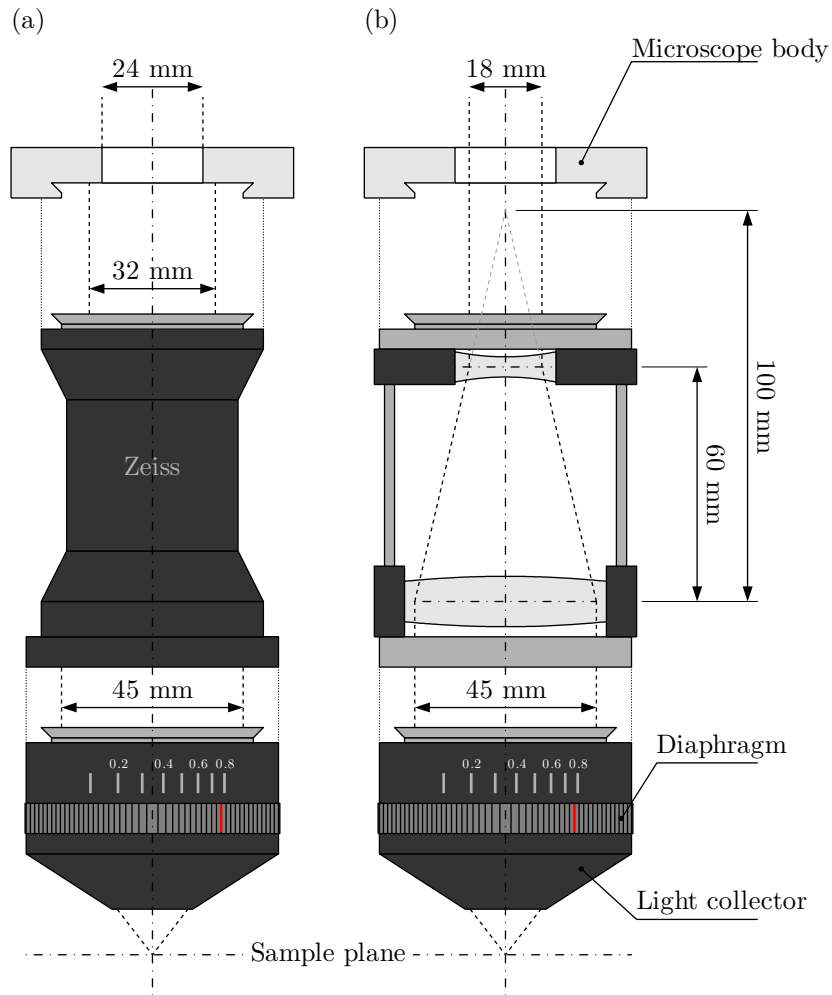


**Figure 3.2:** Comparison of condenser system as provided by Zeiss (a), and our adjusted condenser system (b).

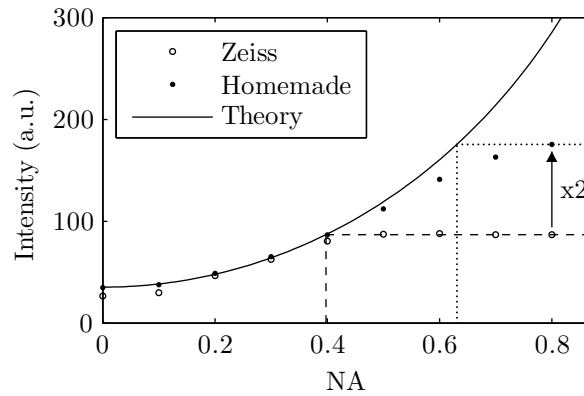


**Figure 3.3:** Collected intensity of a isotropic light source for varying NA of an air condenser ( $n = 1$ ). The dark noise causes an offset at  $NA = 0$  which is included in the theoretical profile.

ment is crucial to collect the majority of the SHG signal. A good starting point for this alignment is Köhler illumination, obtained by focusing the field diaphragm of the microscope to the sample plane through illumination with a halogen lamp. However, this field diaphragm is located just above the microscope body (Fig. 3.2), while the detector is reached only after passing additional mirrors and lenses beyond the field diaphragm. Therefore, the SHG signal is not optimally transferred to the detector for Köhler illumination. For the setup used in this work, we found that the SHG signal increases by setting a critical condenser alignment. This critical alignment is achieved by focusing a halogen lamp, which is positioned at the detector site, to the sample plane. Basically, this procedure ensures that the full signal is focused to the photo-sensitive part of the photo-multiplier.

### 3.3 Polarization controller

To perform polarization SHG experiments (Sec. 2.4), we designed an automated polarization controller device. Although this device was not explicitly used in this thesis, a technical description is given for future reference. We first show the theory basics related to the device to calculate the output polarization state, and then discuss some key technical aspects to understand the functioning of the device.

#### 3.3.1 Output polarization

The device allows a full control of the polarization state of the illumination beam before it reaches the sample. It is known that the output polarization of the MaiTai is linear and parallel to the table. After passing the scanning mirrors, the polarization is parallel to the front of the microscope, or parallel to the lower edge of an image. We assumed that the polarization remains linear after passing the optical system of the LSM510 scan head, although the extinction ratio was never tested.

The microscopy body has a slot to insert a slider between the non-descanned dichroic mirror and the scan head output (Fig. 3.1). We designed a slider containing a quarter wave plate (qwp) to control the ellipticity, and a half wave plate (hwp) to rotate the main polarization axis of the illumination beam. The beam first passes the qwp and then the hwp, allowing for an easy configuration of the polarization state (Fig. 3.4). The output polarization can be calculated for every orientation  $\varphi$  of the qwp and  $\vartheta$  of the hwp by means of the Jones matrices. The Jones matrices for the qwp ( $Q$ ) and hwp ( $H$ ) with their fast axis along the  $x$ -direction are given by,

$$Q = \begin{pmatrix} 1 & 0 \\ 0 & i \end{pmatrix} \quad H = \begin{pmatrix} 1 & 0 \\ 0 & -1 \end{pmatrix} \quad (3.2)$$

By using the rotation matrix,

$$R(\theta) = \begin{pmatrix} \cos \theta & \sin \theta \\ \sin \theta & -\cos \theta \end{pmatrix} \quad (3.3)$$

the Jones matrices for a qwp with angle  $\varphi$  and hwp with angle  $\vartheta$  with respect to the  $x$ -axis are given by

$$Q(\varphi) = R(\varphi)QR^{-1}(\varphi) = \begin{pmatrix} \cos^2 \varphi - i \sin^2 \varphi & \frac{1+i}{2} \sin 2\varphi \\ \frac{1+i}{2} \sin 2\varphi & \sin^2 \varphi - i \cos^2 \varphi \end{pmatrix} \quad (3.4)$$

$$H(\vartheta) = R(\vartheta)HR^{-1}(\vartheta) = \begin{pmatrix} \cos 2\vartheta & \sin 2\vartheta \\ \sin 2\vartheta & -\cos 2\vartheta \end{pmatrix}. \quad (3.5)$$

The input polarization is oriented along the  $x$ -direction,

$$\vec{E}_\omega = E_0 \begin{pmatrix} 1 \\ 0 \end{pmatrix}. \quad (3.6)$$

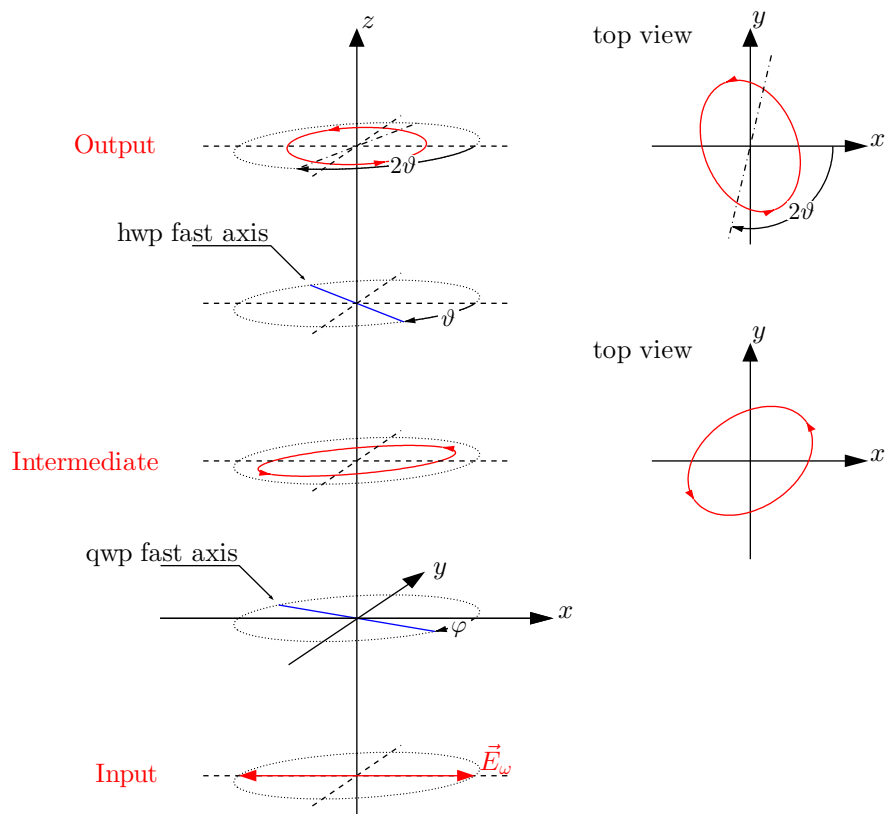


**Figure 3.4:** Schematic representation of the polarization controller device. Half wave plate is denoted by hwp, and quarter wave plate by qwp.

**Table 3.1:** Overview of value for  $\varphi$  and  $\vartheta$  for a few standard output beams for horizontally linear polarized input beam ( $x$ -dir).

	$\varphi$	$\vartheta$
Horizontal linear polarization ( $x$ -dir.)	0	0
Vertical linear polarization ( $y$ -dir.)	0	$\pi/4$
Diagonal (bottom left to top right) linear polarization ( $+\pi/4$ )	0	$\pi/8$
Diagonal (top left to bottom right) linear polarization ( $-\pi/4$ )	0	$-\pi/8$
Right circular polarization (RCP)	$\pi/4$	any
Left circular polarization (LCP)	$-\pi/4$	any

such that the output field  $\vec{E}_\omega^{\text{out}}$  is given by

$$\vec{E}_\omega^{\text{out}} = H(\vartheta)Q(\varphi)\vec{E}_\omega. \quad (3.7)$$

In Fig. 3.4 the intermediary and output field are represented in a Lissajous figure for an arbitrary  $\varphi$  and  $\vartheta$ . In Table 3.1 a few combinations for the qwp and hwp rotation are shown to produce basic and often used polarization states.

Up to here, it is assumed that the NDD dichroic mirror and the objective do not affect the polarization of the transmitted light. In reality however, we know that the NDD dichroic mirror possesses phase retardation resembling that of a quarter wave plate. This affects the polarization state, except the purely horizontally or vertically polarized light. For forward NDD detection schemes, the NDD dichroic mirror can be left out of the beam path. However, for backward detection, the NDD is crucial and should be taken into account. Assuming that the dichroic mirror behaves as a quarter wave plate, horizontally and vertically polarized light are not affected, and circularly polarized light can be obtained by setting the polarization  $\pm\pi/4$  with respect to the  $x$ -axis (Table 3.1). Linearly polarized light at  $\pi/4$  is obtained by setting circularly polarized light with the device. Chou *et al.* [67] calculated that a combination of a hwp and qwp can be used to pre-compensate for any retardation or  $x$  vs.  $y$  transmission ratio introduced by a given optical system. Our polarization controller can therefore be used to rule out the effect of the NDD dichroic mirror.

### 3.3.2 Technical notes

Both the quarter and half wave plate can be rotated using computer controller stepper motors (Trinamic PD-110-42, Hamburg, Germany). The motors cover a  $360^\circ$  rotation in 1600 steps, and a 1:2 gear ratio is used to transmit the rotation from motor to wave-plate by a tooth belt. This results in a total of 3200 steps per rotation, and thus an angular resolution of  $0.1125^\circ$ . Because of the physical dimensions of the motors, they

are positioned on the external part of the slider that is inserted into the microscope body.

The controlling software contains a module to perform experiments that are synced with the TTL frame pulse of a time-series measurement from the Zeiss microscope. This can be used to for instance perform automated polarization-SHG experiments (see Sec. 2.4). The sync scheme is depicted in Fig. 3.5. Syncing is done through opto-coupled one-way communication by reading the Zeiss frame pulse using the motor controller unit. To initialize the experiment, first a proper time series needs to be set in the Zeiss software. This includes defining the scanning parameters to obtain the frame time, and a delay of about 2-3 seconds is required between each frame. The frame time needs to be transferred manually to the polarization controller, in which also a wave-plate rotation sequence has to be defined.

The synced experiment is started in the controller software first. The wave-plates rotate (Rotation) to their starting positions. Then the controller waits for the first frame pulse of the Zeiss software. This first frame pulse is delivered when the time-series experiment is started in the Zeiss software, meaning that the controller waits for the user to start the experiment. Once the controller detects the pulse, a waiting timer starts for the duration of the previously given frame time. A delay of a few microseconds exists between the start of the time-series, and the start of the timer in the controller software. This is due to the Set-Reset latch (SR-latch) which makes the micro-second frame pulse of the Zeiss detectable for the discrete readout of the controller (Readout loop). The controller therefore always waits long enough before setting the new polarization (Rotation), which thus always happens during the delay of the Zeiss time-series. After rotation, the controller waits for the next frame pulse. The timing sequence is repeated for the number of steps defined by the polarization sequence. In general, this method partly relies on a correct timer clock of both machines, but through the use of the physical sync, the Zeiss and the controller software will always be synced.

### 3.3.3 Validation experiment

To validate the functioning of the polarization controller device, an experiment was performed to estimate the helical pitch angle of amylopectin in a potato starch granule [23]. For this, a sequence of SHG images is made with a rotating linear illumination polarization (Fig. 3.6 a). The linear polarization starts at the reference value defined by the polarization state of the laser, which is parallel to the lower edge of the image. The polarization angle  $\alpha$  starts at  $0^\circ$  (parallel to lower edge of the image) and increases by  $18^\circ$  until it has rotated up to  $702^\circ$ . This yields a pixel-by-pixel polarization fingerprint of 40 polarization states. This fingerprint is analysed by equation (2.45) under the assumption of Kleinmann symmetry, and including a phase shift to

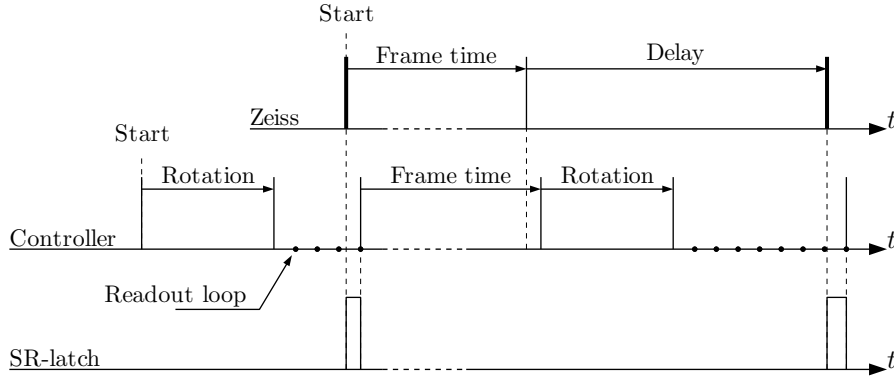


**Figure 3.5:** Timing scheme for synced experiments.

estimate the orientation of the SHG active molecule in the imaging plane ( $\phi$ ),

$$I(\alpha) = A \left\{ \sin^2 2(\alpha - \phi) + [B \cos^2(\alpha - \phi) + \sin^2(\alpha - \phi)]^2 \right\}. \quad (3.8)$$

This yields two physically relevant parameters: the orientation of the molecule with respect to the lower edge of the image ( $\phi$ ), and the ratio of two tensor parameters ( $B = d_{11}/d_{12}$ ). From the latter, the helical pitch angle is estimated by equation (2.51). The analysis was done using the Fast-Fourier P-SHG algorithm [68], and mapping of both the SHG source orientation and helical pitch angle is shown in Fig. 3.6 b-c. The orientation mapping shows the radial direction of SHG sources which is typical for starch granules. As can be observed from the histogram of the helical pitch angle (Fig. 3.6 d), a peak value at  $33^\circ$  is observed with a full width at half maximum (FWHM) of about  $10^\circ$ . Within the error range, our results are similar to those obtained by Psilodimitrakopoulos *et al.* [23]: a histogram peak at  $36^\circ$  with a FWHM of about  $9^\circ$ . This results indicating that the polarization controlling device is functioning properly.

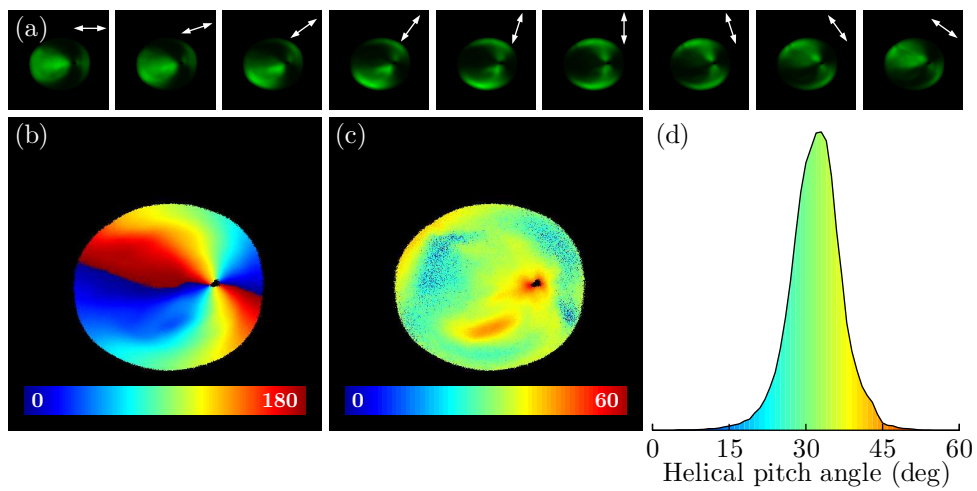


**Figure 3.6:** (a) Selection of polarization dependent SHG images of a potato starch granule. (b) Mapping of the orientation of SHG active molecule within the granule.  $0^\circ$  is parallel to the horizontal edge of the image. (c) Mapping of the helical pitch angle. (d) Histogram of the helical pitch angle. The color coding is the same as in panel (c). The histogram peak is located at  $33^\circ$ .

### 3.4 Noise definition

In chapter 5 and 6, SHG intensity profiles are fitted by theoretical profiles. To estimate the goodness-of-fit for each profile, the noise definition of the used analogue photo-multipliers (PMTs) is determined. Mainly two processes define the noise of the PMT: dark noise as a results of photocathode thermionic emission, and shot noise resulting from the signal. Besides these physical processes, the integration time per pixel, or pixel time, affects the noise properties through signal averaging. It is therefore preferred to experimentally determine the noise properties for a given integration time, but also for the experiment environmental parameters such as background light or reflections by optics.

In this work we assumed Gaussian noise of which the standard deviation  $\sigma_n$  varies as function of the average intensity  $\mu_n$  as a consequence of shot noise. Experimental values for these parameters are obtained by scanning a uniform image or a sufficiently long single spot time series for varying mean intensity, ranging from under-illumination to over-illumination. The noise data can be acquired from a solution of a fluorescent dye, looking at the SHG signal from a spot, or by collecting illumination light scattered from an interface. Note that it is always assumed that the illumination is stable and uniform within the entire image when measuring the noise properties.

In Fig. 3.7 the noise definition of our system is given for two different pixel dwell times using 8-bit analogue to digital conversion. Using this noise definition, the goodness-of-fit can be quantified using the reduced  $\chi^2$  statistic<sup>a</sup> calculated by

$$\chi^2 = \frac{1}{N - \nu - 1} \sum_{i=1}^N \frac{(I_i^t - I_i^e)^2}{\sigma_n(I_i^t)^2} \quad (3.9)$$

with  $N$  the number of data points in the experimentally obtained intensity profile  $I^e$  and  $\nu$  the number of freely adjustable fit parameters defining the theoretical intensity profile  $I^t$ .

---

<sup>a</sup>Not the be confused with the second order susceptibility tensor  $\chi^{(2)}$ .

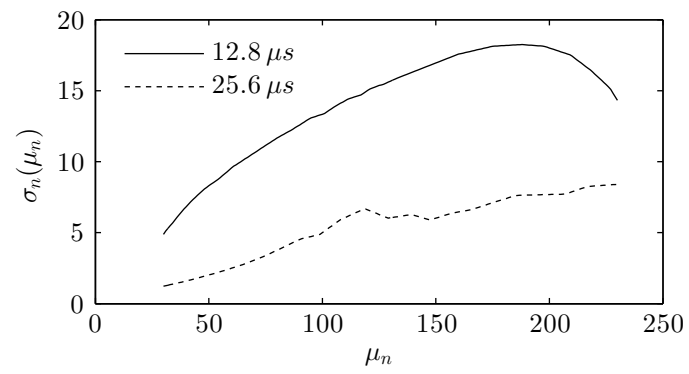


**Figure 3.7:** Noise definition of the imaging system for 2 different pixel dwell times in an 8-bit image. A Gain of 750 and a 20x/0.75 objective were used.



## **CHAPTER 4**

---

# **Polarization second harmonic generation by image correlation spectroscopy on collagen type I hydrogels**

---

**Paesen, R.**, Sanen, K., Smisdom, N., Michiels, L. & Ameloot, M. Polarization second harmonic generation by image correlation spectroscopy on collagen type I hydrogels. *Acta Biomater.* **10**, 2036–2042 (2014)

## 4.1 Abstract

Successful engineering of bio-mimetic tissue relies on an accurate quantification of the mechanical properties of the selected scaffold. To improve this quantification, typical bulk rheological measurements are often complemented with microscopic techniques, including label-free second harmonic generation (SHG) imaging. Image correlation spectroscopy (ICS) has been applied to obtain quantitative information from SHG images of fibrous scaffolds. However, the typical polarization SHG (P-SHG) effect, which partly defines the shape of the autocorrelation function (ACF), has never been taken into account. Here we propose a new and flexible model to reliably apply ICS to P-SHG images of fibrous structures. By starting from a limited number of straightforward assumptions and by taking into account the P-SHG effect, we are able to cope with the typically observed ACF particularities. Using simulated datasets, the resulting model is thoroughly evaluated and compared with models previously described in literature. We show that our new model has no restrictions concerning the fibre length for the density retrieval. For certain length ranges, the model can additionally be used to obtain the average fibre length and the P-SHG related non-zero susceptibility tensor element ratios. From experimental data on collagen type I hydrogels, values of SHG tensor element ratios and fibre thickness are determined which match values reported in the literature, thereby underpinning the validity and applicability of our new model.

## 4.2 Introduction

Tissue engineering focuses on creating an optimal environment to grow individual cells into functional tissue. This preferred environment depends on the cell type, meaning that the required biomechanical properties have to be tailor-made: e.g. neuronal cells prefer soft flexible environments while stiff and rigid structures are required for cartilage growth in joints or cardiac tissue [69–71]. Although an accurate knowledge of these mechanical properties is important, bulk rheological measurements are used throughout, while equally important, local micro-structural properties are generally ignored or difficult to assess.

Collagen type I hydrogels are known to be good scaffolds and often used for the growth of collagen related tissue such as cartilage or dermis [72, 73]. For assessing the hydrogel properties, more researchers are currently finding their way to various types of microscopy such as confocal fluorescence or reflectance microscopy, and label-free second harmonic generation (SHG) microscopy which is particularly useful in the case of collagen scaffolds [46, 74]. Although the mentioned microscopy techniques provide detailed images of the hydrogel structure, the required image analysis for obtaining quantitative structural information is often done by subjective thresholding and manual data extraction [46, 75, 76]. In avoiding these subjective and often tedious techniques, image correlation spectroscopy (ICS) [49] is believed to be a proper alternative and a robust approach for quantifying the image content of fibre networks. In general, ICS is based on mapping the average pixel correlation, resulting in an autocorrelation function (ACF) which contains statistical information of the underlying image.

Various publications have already appeared in which the typical width of the ACF has been used to identify the properties of a hydrogel. Raub *et al.* [46] suggested that this width is representative for the fibre thickness, which in turn is a crucial measure for the mechanical properties of the hydrogel. In addition to this fibre thickness, the pore size is a key parameter that influences mechanical properties. Pore size information could be obtained by direct image analysis, yet others have shown that this size is proportional to the product of the average fibre length and the average number of fibres per unit area (density) [77, 78]. For images of fibrous structures, Robertson *et al.* [47] showed that the amplitude of the ACF is determined by exactly that product. So, in order to correctly assess the pore size of the hydrogel, the ACF amplitude needs to be precisely estimated. Unfortunately, image noise jeopardizes direct amplitude readout. Additionally, Robertson *et al.* [47] mentioned that for instance a Gaussian approach results in an underestimate of the amplitude, implying substantial model dependence for ACF amplitude recovery. Therefore, a good theoretical model is needed to fit the entire ACF, with the exception of the noise containing centre value. Besides improved amplitude recovery, an appropriate ACF model might reveal additional information of the imaged structures. In the specific case of SHG microscopy on collagen type I hydrogels, the typical polarization SHG (P-SHG) effect leads to

a material specific, orientation dependent intensity modulation determined by only a few SHG tensor elements [9, 23]. By employing the appropriate ACF model, it should be possible to extract information on those tensor elements from the very specific ACF data.

Different models have been proposed to analyze the ACF of fibre like images. The most evident ACF model is a 2D Gaussian function [46, 78]. This has shown to work perfectly for images of point sources [49], but appropriate measures have to be taken for fibre like structures. Robertson *et al.* [47] suggested an approach in which the ACF is treated as the probability distribution for pixel correlation due to the fibre like structures. In this, the real fibre is modelled to be one pixel wide and  $L$  pixels long, for which it is possible to explicitly derive the probability distribution in the limiting case of sufficiently long fibres. By convolving the resulting distribution with the autocorrelated optical system point spread function (PSF) the ACF of an image of *pixel* fibres, convolved with the PSF, is obtained. Although this is a valid approach, the choice of considering fibres of one pixel wide is a limiting factor for the model, making Robertson's model only applicable when a pixel size comparable to the real fibre thickness is chosen. This thickness, however, is often not known a priori as it is a parameter of interest. Finally, because of this *pixelized* method, possible angular intensity modulations, such as the P-SHG effect, cannot be incorporated directly into the model.

In the current contribution a method is introduced to simulate an image of randomly positioned fibres, inspired by P-SHG images of collagen type I hydrogels. We assume that fibres have a finite length. In addition the fibres are considered to have a thickness which is at most  $\sim 25\%$  of the resolution of the imaging system so that the apparent PSF increase remains negligible ( $\leq 1\%$ ). We use this as a basis to test the models used by Raub *et al.* [46] and Robertson *et al.* [47] for analyzing the ACF of images of complete randomness in both position and orientation of the individual fibres. Additionally we propose an alternative model for analyzing the specific ACF of the P-SHG images. In this model the P-SHG effect is incorporated such that information on the tensor elements can be successfully retrieved from the ACF. Finally, we test the different approaches on a dilution series of a collagen type I hydrogel to elucidate the correctness of the ACF amplitude estimate and the applicability of the proposed model.

## 4.3 Calculations and Modelling

### 4.3.1 Simulation framework

A collagen type I hydrogel is considered to comprise only individual collagen fibres with mean length  $\langle L \rangle$  and with a diameter of 80 nm. Experimentally, these parameters can be tuned by changing conditions such as pH, ionic strength and polymerisation temperature [46]. An imaged fibre  $F(x, y)$  lying in the image plane, positioned at  $(0, 0)$  and oriented along the x-axis can then be considered as a convolution ( $*$ ) of an infinitely thin fibre of length  $L$  and the point spread function  $G(x, y)$  of the imaging system

$$F(x, y) = G(x, y) * \delta(|X| < L/2, y). \quad (4.1)$$

By means of a coordinate transformation, including translation and rotation, of the  $\delta$ -function in eq. 4.1, the fibre can be positioned anywhere inside the image and oriented freely within the image plane. Typically for ICS [49], the PSF is assumed to be Gaussian,

$$G(x, y) = I_0 \exp \left[ -2 \left( \frac{x^2}{w_x^2} + \frac{y^2}{w_y^2} \right) \right], \quad (4.2)$$

with  $w_{x,y}$  the half width at the  $e^{-2}$  value, often referred to as the PSF width. This width is typically in the range of 300 – 400 nm, allowing for the assumption that 80 nm thick fibres can be considered as infinitely thin.

In this work, additional emphasis is put on the intensity dependence due to the angle of the polarization of the incident light relative to the fibre long axis, known as polarization SHG (P-SHG) [23, 38]. In general, for fibres lying in the imaging plane, this P-SHG intensity modulation  $p(\theta)$  is defined as

$$p(\theta) = \sin^2 2\theta + \left( \frac{d_{31}}{d_{15}} \sin^2 \theta + \frac{d_{33}}{d_{15}} \cos^2 \theta \right) \quad (4.3)$$

where  $\theta$  is the angle between the collagen fibre and the polarization, and  $d_{ij}$  are the non-zero second order macroscopic susceptibility tensor elements. In the particular case of Kleinman symmetry, it holds that  $d_{31} = d_{15}$  while the value of the ratio  $d_{33}/d_{15}$  ranges from 1.3 to 1.5 for collagen type I [9].

### 4.3.2 Autocorrelation function

The autocorrelation function  $g(\eta, \xi)$  of an image is defined as

$$g(\eta, \xi) = \frac{\langle \delta I(x - \eta, y - \xi) \delta I(x, y) \rangle}{\langle I(x, y) \rangle^2} \quad (4.4)$$

where  $I(x, y)$  represent the image,  $\langle \dots \rangle$  is the average over all  $x$  and  $y$  values of the argument, and  $\delta I(x, y) = I(x, y) - \langle I(x, y) \rangle$ . In the case of an image of sub-resolution beads, the ACF of the image is simply a Gaussian with a width increased

by a factor  $\sqrt{2}$  compared to that of the PSF. However, in case of a fibre, additional correlation is induced over the length of this fibre. Because of the commutative and associative properties of the convolution product of symmetric functions, the ACF of one fibre  $g^1(\eta, \xi)$ , having length  $L$  and oriented along the  $x$ -axis can be written as

$$g^1(\eta, \xi) = \Gamma(\eta, \xi) * \begin{cases} (L + \eta)\delta(\xi) & -L \leq \eta \leq 0 \\ (L - \eta)\delta(\xi) & 0 < \eta \leq L \end{cases}. \quad (4.5)$$

with  $\Gamma(\eta, \xi)$  the ACF of the system PSF. Again a translation and rotation can be introduced on the second convolution factor in the right hand side of eq. 4.5. Only the rotational transformation will be employed here, since a rotated fibre results in an ACF that is likewise rotated, but remains positioned at the centre of the ACF, independent of its position in the image. Note that both eq. 4.1 and eq. 4.5 can be expressed in closed form. Also, eq. 4.5 is not only the ACF of a single fibre, but can be used directly to analyze the ACF of an image containing perfectly aligned and randomly positioned fibres.

The ACF of an image containing randomly positioned fibres will represent the autocorrelation of all fibres. Because of the positional randomness, all fibres are considered to be independent of each other meaning that on average no cross correlation should exist. This implies that the ACFs of all individual fibres simply accumulate at the origin of the autocorrelation space. When assuming that all possible orientations are equally likely, the ACF can be written as a continuous sum over all possible orientations. For practical implementation this sum can be approximated by a discrete sum of individual fibre ACFs to as few as one single fibre ACF for every 10 degrees ( $N = 18$ ). In general the ACF can be written as

$$g(\eta, \xi) = g_{00} \left| \sum_{i=1}^N g_{\theta_i}^1(\eta, \xi) \right|, \quad (4.6)$$

where  $g_{\theta_i}^1(\eta, \xi)$  represents the ACF of a single fibre under a rotational basis transformation by an angle  $\theta_i$ ,  $g_{00}$  is the effective ACF amplitude for which the information content will be discussed in section 4.3.3, and the notation  $|\dots|$  takes care of the normalization of the sum to unity amplitude. The angles  $\theta_i$  are set to be equally spaced between 0 and 180 degrees.

When an image is made up of fibres that have an intensity modulation as for the P-SHG effect, the shape of the ACF is altered. In case all orientations are represented equally in the image, the intensity variation can be included in eq. 4.6 by introducing a modulation function inside the sum. When the intensity of every fibre is modulated, the rotated single fibre ACF must be multiplied by the square of the angular modulation function (e.g. eq. 4.3),

$$g(\eta, \xi) = g_{00} \left| \sum_{i=1}^N g_{\theta_i}^1(\eta, \xi) p^2(\theta_i) \right|. \quad (4.7)$$

### 4.3.3 ACF amplitude

In the case of sub-resolution beads, the ACF amplitude is known to be inversely proportional to the average number of particles positioned inside the observation area of the system PSF ( $A_{\text{PSF}}$ ) [79], and hence relates to the surface density of the beads ( $n$ ):

$$g_{00} = (nA_{\text{PSF}})^{-1}. \quad (4.8)$$

In the case of fibres, a similar relation can be derived. For this, assume the image consists of a collection of dispersed beads that are imaged by a PSF with the shape of a single fibre as defined by eq. 4.1. Then, the ACF amplitude is related to the number of beads inside the observation area of that particular PSF. Stated otherwise, the ACF amplitude is inversely proportional to the number of centres of fibres positioned inside the observation area of an imaged fibre. Both the system PSF and the length of the fibre are determining parameters for this observation area. So in general the amplitude of the ACF is equal to

$$g_{00} = (nA_f^L)^{-1} \quad (4.9)$$

with  $A_f^L$  the observation area of an imaged fibre with length  $L$  obtained in the same way the surface of the system PSF is calculated [79];  $n$  is the fibre density given by the ratio of the number of fibres of which the centre lies within the image field of view and the area of the field of view.

In case of an intensity modulation of the individual fibres, such as the P-SHG effect, not every orientation contributes equally to the amplitude of the ACF. Based on the correction used in fluorescence correlation spectroscopy for multiple species of different fluorescent brightness [80], one can show that the ACF amplitude has to be modified to (see supplementary material 4.9.1)

$$g_{00} = \frac{\langle p^2(\theta) \rangle_{\theta}}{\langle p(\theta) \rangle_{\theta}^2} \cdot \frac{1}{nA_f^L}. \quad (4.10)$$

This is similar to the correction used in fluorescence correlation spectroscopy with multiple species of different fluorescent brightness [80]. For typical values of the tensor element ratios in case of type I collagen ( $d_{31}/d_{15} = 1$ ,  $d_{33}/d_{15} = 1.4$ ) the correction factor is approximately 1.06.

The effect on the ACF amplitude by the noise induced by the detectors can be accounted for by the correction suggested by Koppel *et al.* [81],

$$g_{00} = g_{00}^e \left( 1 - \frac{\langle \Delta(x, y) \rangle_{xy}}{\langle I(x, y) \rangle_{xy}} \right)^{-2} \quad (4.11)$$

with  $g_{00}^e$  the experimentally obtained amplitude by fitting with the described model, and  $\Delta(x, y)$  an image containing only the system noise. Such an image is typically obtained by performing a scan without excitation light.

Finally, in the specific case of a collagen type I hydrogel, the ACF amplitude can phenomenologically be linked to the effective tropocollagen density  $\rho$ . Assuming a hexagonal packing of tropocollagen molecules, and a cylindrical shape with final diameter  $D$  and length  $L$ , the ACF amplitude can be shown to be given by (see supplementary material 4.9.2)

$$g_{00} = \frac{1}{\rho} \cdot \frac{\mu\pi D^2}{2\sqrt{3}CV_{\text{PSF}}d^2l} = \frac{K}{\rho} \quad (4.12)$$

where  $\mu$  is the molecular mass of type I tropocollagen ( $\sim 300$  kDa),  $V_f^L$  and  $V_{\text{PSF}}$  is the volume of an imaged fibre of length  $L$  and the system PSF volume respectively,  $d$  (1.5 nm) is the distance between tropocollagen molecules, and  $l$  (340 nm) is the tropocollagen length combined with the gap between successive staggered molecules (values obtained from [82]). Basically eq. 4.12 converts the number of tropocollagen molecules into the average number of fibres considered in eq. 4.9. In case the fibre length is at least one order of magnitude larger than the PSF size, the convoluted fibre volume can be related to the PSF volume and the length of the fibre by  $V_f^L \approx C \cdot L \cdot V_{\text{PSF}}$ , with  $C$  a constant which is typically about  $1.72 \mu\text{m}^{-1}$  for a  $0.33 \mu\text{m}$  PSF size. This makes the relation between the ACF amplitude and the hydrogel density independent of the length of the formed fibres.

## 4.4 Materials and methods

### 4.4.1 Hydrogel

Hydrogels were made from a bovine collagen type I solution Nutragen® (Advanced BioMatrix, USA) supplied as a 6 mg/mL aqueous solution in 0.01 M HCl with a pH value of 2.0. Gels with a collagen concentration of 4.8 mg/mL were prepared on ice by quickly mixing Nutragen® collagen solution, 1x PBS and 10x minimal essential medium (MEM, Sigma, Bornem, Belgium) with a 8:1:1 ratio. The collagen solution was neutralized (pH between 7.2 – 7.4) by dropwise addition of 1 M NaOH, assessed by colour change of the phenol red pH indicator, and diluted 3:4 fold serially with 1x PBS to obtain solutions with a collagen concentration of 3.6, 2.7, 2.02 and 1.52 mg/mL. The neutralized solutions (150 µL per condition) were transferred to a 8-well glass chamber slide (Lab-Tek®II, Nalge Nunc International, Rochester, NY, USA) and incubated overnight at 37 °C to allow polymerization.

### 4.4.2 Microscopy

SHG imaging is performed using a Zeiss LSM510 META (Carl Zeiss, Jena, Germany) mounted on an Axiovert 200M and a 40x/1.1 water immersion objective (LD C-Apochromat 40x/1.1 W Korr UV-VIS-IR, Carl Zeiss). In order to sufficiently sample the PSF a pixel size of 87.9 nm is chosen for 1024x1024 pixels per images yielding a field of view of 90 µm. The excitation is provided by a femtosecond pulsed laser (MaiTai DeepSee, Spectra-Physics, CA, USA) tuned to a central wavelength of 900 nm. The excitation light was linearly polarized. An analogue photomultiplier tube, delivered by Zeiss, is used for backward detection in non-descanned mode after the signal passes through a 50 nm wide band pass filter with a central wavelength of 430 nm. The images are taken 20 µm above the cover glass to reduce possible distortion of the optical point spread function by the sample itself. Microscopy is performed at 37 °C.

### 4.4.3 Simulations

The length of the simulated fibres is drawn from a Gaussian distribution to include length variability and mimic the 3D nature of a hydrogel. The standard deviation of the Gaussian is 40% of the mean value  $\langle L \rangle$ . The system noise is assumed to be Gaussian with an intensity dependent standard deviation. This dependency was determined for the used system, and the resulting noise is superimposed onto the simulated image. The SHG tensor element ratios are set to  $d_{31}/d_{15} = 1$  which accounts for Kleinman symmetry, and  $d_{33}/d_{15} = 1.44$  which lies in the typical range of reported values for collagen type I under Kleinman conditions and is a reported value for collagen from tendon [83]. The Gaussian system PSF is set to be symmetric with a  $e^{-2}$  value of 0.33 µm which is acceptable for the described experimental setup.

## CHAPTER 4

---

**Table 4.1:** Overview of the parameters of the three different models. Blank cells mean the parameter is not included in the model, PSF indicates that the value is fixed at the simulation PSF and f indicates that it is a free parameter.

	$g_{00}$	$w_x$	$w_y$	$L$	$d_{31}/d_{15}$	$d_{33}/d_{15}$
Gaussian	f	f	f			
Robertson	f	PSF/f	PSF/f			
'Proposed model'	f	PSF/f	PSF/f	f	f	f

Every condition is simulated 25 times with 1024x1024 pixels per image and a pixel size of 87.9 nm, in accordance with the experimental conditions. The fibre density of the hydrogel is set to  $1/\mu\text{m}^2$ .

### 4.4.4 Analysis

The different models are fitted to the simulated or experimental ACF by performing non-linear least squares algorithm using the built-in function `lsqnonlin` from Matlab (The MathWorks). An unweighted ACF fit is performed on the central 64x64 pixels, excluding the noise-containing zero lag value. An overview of the free and fixed analysis parameters for the studied models is given in Table 4.1. For the Gaussian model the width is a freely adjustable parameter since it was claimed to be dependent on the mechanical properties of the sample [7]. A full expression of the Gaussian model and Robertson's model is provided in the supplementary materials section 4.9.3.

### 4.4.5 Point spread function

The system PSF was measured using ZnO nano-particles with an average diameter of 35 nm (Sigma-Aldrich, Schnellendorf, Germany) dried onto a glass cover slip. The PSF size was extracted from the data by analyzing the ACF of the image using a symmetrical 2D Gaussian fit, yielding a value of  $w_x = w_y = 0.333 \pm 0.003 \mu\text{m}$ .

## 4.5 Results

### 4.5.1 ACF shape particularities

Using an experimental dataset (Fig. 4.1.a), the ACF model introduced in section 4.3.2 was tested and compared to different models described in literature. The results obtained according to the approach introduced by Raub *et al.* [46] which is based on the expression of regular ICS for beads, as well as by the model of Robertson *et al.* [47] in which the ACF is regarded as a correlation probability function, are shown for comparison with the proposed autocorrelation model. In the experimental data, a distinct ACF shape can be observed (inset Fig. 4.1.a) which is considered to be a direct consequence of the P-SHG effect (Eq. 4.3). Using a set of parameters similar to the experimental conditions, a simulation was performed (Fig. 4.1.b) for which the contours of the ACF are shown (inset Fig. 4.1.b). Qualitatively, an ACF shape similarly to that of the experimental data is observed for the simulated data, indicating that the proposed simulation model indeed agrees with the real case.

The applicability of the different models is tested by comparing the residuals resulting from the fitting procedure as described in section 4.4.4. Both the resulting ACF normalized to unit amplitude (Fig. 4.1.c-e) as well as their corresponding residuals (Fig. 4.1.f-h) are shown. From the latter it can be concluded that our model agrees well with the ACF of the experimental data. The residuals show less pronounced deviations with a maximum of approximately 3% of the resulting ACF amplitude, compared to up to 15% for the Gaussian model.

### 4.5.2 Evaluation of parameter recovery by simulations

The validity and correctness of the proposed model was tested on a simulated dataset, and compared to the Gaussian and Robertson's approach. Parameter recovery was tested for various fibre lengths (Fig. 4.2) since the ACF shape is mainly dictated by the additional correlation along the fibre axis. The other parameter values are as described in section 4.4.4. For the results shown, the PSF parameters were fixed to their true values. The corresponding mean and standard deviation of the values resulting from fitting are shown in Fig. 4.2. The analysis was also done for freely adjustable PSF widths giving similar results but slightly increased standard deviations for the discussed parameters (data not shown). A first measure for the appropriateness of the model is the correct recovery of the ACF amplitude (Fig. 4.2.a). For the three models, the fitted amplitude is compared to the expected one (dashed line). The latter is obtained by taking into account the length of the fibre combined with the P-SHG intensity modulation (eq. 4.10), and the noise correction (eq. 4.11). Note that error bars are only shown for the proposed model. The standard deviation was similar for the three models indicating that the parameter spread originated from data variability rather than incorrect parameter recovery. The right axis (dash-dotted) points out the

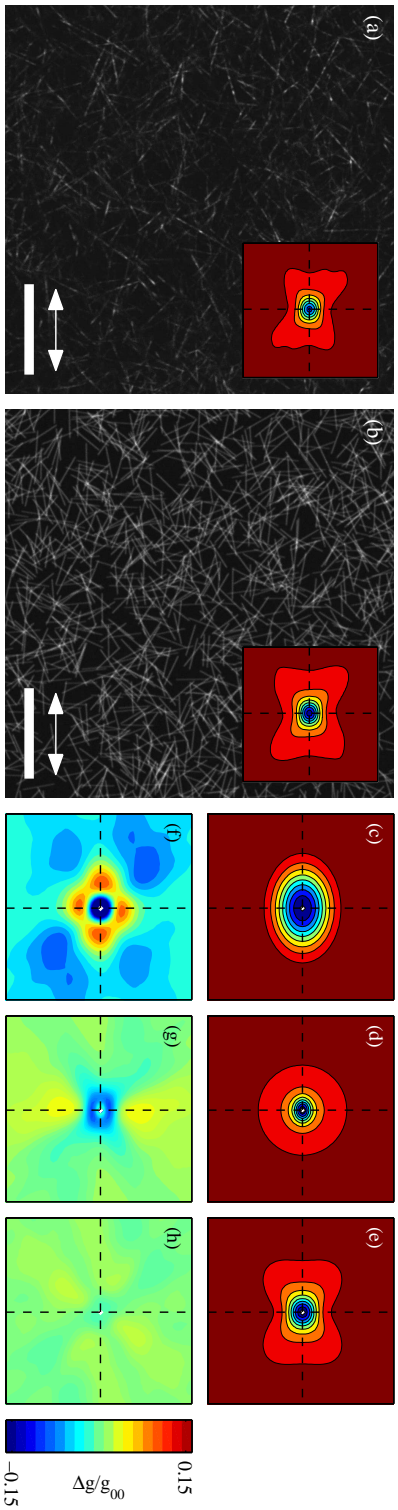


**Figure 4.1:** (a) Typical SHG image of a collagen type I hydrogel (4.8 mg/mL). (b) Simulated image as described in section 4.4.3 using parameters retrieved from analysing real data, shown in (a), by our model ( $n = 0.18$ ,  $\langle L \rangle = 7.17 \mu\text{m}$ ,  $d_{31}/d_{15} = 1.5$ ,  $d_{31}/d_{15} = 1.9$ ). The insets show a contour plot of the normalized ACFs, scale bar = 20  $\mu\text{m}$ ; the double arrow indicates the fundamental polarization direction. (c-e) Contour plots of the ACF fitted to the ACF of the real data shown in (a) by the Gaussian model [46], the model introduced by Robertson *et al.* [47] and the proposed model (eq. 4.7) respectively. (f-h) Contour plot of accompanying residuals normalized to  $g_{00}$  of the ACF fit. The colour scale is identical for the three cases. For all ACF and residual plots, the central 64x64 pixels are shown.

actual theoretical ACF amplitude value as a reference.

Robertson's model [47] seems to underestimate the amplitude but approaches the expected value for fibre lengths substantially larger than the width of the system PSF, matching the range for which this model is basically developed. In this range, this model also seems to be able to ignore the P-SHG effect, despite the fact that the ACF is shaped asymmetrically (Fig. 4.1.d and Fig. 4.1.e). This could be explained by unequal resulting fit values for both lateral PSF dimensions. The Gaussian model on the other hand gives a correct estimate for the amplitude for fibres shorter than the system PSF since in this length range, the fibres are merely imaged as diffraction limited objects. However, for longer fibres the amplitude is consistently underestimated since here the ACF shape changes to a non-Gaussian profile, as was already indicated by Robertson *et al.* [47]. The interval defined by fibre lengths in the order of the PSF size up to about 15 times this PSF size, seems to be a transition region where both the Gaussian and Robertson's model fails. Our proposed model works well for diffraction limited fibres, longer fibres and fibre lengths in the model transition zone.

In contrast to Robertson's and the Gaussian approach, our proposed model allows for the determination of the average length of the fibres (Fig. 4.2.b) and second order hyperpolarizability tensor element ratios (Fig. 4.2.c-d). Again a transition is observed at the PSF size. For objects substantially smaller than the PSF width an incorrect estimate is observed for both the length and the tensor element ratios. This is due to the fact that in this range the ACF is merely a Gaussian defined by the PSF. On the other hand, for objects longer than the width of the PSF all parameters are recovered correctly with standard deviations as low as  $\sim 3\%$ . For increasing fibre length the accuracy of the fitted length decreases and a relative error of  $\sim 10\%$  is obtained for average fibre lengths of  $\sim 15$  times the PSF size. Regarding the tensor element ratios, a good estimate persists since the angular modulation effect of the ACF remains present, independent of the fibre length for lengths above the PSF width.

### 4.5.3 Dilution series

The models discussed above were applied to a dilution series of a collagen type I hydrogel. For interpretation and representation of the results (Table 4.2) it was assumed that the collagen density has no effect on the system PSF, the average collagen fibre length and the SHG tensor elements (eq. 4.3). This implies that the number of fibres per unit area does increase, and hence the amplitude of the ACF is altered (Fig. 4.3).

Both the Gaussian and the Robertson's approach yielded unequal and deviating values for the width of the system PSF in the two lateral directions. These deviations are due to the fact that the symmetry of the actual ACF (see Fig. 4.1.a.) is different from the shape implicitly assumed in these methods. For a fixed PSF size, Robertson's model results in underestimated ACF amplitudes and values similar to the incorrect Gaussian fit are obtained. The approach proposed in this work yields

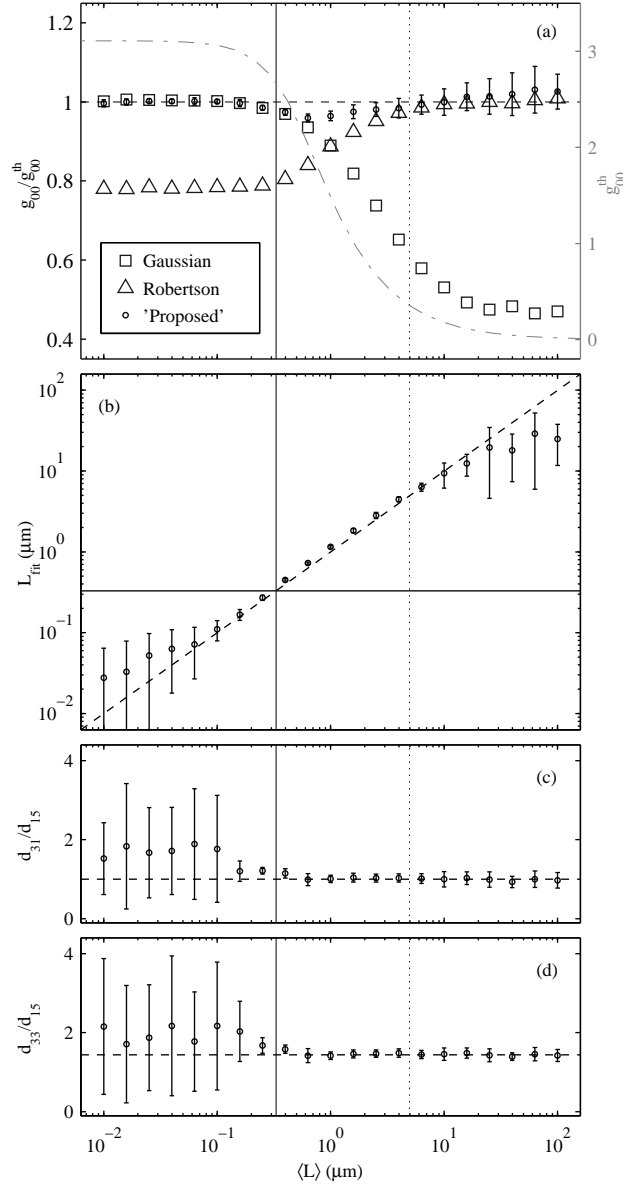


**Figure 4.2:** Parameter recovery of simulated datasets. The simulation is described in section 4.4.3, and the analysis is done with the three different models as described in the text. The PSF parameters are fixed to their true value. The mean with standard deviation of the 25 simulation per average length is given for every freely adjustable parameter. Panel (a) shows only the standard deviation for the proposed model since this was similar for the three models; the right axis (gray) gives the true value of the ACF amplitude,  $g_{00}^{th}$  and is represented by the dash-dotted gray line. In all panels the dashed line indicates the expected value. The vertical line solid represents the system PSF width ( $w_x = w_y = 0.33 \mu\text{m}$ ), and the vertical dotted line represents 15 times the PSF width

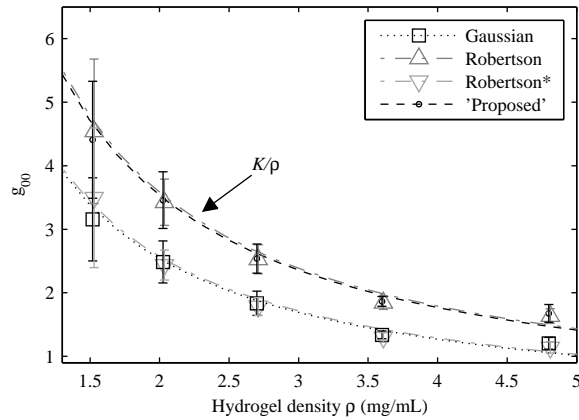


**Figure 4.3:** Mean and standard deviation of the fitted ACF amplitude as function of hydrogel density in the hydrogel dilution series. The expected  $K/\rho$  relation (eq. 4.12) is observed and the dashed lines represent the corresponding fits (see Table 4.2 for the resulting  $K$  values). The asterisk indicates that the PSF width was fixed at  $0.33 \mu\text{m}$ . The results obtained with the proposed model were essentially similar for the freely adjustable and fixed PSF parameter.

excellent values for the PSF size when set as a free fit parameter. Independent of this, the tensor elements ratios fall within the range of values obtained for collagen of adult *Xenopus* aorta [83]. The average resulting fibre length is at least 15 times larger than the PSF ( $\approx 4.8 \mu\text{m}$ ), which according to the simulations, is near the working range for extracting the length information.

The relation between the resulting ACF amplitude, corrected for the system noise and the P-SHG effect, and the hydrogel density was compared to the expected  $K/\rho$  relation (eq. 4.12), as shown in Fig. 4.3. Again the Gaussian fit results in lower values compared to the proposed method. However, in case of a freely adjustable PSF size, Robertson's approach leads to similar values as those obtained by our model. This is in agreement with the amplitude recovery observed in the simulations for fibres that are sufficiently larger than the PSF (Fig. 4.2.a). In contrast, fixing the PSF width results in an underestimated ACF amplitude for all considered concentrations due to the asymmetric nature of the ACF induced by the P-SHG effect. Nevertheless, for all three models the data obey the  $\rho^{-1}$  relation and the resulting proportionality parameters  $K$  are given in Table 4.2. Using eq. 4.12, this parameter is used to calculate the average fibre diameter (Table 4.2). For the three different models, the obtained diameters are within the typical range for collagen fibres (10 – 100 nm) inside a hydrogel

**Table 4.2:** Overview of the analysis of real hydrogel data collected at different densities. For each density 7 images were acquired at a random position. The mean with standard deviation taken over all images for all densities are shown for the obtained system PSF, SHG tensor elements and average fibre length.

	$w_x$ ( $\mu\text{m}$ )	$w_y$ ( $\mu\text{m}$ )	$d_{31}/d_{15}$	$d_{33}/d_{15}$	$L_{\text{ave}}$ ( $\mu\text{m}$ )	$K^a$ ( $\text{mg}/\text{mL}$ )	$D^a$
Gaussian	$0.99 \pm 0.11$	$0.71 \pm 0.08$				$4.9 \pm 0.3$	$48 \pm 3$
Robertson	$0.26 \pm 0.02$	$0.18 \pm 0.02$				$6.9 \pm 0.3$	$57 \pm 3$
Robertson*	$0.33^*$	$0.33^*$				$5.1 \pm 0.3$	$49 \pm 4$
'Proposed'	$0.32 \pm 0.01$	$0.34 \pm 0.01$	$1.5 \pm 0.4$	$1.8 \pm 0.4$	$6 \pm 2$	$6.8 \pm 0.3$	$56 \pm 3$
'Proposed'*	$0.33^*$	$0.33^*$	$1.5 \pm 0.4$	$1.9 \pm 0.5$	$7 \pm 2$	$6.9 \pm 0.4$	$57 \pm 4$

<sup>a</sup>  $K$  and  $D$  as defined in eq. 4.12.

\*parameter was fixed at the given value.

## 4.6 Discussion

Although the structure of a fibrous hydrogel is more and more assessed by means of image correlation spectroscopy, a detailed description of the resulting autocorrelation function related to P-SHG images of collagen type I hydrogels was never described. To improve the ACF analysis in this context, we developed a new, rigorous model that is based on the underlying fibrous structure, and extensively tested its validity and applicability. We want to emphasize that, as opposed to the Gaussian method, the parameters for our proposed model are related to real physical quantities such as the P-SHG tensor element, the mean length of the fibres in a certain length range, and the effective PSF size. Although the latter is included in Robertson's approach as well, it is necessary to set the PSF width as a free fit parameter in order to obtain good estimates of the ACF amplitude when analyzing SHG images of collagen type I hydrogels. This results in unequal lateral PSF dimensions that do not agree with the real system PSF size, which is a direct consequence of the irregular ACF shape due to the P-SHG effect. By including the latter effect into the proposed model, we are able to correct for this.

For designing an ACF model of fibre like structures, it is often assumed that all fibres are lying in the imaging plane, representing only 2D situations [47, 78]. To mimic the 3D nature of a real hydrogel, but also to incorporate intrinsic fibre length variations, we have included a normal length variation with a standard deviation of 40% of the mean fibre length. Still, in reality it holds that fibres tilted out of the imaging plane do not only appear shorter, they also possess an intensity variation along their direction due to the axial resolution of the imaging system. Moreover, in case of P-SHG an additional fibre intensity modulation is present that is related to an out of plane angle. Implementing both the out of plane tilting and the 3D P-SHG effect requires additional work, but could lead to better length and P-SHG tensor ratio estimates. Yet, the currently proposed ACF model resulted in the best residuals out of the three compared models (Fig. 4.1.f-h), and the resulting fit values from the experimental data do fall within the expected ranges (Table 4.2). Moreover, a very good estimate is obtained for the system PSF width and similar P-SHG parameters have been reported in literature before [83].

The current work was inspired by the work done by Raub *et al.* [46] in which great effort was put in evaluating the possibility of probing the hydrogel mechanical properties by image correlation spectroscopy. They suggest that the rheological storage modulus is related to the average fibre thickness, which they proved to be proportional to the width of the Gaussian function fitted to the ACF of subjectively thresholded SHG images, and to the pore size which is determined by direct image processing. The latter can also be obtained directly from the ACF. In this context, Eichhorn and Sampson [77] show that the pore size of a 2D random network is inversely proportional to the product of the fibre density and the average length of the fibres for fibres much longer than their diameter. In this limiting case, eq. 4.9 shows

that the ACF amplitude is proportional to that very same product since it also holds that  $L \gg w$  implying that  $A_f^L \approx C \cdot L \cdot A_{\text{PSF}}$ . The average thickness of the fibre could be included in the fitted PSF width for our proposed method. However, this width increases a maximum of 1% for fibre thicknesses up to 25% of the PSF size, resembling the thickness of the considered fibres ( $\sim 80$  nm). Prior knowledge of the collagen density in combination with eq. 4.12 however provides an alternative method to estimate the local fibre thickness. All the above mentioned emphasizes the need for an appropriate theoretical model in applying image correlation spectroscopy to assess the local mechanical properties of random fibre networks.

In this work we mainly focussed on the applicability of the different models on random fibre networks which are imaged using label-free SHG microscopy, including the SHG polarization effect. We proved that the latter is important to cope with the angular modulation observed in the experimental ACF, and obtained acceptable values for the P-SHG parameters. Yet, because of the way the model is defined it can be adjusted to be applicable in any kind of fibre like image. The ACF of images of fluorescently labelled collagen fibres inside a hydrogel could be analyzed using eq. 4.6, as well as bright field images of any random fibre network. Additionally, any orientation distribution can be included, by replacing  $p(\theta)^2$  in eq. 4.7, to study for instance the mean fibre direction with its angular spread in images containing preferentially oriented fibre like structures [84]. Still, one has to be careful in extending the number of free fit parameters when introducing custom modulation functions. Necessary parameters that are not of interest and could be determined *a priori* should be set fixed to avoid erroneous fitting and dubious results. Nevertheless, despite the fact that our proposed method is complex and computationally intensive as opposed to the Gaussian and Robertson's model, we claim that it is a flexible method making it versatile in its application range. Moreover, when using the proper modulation function, either for intensity modulation or preferential orientation, it is a very robust method in that no prior and subjective image processing is required to obtain reliable quantitative results.

### 4.6.1 Addendum

Although SHG is a coherent process, we applied here the theory for fluorescence correlation spectroscopy. It is however known that, besides the polarization effect, coherency affects the shape and, mainly, the amplitude of the ACF [85]. Slenders *et al.* [85] state that for sufficiently low concentrations of point scatterers, the coherent ACF resembles that of fluorescence. Considering the images in this work, fibres only overlap at their crossings, while the majority of a fibre is not in the vicinity of other fibres. This could explain the resemblance between our experimental data and simulations using the incoherent model. Undoubtedly, more work is required to adjust the current model for coherent scattering. Although, for the studied densities, the incoherent model seems to be a valid approximation for SHG ICS.

## 4.7 Conclusion

We introduced an alternative model to analyze the ACF of an SHG image of random fibre networks obtained with linearly polarized incident light. Besides an accurate parameter recovery such as the system PSF and the ACF amplitude, simulations prove that this model can be used to measure the P-SHG related non-zero susceptibility tensor element ratios from a single image. Additionally, the fibre length can be obtained for lengths up to 15 times the PSF size. For the ACF amplitude in particular, an inverse proportional relation with the effective tropocollagen density was derived and observed. This relation was used to estimate the average collagen fibre thickness.

## **4.8 Acknowledgements**

This research is part of the Interreg EMR IV-A project BioMIMedics ([www.biomim-edics.org](http://www.biomim-edics.org)), and is co-financed by the European Union, local governments, research institutes and SMEs.

M.A. acknowledges the Federal Science Policy of Belgium (IAP-7/05), the support by the FWO-onderzoeksgemeenschap "Scanning and Wide Field Microscopy of (Bio)-organic Systems", and the Province of Limburg (Belgium) for the financial support within the tUL IMPULS FASE II program allowing for the upgrading the laser source used in this work.

## 4.9 Supplementary material

### 4.9.1 Correlation amplitude correction due to intensity modulation

Correlation amplitude correction due to intensity modulation Because of the similarities between fluorescence correlation spectroscopy (FCS) and image correlation spectroscopy, the autocorrelation amplitude correction is explained using the correlation amplitude for FCS with  $R$  different species as given by [80],

$$g_{00} = \frac{1}{A_{\text{PSF}}} \cdot \frac{\sum_{i=1}^R \alpha_i^2 \langle n_i \rangle}{\left[ \sum_{i=1}^R \alpha_i \langle n_i \rangle \right]^2} \quad (4.13)$$

Here,  $A_{\text{PSF}}$  is the observation area as defined in [79],  $\alpha_i$  is proportional to the brightness of species  $i$ , and  $n_i$  represent its density as number of emitting items per unit area. When assuming that every possible brightness is evenly likely, there is no interspecies difference in density. Then  $\langle n_i \rangle = n_s$ , with  $n_s$  the individual densities for the species. This, combined with equation 4.13 leads to

$$g_{00} = \frac{1}{n_s A_{\text{PSF}}} \cdot \frac{\sum_{i=1}^R \alpha_i^2}{\left[ \sum_{i=1}^R \alpha_i \right]^2} = \frac{1}{n A_{\text{PSF}}} \cdot \frac{\langle \alpha^2 \rangle}{\langle \alpha \rangle^2} \quad (4.14)$$

where  $n = Rn_s$  is the total density for all species combined in the image plane.

### 4.9.2 Autocorrelation amplitude for a collagen type I hydrogel

Commercially available collagen type I hydrogel state the tropocollagen density ( $\rho$ ) of the stock solution, typically given in mg/mL. To convert this density to a fibre density inside the hydrogel, some assumptions are made based on structural properties of collagen type I fibres as obtained by electron microscopy observation (Fig. 4.4.a). The fibres are composed of a hexagonal packing of tropocollagen molecules, which have a mass of  $\mu = 300$  kDa, and a length of 300 nm [82]. The distance  $d$  between parallel tropocollagen molecules is about 1.5 nm and a serial gap of 40 nm exists between them resulting in a length  $l = 340$  nm per tropocollagen molecule. Since laterally neighboring tropocollagen molecules are shifted 67 nm with respect to each other, the packing shown in Fig. 4.4.a yields the typical striated pattern along the collagen fibre as observed by electron microscopy. The volume a tropocollagen molecule occupies is therefore given by

$$V_{\text{tropo}} = S_u l = \frac{\sqrt{3}d^2}{2} l. \quad (4.15)$$

Then, the total number of tropocollagen molecules inside a cylindrical collagen fibre

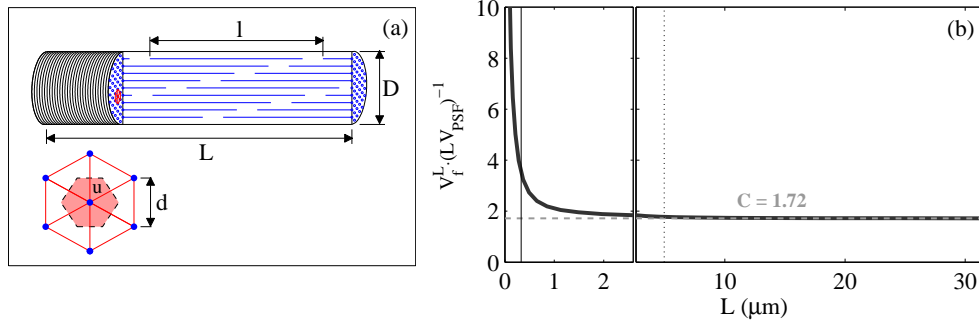


**Figure 4.4:** Mean and standard deviation of the fitted ACF amplitude as function of hydrogel density in the hydrogel dilution series. The expected  $K/\rho$  relation (eq. 4.12) is observed and the dashed lines represent the corresponding fits (see Table 4.2 for the resulting  $K$  values). The asterisk indicates that the PSF width was fixed at  $0.33 \mu\text{m}$ . The results obtained with the proposed model were essentially similar for the freely adjustable and fixed PSF parameter.

of length  $L$  and diameter  $D$  ( $N_{\text{tropo}}$ ) becomes

$$N_{\text{tropo}} = \frac{V_{\text{fibre}}}{V_{\text{tropo}}} = \frac{\pi D^2 L}{2\sqrt{3}d^2 l}. \quad (4.16)$$

This allows us to calculate the fibre density  $n$  for a given tropocollagen density  $\rho$ , by first converting into a number density ( $n_{\text{tropo}} = \rho/\mu$ ).

$$n = \frac{n_{\text{tropo}}}{N_{\text{tropo}}} = \left( \frac{\mu\pi D^2 L}{\rho 2\sqrt{3}d^2 l} \right). \quad (4.17)$$

Given the fact that the amplitude of the autocorrelation function ( $g_{00}$ ) for a hydrogel is defined by  $(nV_f^L)^{-1}$ , with  $V_f^L$  the observation volume shaped as a fibre of length  $L$ , it holds that

$$g_{00} = \frac{1}{V_f^L} \cdot \frac{\mu\pi D^2 L}{\rho 2\sqrt{3}d^2 l}, \quad (4.18)$$

Note that observation volume is used over area now because of the 3D nature of a real hydrogel opposed to the 2D case of the simulations. Finally we can use the assumption that  $V_f^L \approx C \cdot L \cdot V_{\text{PSF}}$  for fibres longer than  $\sim 15$  times the PSF size (Fig. 4.4.b). The autocorrelation amplitude is then given by

$$g_{00} = \frac{1}{\rho} \cdot \frac{\mu\pi D^2}{2\sqrt{3}C V_{\text{PSF}} d^2 l} \quad (4.19)$$

All mentioned values are obtained from [82].

### 4.9.3 Model overview

The model proposed in the paper is compared to the Gaussian model which is given by

$$g(\eta, \xi) = g_{00} \exp \left[ - \left( \frac{\eta^2}{w_x^2} + \frac{\xi^2}{w_y^2} \right) \right] \quad (4.20)$$

and Robertson's model defined as [47]

$$g(\eta, \xi) = g_{00} \left[ \frac{1}{1 + \pi \sqrt{\eta^2 + \xi^2}} \right] * \left[ \frac{1}{\pi w_x w_y} \exp \left[ - \left( \frac{\eta^2}{w_x^2} + \frac{\xi^2}{w_y^2} \right) \right] \right] \quad (4.21)$$

with \* representing the convolution.

### 4.9.4 Coordinate system

In this chapter a different coordinate system was used than that in section 2.4. While here the  $z$ -axis is used as symmetry axis, the  $x$ -axis is considered as symmetry axis in the theory chapter. This implies the tensor element indices are interchanged using the following rules:  $d_{11} \leftrightarrow d_{31}$ ,  $d_{12} \leftrightarrow d_{33}$  and  $d_{26} \leftrightarrow d_{15}$ .



## **CHAPTER 5**

---

# **On the interpretation of second harmonic generation intensity profiles of striated muscle**

---

**Paesen, R.**, Smolders, S., Notelaers, K., Wens, I., de Hoyos Vega, J. M., Eijnde, B. O., Hansen, D. & Ameloot, M. On the interpretation of second harmonic generation intensity profiles of striated muscle. *J. Biomed. Opt.* (2015)

## 5.1 abstract

Recently, a supra-molecular model was developed for predicting striated skeletal muscle intensity profiles obtained by label-free second harmonic generation (SHG) microscopy. This model allows for a quantitative determination of the length of the thick filament anti-parallel range or M-band ( $M$ ), and results in  $M = 0.12 \mu\text{m}$  for single band intensity profiles when fixing the A-band length ( $A$ ) to  $A = 1.6 \mu\text{m}$ , a value originating from electron microscopy (EM) observations. Using simulations and experimental data sets, we showed that the objective numerical aperture and the refractive index (RI) mismatch ( $\Delta n = n_{2\omega} - n_{\omega}$ ) between the illumination wave ( $\omega$ ) and the second harmonic wave ( $2\omega$ ) severely affect the simulated sarcomere intensity profiles. Thereby, our recovered filament lengths did not match with those observed by EM. For an RI mismatch of  $\Delta n = 0.02$ , and a moderate illumination numerical aperture of 0.8, analysis of single band SHG intensity profiles with freely adjustable A- and M-band size yielded  $A = 1.40 \pm 0.04 \mu\text{m}$  and  $M = 0.07 \pm 0.05 \mu\text{m}$  for skeletal muscle. These lower than expected values were rationalized in terms of the myosin density distribution along the myosin thick filament axis. Our data provided new and practical insights for the application of the supra-molecular model to study SHG intensity profiles in striated muscle.

## 5.2 Introduction

Second harmonic generation (SHG) microscopy have been demonstrated to be an excellent tool for label-free imaging of several biological structures. The well defined properties of the SHG signal makes it convenient to study well ordered structures such as collagen type I rich structures [22, 44, 86, 87], microtubules inside mitotic spindles or neurons [12, 88, 89] and striated muscle containing myosin thick filaments [36, 63, 90, 91]. SHG microscopy relies on the presence of non-centrosymmetric features, achieved through a high degree of order of polar biomolecules. This implies that even the smallest changes in this structural regularity have a detrimental effects on the resulting SHG signals, making SHG microscopy one of the tools for early detection of reorganization of SHG active molecules.

Disorder of otherwise perfectly aligned myosin thick filaments is known to occur within muscle tissue, either as a primary consequence of muscle targeting disease such as Nemalin myopathy [92] or Pompe's disease [93], or as secondary effects of muscle disuse [94]. Various studies have recently emerged suggesting SHG microscopy to be a valuable label-free tool to study muscular disorder [93, 95, 96]. However, to fully understand the effect of muscle degradation on the SHG signal, detailed knowledge of sarcomere structures and their relation to the second harmonic signal generation is necessary.

Striped SHG patterns are typical for skeletal and cardiac muscle [36, 63, 91, 97]. Two SHG based approaches have been used to quantify these striations [36, 96, 98]. Both methods are based on analysing a 1D intensity profile, mostly extracted from 2D SHG images. The first approach relies on a phenomenological profile definition such as a double Gaussian peak [96, 98]. This is useful for analysing double peaked intensity profiles observed in cardiac muscle tissue, but apart from the sarcomere length, the resulting parameter values have no direct relation to biological structural properties of sarcomeres. The second approach is developed by Rouède *et al.* [36], and relies on a more rigorous model based on the molecular organization of sarcomeres. Starting from the Maxwell equations, they derive electric field expressions for far-field SHG radiation to predict intensity profiles. In this so called supra-molecular model, the SHG signal is assumed to originate from the thick filament (A-band), consisting of two oppositely directed non-centrosymmetric hemi-filaments. This reversed directionality leads to a  $\pi$  phase difference between the SHG signals coming from both hemi-filaments, and makes the thick filament centrosymmetric where the hemi-filaments connect and overlap (M-band). By including these features, the model comprises the A-band length ( $A$ ), M-band length ( $M$ ) and sarcomere length ( $L$ ) as biological structural parameters (Fig.5.1a). Besides these structural parameters, microscope related parameters such as the optical point spread function (PSF) and the numerical aperture (NA) of the signal collection optics are implemented in the model.

To use the supra-molecular model, Rouède *et al.* [36] sets the A-band length to  $A = 1.6 \mu\text{m}$ , a generally accepted value observed by electron microscopy (EM)[99,

100]. Fitting the experimental profiles then yields the sarcomere length and the M-band size as biologically relevant parameters. For healthy skeletal muscle tissue, consisting of single peaked SHG intensity profiles, an M-band length of  $M = 0.12 \mu\text{m}$  results [36], being smaller than the EM related value of  $M = 0.15 \mu\text{m}$  previously described [99, 100]. This shorter length is assumed to be a consequence of unaccounted spherical aberrations [36]. However, when applying the supra-molecular model as suggested by Rouède *et al.* [36], we observed severe experimental versus theoretical profile discrepancies.

The aim of our study was therefore to determine the apparent A- and M-band lengths obtained from SHG data using the supra-molecular model when  $A$  is set as a freely adjustable parameter, instead of fixing it to  $1.6 \mu\text{m}$ . This yielded more accurate fits, but both the apparent A- and M-band lengths were then lower than their corresponding EM values, with M-band lengths approaching zero. To explain the obtained values, we studied the effect of two optical parameters and a biological feature on the SHG intensity profiles of sarcomeres.

The first optical parameter is the refractive index (RI) mismatch between the illumination wavelength ( $n_\omega$ ) and the SHG wavelength ( $n_{2\omega}$ ). Rouède *et al.* [36] assumes that the refractive index of muscle tissue approaches that of water and that the tissue behaves dispersionless:  $n_\omega = n_{2\omega} = 1.33$ . However, even a small RI mismatch already leads to signal phase mismatch in the axial direction [43], affecting the coherent properties of the SHG signal, and thereby altering the far field emission profile on which the supra-molecular model relies. RI data for muscle tissue originating from various species have been reported, mentioning values ranging from 1.37 to 1.41 in the visible wavelength range [101–103]. Yet, only a limited amount of studies exist where a full dispersion analysis from the visible to near infra-red light range is performed [102]. Besides the regular wavelength dependence of the refractive index, other RI affecting optical effects might be involved. The use of ultra short pulsed lasers [6], but also dichroism [103] and differences in RI of the sarcomere A and I region [104] play a role in the complete dispersion properties of skeletal muscle tissue. In this study, we investigated the dispersion effect by analysing an experimental data set with a range of RI mismatches.

The second optical parameter that affects the returned length information is the NA of the illumination objective. To obtain sufficient resolution for an accurate length estimate, immersion objectives with higher numerical apertures are desired. However, tighter focussing with high NA objectives induces additional transverse and axial polarization fields [57, 58], which are not included in the supra-molecular model [36]. We therefore looked at the influence of the illumination NA on the returned lengths.

The studied biological feature is related to the ordering of the myosin rods inside the thick filament. For this, the effect of the density distribution of myosin rods along the thick filament axis was studied. We performed simulations by implementing the myosin packing according to models by Knight *et al.* [105] and Skubiszak and

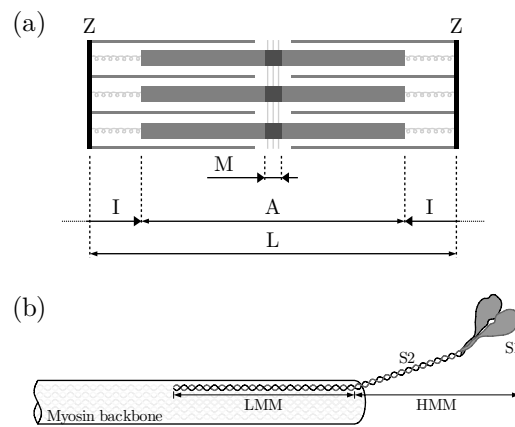


**Figure 5.1:** (a) Illustration of sarcomere structure.  $L$  is the sarcomere length from Z-line to Z-line, A is the thick filament A-band, M is the anti-parallel M-region, I indicates the I-band. (b) Detailed depiction of the right end of a thick filament. It shows how the light meromyosin (LMM) chain contributes to the myosin backbone, whereas sub-fragment 1 (S1) and 2 (S2) of the heavy meromyosin (HMM) are not part of this backbone due to a loose S2/LMM hinge connection.

Kowalczyk [10], considering either the LMM or the LMM and S2 as SHG active regions (Fig. 5.1)[63, 90, 106].

## 5.3 Materials and methods

### 5.3.1 Tissue preparation

#### Skeletal muscle

Female Lewis rats of age 6-7 weeks, and body weight 100 – 120 g (Harlan CPB, Zeist, The Netherlands) were housed in the animal facilities at Hasselt University. The animals used in this work were the health control animals of a study for which the protocol was approved by the animal Ethics Committee of Hasselt University, and was in accordance with the national and European legislation. The National Research Council's guide for the care and use of laboratory animals was followed.

After anaesthetizing with pentobarbital sodium (5 mg/100 g body weight), *Flexor digitorum longus* muscles were dissected from both hind limbs, incubated overnight in 4% para-formaldehyde (PFA) at 4°C, followed by cryoprotection in 30% sucrose in phosphate buffered saline (PBS) at 4°C until the tissue had sunk. Muscles were frozen in optimal cutting temperature compound (Tissue-Tek, Sakura Finetek Europe, The Netherlands) using liquid nitrogen cooled isopentane and stored at –80°C. 14 µm thick sections proved to be the best reproducible thinnest sections on the available cryostat (CL 1990 UV, Leica, Wetzlar, Germany). The sections were made along the length of the myofibers, mounted onto Superfrost Plus glasses (Menzel-Gläser, Thermo Fisher Scientific, Waltham, MA) and stored at –20°C. Before imaging, sections were washed 3 times 5 minutes in PBS, dipped into milli-Q water and a cover slip was placed using Immu-Mount™ (Thermo Fisher Scientific, Waltham, MA). Coverslipped sections were stored at 4°C until imaging.

### 5.3.2 Microscopy

SHG imaging was performed using a Zeiss LSM510 META (Carl Zeiss, Jena, Germany) mounted on an Axiovert 200M and a 40x/1.3 oil immersion objective (Plan-Neofluar 40x/1.3 Oil DIC, Carl Zeiss). A back aperture pinhole was used to reduce the effective NA to approximately 0.8 in order to be able to test the effect of a higher NA on the recovered model parameters [58]. The excitation was provided by a femtosecond pulsed laser (MaiTai DeepSee, Spectra-Physics, CA) tuned at a central wavelength of  $\lambda_{\omega} = 810$  nm. The SHG signal was collected in forward mode by a condenser with a  $NA_C$  of 0.8. After passing through a 400 – 410 nm bandpass filter, the forward directed signal was detected by an analogue photomultiplier tube, delivered by Zeiss.

### 5.3.3 Point spread function

The PSF was measured by two-photon excited fluorescence microscopy of green fluorescent microspheres (PS-Speck™ Microscope Point Source Kit, Molecular Probes,

Eugene, OR) mounted on a microscope cover glass. The 3D PSF information of at least 20 beads was compared to a 3D Gaussian intensity profile for two-photon processes ( $I_{2P}$ ),

$$I_{2P}(x, y, z) \propto |E_\omega(x, y, z)|^4 \propto e^{-\frac{4x^2+4y^2}{w_{xy}^2} - \frac{4z^2}{w_z^2}}, \quad (5.1)$$

yielding  $w_{xy} = 0.576 \mu\text{m}$  and  $w_z = 3.802 \mu\text{m}$  for  $\text{NA} = 0.8$ , and  $w_{xy} = 0.467 \mu\text{m}$  and  $w_z = 1.946 \mu\text{m}$  for  $\text{NA} = 1.3$ .

### 5.3.4 Sarcomere profile analysis

The profile analysis was done by in-house developed Matlab (Version R2013a, The MathWorks, Natick, MA) routines. Sarcomere dimensions were obtained by analysis of manually selected intensity profiles. Each selected profile was required to extend at least three similarly appearing sarcomeres to obtain a good estimate of all length parameters. Four additional parallel profiles separated one pixel, and two pixels at both sides of the selected profile were included and averaged for noise reduction. Cubic interpolation was used by Matlab's built-in function *improfile* to obtain SHG intensities for the coordinates belonging to the selected profile. The weighted and reduced goodness-of-fit ( $\chi^2$ ) for each profile was calculated by taking the experimentally determined noise properties of the imaging set up into account. The intensity dependent noise was quantified by calculating the mean and standard deviation from a series of uniform images.

### 5.3.5 Simulations

Myosin density simulations were performed for an illumination NA of 0.8, using a sarcomere length of  $L = 2.2 \mu\text{m}$ , and a refractive index mismatch of  $\Delta n = 0.02$  with  $n_\omega = 1.39$ , based on the results shown in section 5.4.1. For repeated simulations, random noise obeying the measured noise properties was superimposed onto a noise-free profile.

### 5.3.6 The supra-molecular model

The SHG far field radiation pattern was calculated by [36]

$$I(\theta, \phi) \sim I^X I^Y I^Z (1 - \sin^2 \theta \cos^2 \phi) \quad (5.2)$$

with  $\theta$  and  $\phi$  respectively the polar and azimuthal angle with respect to the centre of the Gaussian illumination beam (Fig. 5.2). The dispersion induced phase mismatch between the illumination wave ( $k_\omega = 2\pi n_\omega \lambda_\omega^{-1}$ ) and the SHG signal ( $k_{2\omega} = 4\pi n_{2\omega} \lambda_\omega^{-1}$ ), has an effect on the  $X$ ,  $Y$  and  $Z$  components which are given by

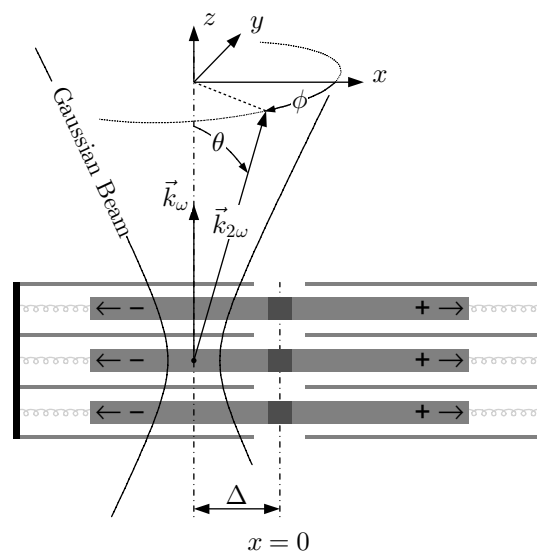


**Figure 5.2:** Parameters in the supra-molecular model and system definition.  $\Delta$  is the scan parameter representing the position of the Gaussian beam with respect to the center of the sarcomere. The + and - sign represent the  $\pi$  phase shift due to the direction inversion at the center of the thick filament as indicated by the arrows. See Fig. 5.1 for the definition of the structural parameters  $A$ ,  $M$  and  $L$ .

[36, 107]

$$I^X = \frac{\pi}{2} w_{xy}^2 \left| \sum_{n=-\infty}^{+\infty} a_{\Delta,n} e^{-\frac{1}{8} k_{2\omega}^2 w_{xy}^2 \left( \sin \theta \cos \phi - \frac{2n\pi}{L k_{2\omega}} \right)^2} \right|^2 \quad (5.3)$$

$$I^Y = \frac{\pi}{2} w_{xy}^2 e^{-\frac{1}{4} k_{2\omega}^2 w_{xy}^2 (\sin \theta \sin \phi)^2} \quad (5.4)$$

$$I^Z = \frac{\pi}{2} w_z^2 e^{-\frac{1}{4} w_z^2 (k_{2\omega} \cos \theta - 2k_\omega + 4k_\omega^{-1} w_{xy}^{-2})^2} \quad (5.5)$$

with

$$a_{\Delta,n} = \frac{-2i}{\pi n} \sin \left[ \pi n \frac{A+M}{2L} \right] \sin \left[ \pi n \frac{A-M}{2L} \right] \exp \left( -\frac{2i\pi n \Delta}{L} \right), \quad (5.6)$$

and where  $A$ ,  $L$  and  $M$  are the sarcomere structural parameters (Fig. 5.1).  $\Delta$  is the parameter representing the position of the Gaussian beam on the sample (Fig. 5.2). The intensity at each position  $\Delta$  was obtained by integrating the emission profile according to the condensor properties,

$$I(\Delta) = \int_0^{2\pi} \int_0^\Theta I(\theta, \phi) \sin \theta \, d\theta \, d\phi \quad (5.7)$$

with  $\Theta = \arcsin(\text{NA}_C)$ . Due to the RI mismatch, the emission profile could change in such a way that relevant intensity parts are not collected by the condenser. Moreover, an increased phase-mismatch results in a lower SHG signal, with a less pronounced intensity decrease at the M-band region due to the hemi-filament phase reversal, resulting in altered sarcomeric intensity profiles.

## 5.4 Results

### 5.4.1 Dispersion

To emphasize the effect of the RI mismatch and a free A-band, simulations were performed and compared to a representative experimental profile (Fig. 5.3a-b). It is clear that zero RI mismatch results in simulated profiles that do not agree with the experimental data, neither for  $A = 1.6 \mu\text{m}$  and  $M = 0.15 \mu\text{m}$  nor for the optimal  $A$  and  $M$  obtained from a fit. Increasing the RI mismatch to  $\Delta n = 0.02$  resulted in theoretical sarcomeric profiles that are closer matching to the experimental data, with the best match obtained for the fitted A- and M-band length. Our data indicate that both the RI mismatch and the freely adjustable filament lengths are crucial to obtain simulated profiles properly matching the experimental data.

To gain insight in the effective dispersion properties of striated muscle, a set of single band sarcomere SHG profiles ( $N = 16$ ) was analysed using an RI mismatch ranging from 0 to 0.04 with a 0.001 step size (Fig. 5.3c-e). Assuming that the supra-molecular model is an accurate model, the optimal  $\Delta n$  can be determined by means of the resulting  $\chi^2$ . In the analysis, the sarcomere length and the M-band size were freely adjustable. Additionally, the effect of taking a freely adjustable A-band parameter was compared to a fixed A-band value. In accordance with Rouède *et al.* [36], this value was chosen  $1.6 \mu\text{m}$ . For the freely adjustable A-band length, the minimal  $\chi^2 = 1.04 \pm 0.45$  was observed for a  $\Delta n = 0.020$ . For this optimal RI mismatch, an apparent A-band length of  $A = 1.40 \pm 0.04 \mu\text{m}$  was obtained and simultaneously an apparent M-band length of  $M = 0.07 \pm 0.05 \mu\text{m}$  resulted (Table 5.1). Fixing the A-band length to  $1.6 \mu\text{m}$  resulted in a notably higher minimal  $\chi^2 = 2.65 \pm 0.78$  at  $\Delta n = 0.013$ , with an apparent M-band length of  $M = 0.04 \pm 0.04 \mu\text{m}$ .

Because no significant effects were observed on the recovered parameters for  $n_\omega$  ranging from 1.37 to 1.41, the value of  $n_\omega$  was always fixed at 1.39. This finding indicates that the RI mismatch imposes the major profile alterations, not the effective RI.

### 5.4.2 Tight focussing

The data shown in Fig. 5.3 were generated using an illumination objective with  $\text{NA} = 0.8$ . One could argue that a higher NA is beneficial for the resolution and thus better to accurately estimate length parameters. However, tight focussing of light polarized in the  $x$ -direction is known to induce polarization components in both the  $y$  and  $z$  direction [57, 58], a feature that is not included in the supra-molecular model [36]. We experimentally tested the effect of increasing the NA to 1.3 by removing the back aperture pinhole and imaging the exact same regions as for the low NA (Fig. 5.4). Both from the raw image data (Fig. 5.4a) and the profile comparison (Fig. 5.4b) it is clear that tight focussing alters the SHG intensity profile, resulting in pronounced

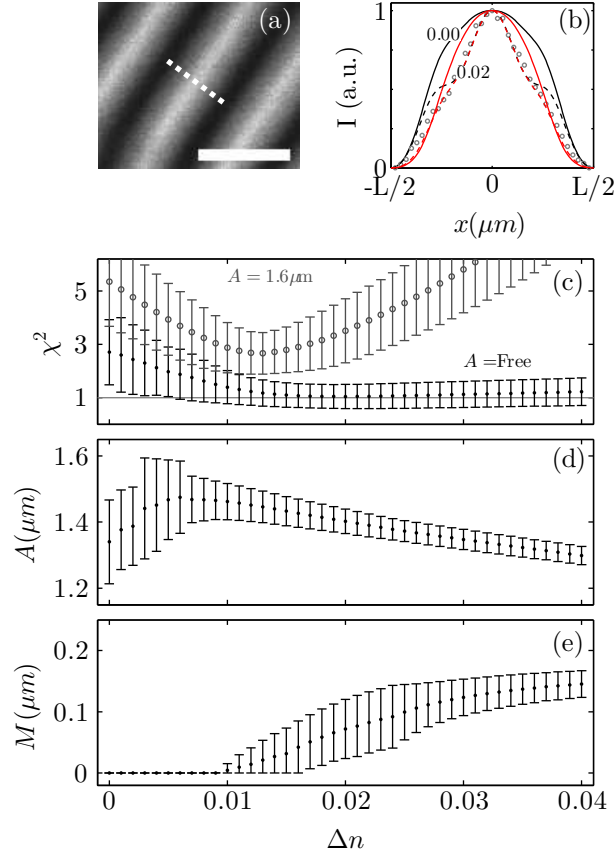


**Figure 5.3:** The effect of dispersion on skeletal sarcomere intensity profiles imaged using  $\text{NA} = 0.8$ . (a) typical SHG image of single band sarcomeric structures. Scale bar  $3 \mu\text{m}$ . The dashed line illustrates a selected profile containing one sarcomere. (b) Typical experimental single band pattern (circles). The numbers indicate the refractive index mismatch  $\Delta n = n_{2\omega} - n_{\omega}$  with  $n_{\omega}$  fixed at 1.39 [102]. Additional simulation parameters:  $A = 1.60 \mu\text{m}$  and an  $M = 0.15 \mu\text{m}$  for black lines. The red lines show the best fit for each RI mismatch with a free  $A$  and  $M$ . The profiles are normalized to their maximum value. (c) Effect of pre-set RI mismatch on the  $\chi^2$  of the fit on a set of single band sarcomere intensity profiles. A freely adjustable A-band (dots) versus an A-band fixed at  $1.6 \mu\text{m}$  [36] (circles) is shown. The error bars represent standard deviation ( $N=16$ ). (d) and (e) respectively show the resulting A- and M-band length as function of RI mismatch for freely adjustable  $A$  and  $M$ .

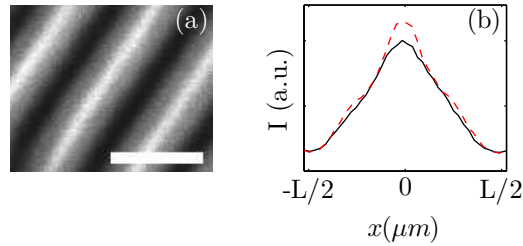


**Figure 5.4:** Effect of tight focussing on the SHG intensity profile. (a) Raw image data obtained using an objective with NA = 1.3 for same region as shown in Fig.5.3a. (b) Profile comparison of raw data for objective with NA = 0.8 (solid) and NA = 1.3 (dashed). Scalebar 3  $\mu\text{m}$ .

shoulder regions near the sides of the M-band.

The sarcomere dimensions were studied in a similar way as for the moderate NA objective. The PSF was acquired separately and included in the analysis. Compared to the low NA data, a different optimal RI mismatch of  $\Delta n = 0.028$  resulted at the minimal  $\chi^2 = 2.08 \pm 1.06$ . At this RI mismatch, a significantly different apparent  $M = 0.03 \pm 0.03 \mu\text{m}$  ( $p < 0.005$ ) and similar apparent  $A = 1.38 \pm 0.04 \mu\text{m}$  were observed.

### 5.4.3 Myosin density distribution

The myosin rod is known to be the basic building block of the myosin thick filament. Using detailed information of these rods, we studied their role in defining the sarcomere SHG intensity profile and the associated lengths estimated by the supra-molecular model. The myosin rod can be subdivided into two main regions: the heavy meromyosin (HMM) and the light meromyosin (LMM) region (Fig. 5.1). The HMM consists of two sub-fragments: sub-fragment 1 (S1) containing the two globular heads, and the 62 nm long sub-fragment 2 region (S2) which is part of the  $\alpha$  helical coiled-coil of the myosin rod [10]. The other part of this  $\alpha$  helix is located at 100.6 nm long LMM region [10]. It is known that the only the LMMs assemble into the backbone of the thick filament, but how this packing is organized is still under debate [10, 99, 105, 108]. A general consensus is that the myosin density decreases at the distal parts of the myosin filament [10, 99]. We tested two possible packing schemes, both based on the the complete bipolar model suggested by Skubiszak and Kowalczyk [10] in which the myosin rod takes a helical form.

For both models a total of 98 positions with S1 units (crowns) are assumed for the entire thick filament [10, 105]. The step between successive myosin rods is 14.33 nm and the anti-parallel overlap in the central zone is maximal  $7 \times 14.33 \text{ nm}$ . Due to the helical rod shape, the LMM and S2 have a projected axial length of 88.44 nm

**Table 5.1:** Comparison of apparent A- and M-band length between experimentally obtained values in this work, and values obtained by simulations taking the effective myosin density into account. The objective NA = 0.8. All lengths are in  $\mu\text{m}$ , and the mean values with standard deviation are given. N = 250 for simulations.

Par.	Experimental (N=16)	Skubiszak and Kowalczyk [10]		Knight [105]	
		LMM	LMM+S2	LMM	LMM+S2
A	$1.40 \pm 0.04$	$1.31 \pm 0.01^*$	$1.35 \pm 0.01^*$	$1.37 \pm 0.01^*$	$1.40 \pm 0.01$
M	$0.07 \pm 0.05$	$0.03 \pm 0.02^*$	$0.11 \pm 0.01^*$	$0.01 \pm 0.01^*$	$0.06 \pm 0.02$

\* denotes  $p < 0.001$  compared to experimental value (one-way ANOVA)

and 53.17 nm respectively. In the Skubiszak and Kowalczyk packing model the three successive proximal and distal crowns of each hemi-filament, thus in total 12 out of 98 crowns, contain only 1 set of globular heads (S1), whereas the remaining crowns contain 3 of those sets. The thick filament is then composed of a total of 270 myosin rods. The second packing model is based on observations done by Knight [105]. Each crown has 3 sets of globular heads and a gap is present before the last two distal crowns. A total of 294 myosin molecules are then contained in the thick filament.

To calculate the SHG profiles from these packing schemes, the SHG active density  $g(x)$  was defined by the sum of polarized rods in the positive and negative  $x$ -direction direction. This means one side of the filament contains a negative density, the other side is positive and at the center of the myosin rod the SHG active density is zero (Fig. 5.5). This is in agreement with the original supra-molecular model [36]. In Fig. 5.5, the myosin density  $g(x)$  along the thick filament axis is plotted for both models, and for the case of LMM or LMM+S2 as the SHG active region. Note that for both packing models, the myosin density turns zero at  $\approx 0.8 \mu\text{m}$  (distal) when LMM+S2 is considered, as indicated by the dots in Fig. 5.5. This explains the  $1.6 \mu\text{m}$  observed by EM.

We included the effective myosin rod packing scheme  $g(x)$  in the supra-molecular model by calculating the Fourier coefficients  $a_{\Delta,n}$  through numerical integration of

$$a_{\Delta,n} = \int_{-L/2}^{+L/2} g(x) \exp\left(-\frac{2i\pi n(x + \Delta)}{L}\right) dx. \quad (5.8)$$

In this adjusted model, the SHG intensity profile is entirely defined by the packing scheme and sarcomere length  $L$ , making the  $A$  and  $M$  parameter of the original model redundant. To be able to compare the simulated profiles based on  $g(x)$  to the experimentally obtained profiles, the simulated profiles were analysed with the original supra-molecular model. This yielded  $A$  and  $M$  values that can be compared to their corresponding experimental values (Table 5.1).

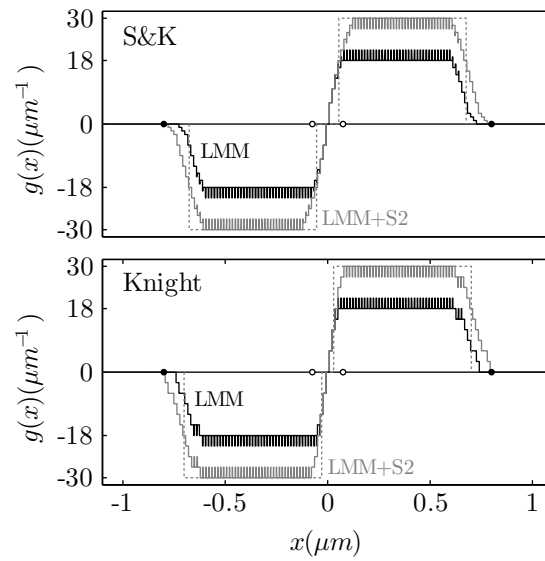


**Figure 5.5:** Plot of SHG active density for each position along the axis of the thick filament  $g(x)$ , according to the model by Skubiszak and Kowalczyk (S&K) or Knight, either with or without taking the S2 part into account. The polarity inversion at the center of the thick filament is included by the sign of the density. The dashed line represents best fitting supra-molecular model for the case of LMM+S2 as SHG active. The dots and circles indicate the A-band and M-band range respectively, according to EM observations [99].

## 5.5 Discussion

The presented work was initiated by the discrepancy between the experimentally obtained apparent A- and M-band length, and the lengths assumed in the supra-molecular model for sarcomere SHG intensity profiles. Both the apparent A- and M-band length consistently resulted in values lower than the assumed values. We conclude that, when applying the supra-molecular model to single band intensity profiles, the experimentally obtained lengths for the A- and M-band are  $A = 1.40 \pm 0.04 \mu\text{m}$  and  $M = 0.07 \pm 0.05 \mu\text{m}$ , instead of  $A = 1.6 \mu\text{m}$  and  $M = 0.15 \mu\text{m}$  respectively. Note that for comparing these values, we assumed no variation of filament lengths across different vertebrate species [109]. To explore the observed length differences, the effect of optical parameters being the RI mismatch and objective numerical aperture were evaluated. Additionally, the biologically relevant myosin density distribution was explored.

Based on the goodness-of-fit of the supra-molecular model to the experimental data (Fig. 5.3c), and visual inspection of the fitted profiles (Fig. 5.3b), our data clearly demonstrate that leaving the A-band freely adjustable resulted in better fits. Although it might be obvious that increasing the degrees of freedom results in better fits, it caused the resulting apparent A-band length to vary around  $1.4 \mu\text{m}$ , severely deviating from the assumed  $1.6 \mu\text{m}$ . This indicates that SHG based data cannot be compared directly to the lengths estimated by other techniques such as EM.

For the full studied RI mismatch range, and in case of a freely adjustable  $A$ , the analysis revealed lower than expected apparent A- and M-band lengths (Table 5.1). Regarding the apparent A-band length, the data in Fig. 5.3c show that the expected  $1.6 \mu\text{m}$  is never returned by the fit in the studied RI mismatch range. The apparent M-band length for  $\Delta n$  below 0.01 always returned 0, again not agreeing with the initial assumptions of the supra-molecular model. The optimal RI mismatch was estimated to be  $\Delta n = 0.02$  with  $n_\omega = 1.39$  (Fig. 5.3). This  $\Delta n$  is lower than previously reported values of  $\approx 0.03$ , obtained by measurements on fresh tissue [102]. Our sample was fixed with 4% PFA and cryo-protected with 30% sucrose, suggesting that the obtained RI mismatch value is protocol specific and probably limited to the presented experiments. We opted to select the  $\Delta n$  for which the average  $\chi^2$  is at its absolute minimal value. Note however that for a free  $A$ , the  $\chi^2$  was acceptably low in a broad range around this minimum. In fact, a t-test with 5% confidence levels revealed that for any RI mismatch above 0.011, the average  $\chi^2$  was not significantly different than 1 in the tested range. This might be related to the low resolution of the used objective (NA = 0.8). For this lower resolution good fits can be obtained for any higher RI mismatch, but with unexpected values for both  $A$  and  $M$ . Despite the uncertainty of the method, we chose to continue our work with the RI mismatch for which the average  $\chi^2$  is at its absolute minimal value. This choice was further rationalised by the following observation. For increasing  $\Delta n$ ,  $M$  tends toward a value that agrees with that obtained by EM, indicating a higher

$\Delta n$  is more suited. However, at higher  $\Delta n$   $A$  decreased and deviates even more from the EM value, suggesting a lower  $\Delta n$  is more appropriate. To conclude, we were not able to generally define the effective RI mismatch of fixed muscle tissue with this approach, though we emphasize the importance of taking sample dispersion properties into account when applying the supra-molecular model (Fig. 5.3).

In an attempt to explain the A-band length discrepancy, two previously described models for the myosin rod arrangement within the thick filament were implemented in the supra-molecular model. Using this, the influence of the effective myosin density on the parameter recovery by the supra-molecular model was tested. For each packing model, both the case of only LMM and LMM+S2 as SHG active regions were considered (Table 5.1, NA = 0.8). First of all, independent of the used model or of which region should be considered as SHG active, the apparent A- and M-band lengths appeared always shorter than their corresponding EM values of 1.6  $\mu\text{m}$  and 0.15  $\mu\text{m}$  respectively. This is in agreement with our experimental results, indicating that the density distribution of the myosin rods is crucial in defining the SHG intensity profile. Regarding both the apparent A- and M-band lengths, only the simulated profiles based on the packing model by Knight *et al.* [105], with LMM+S2 as SHG active regions resulted in similar lengths as found the experimental data. This suggests that the S2 region should be taken into account as significant contributor, a fact that is currently still under debate. Plotnikov *et al.* [63] suggests that only the LMM inside the thick filament backbone is the major contributor. Based on polarization SHG (P-SHG) Psilodimitrakopoulos *et al.* [13] shows that the helical pitch angle of the SHG source resembles that of the myosin  $\alpha$ -helix of which both the LMM and the S2 region are composed of. Almost simultaneously, but also independent from each other, Nucciotti *et al.* [90] and Schürmann *et al.* [106] show that the P-SHG profile depends on the contraction state of the sarcomeres. They suggest and simulate that the reorientation of the S2 part due to binding of the myosin heads (S1) to actin is causing a change in P-SHG response, thereby proving that S2 significantly contributes to the SHG signal. To test the effect of the S2 presence on the apparent A-band and M-band length, it would be better to effectively remove this region by long term trypsinization or specific cleaving [110]. Alternatively, experiments based on the rigor state of muscle tissue, similar to those by Nuciotti *et al.* [90] and Schürmann *et al.* [106], can be performed to study the effect of S2 re-orientation on the retrieved lengths.

The effect of the objective NA on the profiles was experimentally tested by imaging regions with both NA = 0.8 and NA = 1.3 (sec. 5.4.2). For both NAs, a different optimal RI mismatch and M-band size was observed, while a similar A-band length was returned. The observed differences are possibly due to additional polarization fields caused by the high NA [57, 58]. These fields are not taken into account by the supra-molecular model [36], yielding different results for the same sarcomeres. Since the high NA describes the experimental data less accurately, as indicated by the higher  $\chi^2$ , and because tight focussing is known to alter polarization states, we

suggest that a moderate NA is beneficial when using the supra-molecular model. However, using this moderate NA comes at the cost of a lower resolution, making accurate estimates of the filament lengths prone to errors. Alternatively, if one desires to use a higher NA, the supra-molecular model should be adjusted to include the different field components introduced by the tight focussing. This requires redefining the implementation of the second order susceptibility and Gaussian illumination beam, similar to what Schürmann *et al.* did [106]. This would make the model complicated and requires finite element methods to calculate the intensity profiles. These methods additionally allow to include other optical artefacts such as ellipticity of the illumination beam or local changes in the refractive index [104], probably resulting in more accurate models. Conversely, finite element methods are based on heavier calculations making high throughput analyses extremely slow.

By an apparent increase in the apparent M-band size, the supra-molecular model is able to distinguish regular sarcomeres from proteolytic ones [36]. This means the M-band length is more important than the A-band length as a marker for decreased muscle quality. To overcome possible covariance between  $M$  and  $A$  as fit parameter, it is advisable to fix the A-band length to the previously obtained value of  $\approx 1.4 \mu\text{m}$  (Table 5.1). Additionally, due to the lower resolution caused by a moderate NA, the apparent M-band length often reduces to a meaningless value of  $0 \mu\text{m}$ . A lower limit for the apparent M-band size should then be set to the observed  $\approx 0.07 \mu\text{m}$  (Table 5.1).

Alternative to the apparent increase of the M-band length, a thick filament disorder, which is suggested by Rouède *et al.* [36] to be the source of the increasing M-band size, can be included into the supra-molecular model directly. This would be more in line with the observations of Gotthardt *et al.* [111]. They show data of skeletal muscle fibres with sarcomere disarray due to titin kinase domain absence which is indicative for muscle degeneration. The disarray is evidenced by a dimmed M-line in electron micrographs, while the data simultaneously show a random shifting of the individual thick filaments. By implementing the thick filament disorder directly, simultaneously occurring effects on the A- and M-band length are taken into account (Fig. 5.6). The disorder can be implemented by replacing  $\Delta$  in eq. (5.6) by  $\Delta + \delta$ , where  $\delta$  represents the filament shift with respect to the central position (Fig. 5.6). The number of myosin thick filaments within the focal volume, and thus contributing to the total SHG signal, is sufficiently large ( $10^3 - 10^4$ ) to represent the filament shifts as a continuous density distribution function  $\Phi(\delta)$ . The Fourier coefficients (eq. (5.6)) are then to be replaced by

$$a'_{\Delta,n} = a_{\Delta,n} \int \exp\left(-\frac{2i\pi n\delta}{L}\right) \Phi(\delta) d\delta \quad (5.9)$$

For a set of thick filaments shifted according to a Gaussian distribution with standard deviation  $\sigma$ , the Fourier coefficients  $a_{\Delta,n}$  are modulated by  $\exp(-2\sigma^2\pi^2n^2/L^2)$ . Using this model, the apparent effect of thick filament disorder on the A- and M-

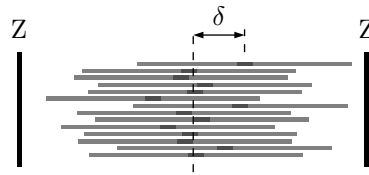


**Figure 5.6:** Depiction of the myosin disorder model with a Gaussian distribution. Each horizontal line represents a thick filament containing the centrosymmetric M-band, indicated by the dark region. The thick filaments are shifted with respect to the sarcomere centre (dashed line) by a distance  $\delta$  which is assumed to be Gaussian distributed.

band size is quantified by only one parameter  $\sigma$ . However, it relies on using a correct value for  $A$  and  $M$ , which can be obtained by the initial supra-molecular model using a set of single band SHG intensity profiles for which  $\sigma = 0$ . To conclude, the disorder method does not reject the assumption of a fixed thick filament length [112], and omits the need of considering apparent changes in the filament lengths.

## 5.6 Conclusions

We showed that the dispersion properties of muscle tissue are crucial for the SHG intensity profiles of sarcomeres. Also, when applying the supra-molecular model as developed by Rouède *et al.* [36], it is advisable to use moderate NA objectives for which no significant additional polarization states arise. Under these conditions, the apparent A-band length of  $1.40 \pm 0.04 \mu\text{m}$  and apparent M-band length of  $0.07 \pm 0.05 \mu\text{m}$  proved to be most appropriate to model single band intensity profiles. As these lengths differ from those observed by EM, the values for both the A- and M-band determined by EM and SHG microscopy cannot directly be compared to each other. We believe that the results obtained in this work provide insights that are crucial for the application of the supra-molecular model to study SHG intensity profiles in striated muscle, and eventually to study pathology induced sarcomere alterations.

## **Acknowledgements**

This research is part of the Interreg EMR IV-A project BioMiMedics ([www.biomimedics.org](http://www.biomimedics.org)) and is co-financed by the European Union, local governments, research institutes and SMEs. Support by the BELSPO funded IAP-PAI network P7/05 on Functional Supramolecular Systems (FS2) is acknowledged. The Province of Limburg (Belgium) is acknowledged for the financial support within the tUL IMPULS FASE II program, allowing for the upgrading of the laser source used in this work.

## **CHAPTER 6**

---

# **Fully automated muscle quality assessment by Gabor filtering of SHG images**

---

**Paesen, R.**, Smolders, S., de Hoyos Vega, J. M., Eijnde, B. O., Hansen, D. & Ameloot, M. Fully automated muscle quality assessment by Gabor filtering of SHG images. *J. Biomed. Opt.* **21**, 026003–1 –026003–9 (2016)

## 6.1 abstract

Although structural changes on the sarcomere level of skeletal muscle are known to occur due to various pathologies, rigorous studies of the reduced sarcomere quality remain scarce. This can possibly be explained by the lack of an objective tool for analyzing and comparing sarcomere images across biological conditions. Recent developments in second harmonic generation (SHG) microscopy and increasing insight into the interpretation of sarcomere SHG intensity profiles have made SHG microscopy a valuable tool to study micro-structural properties of sarcomeres. Typically, sarcomere integrity is analyzed by fitting a set of manually selected, one dimensional SHG intensity profiles with a supra-molecular SHG model. To circumvent this tedious manual selection step, we developed a fully automated image analysis procedure to map the sarcomere disorder for the entire image at once. The algorithm relies on a single frequency wavelet based Gabor approach, and includes a newly developed normalization procedure allowing for unambiguous data interpretation. The method was validated by showing the correlation between the sarcomere disorder, quantified by the M-band size obtained from manually selected profiles, and the normalized Gabor value ranging from 0 to 1 for decreasing disorder. Finally, to elucidate the applicability of our newly developed protocol, the Gabor analysis was used to study the effect of experimental autoimmune encephalomyelitis on the sarcomere regularity. We believe that the technique developed in this work holds great promise for high throughput, unbiased and automated image analysis to study sarcomere integrity by second harmonic generation microscopy.

## 6.2 Introduction

Various types of muscle diseases with changes on the sarcomere level have been identified [92], including types of distal muscular dystrophy which are often caused by defects in structural components of sarcomeres [113]. However, myopathy related research is seldom based on the study of sarcomeres. Instead, myofibre cross-sections are considered to detect irregularities or odd features such as nemalin rods [114], and to study changes in cross sectional area due to myogenesis or muscle atrophy [115, 116]. For these studies, standard tools such as immunohistochemistry (IHC) are used to stain and visualize specific proteins within the tissue. In case sarcomeres are considered, structural details of the sarcomere organization is obtained by transmission electron microscopy (TEM). Both IHC and TEM rely on tedious sample preparation. IHC requires many staining optimization steps, while TEM might suffer from possibly biased human selection of representative regions [117]. Therefore, these standard techniques do not allow to study sarcomere irregularities in a high throughput fashion. The development of a fast and reliable screening tool of sarcomere morphology would be very helpful.

Label-free second harmonic generation (SHG) microscopy provides an attractive pathway that can meet these conditions. Because of the extreme high degree of ordering of the myosin thick filaments, strong SHG signals arise from skeletal muscle tissue [12, 36, 63, 90, 91], making SHG a perfect tool for imaging sarcomeric structures. Muscle degradation is known to be related to disruption of M-proteins which interconnect thick filaments to attain sarcomere integrity [118, 119]. The thick filament misalignment due to absence of M-proteins is known to lie at the basis of clear transition from normal single band to double band SHG intensity profiles [36, 157]. Based on a supra-molecular sarcomere model to calculate the expected SHG intensity profiles, the degree of thick filament misalignment can be quantified by means of an apparent increase in the centrosymmetric M-band size [36, 157]. Currently, this degree of sarcomere disorder is mostly obtained by analyzing local, manually selected one-dimensional sarcomere intensity profiles. On the other hand, based on the distance dependent correlation value of the gray level co-occurrence matrix, Liu *et al.* [93] suggested a method for assessing sarcomere regularity of an entire SHG image. Their approach yields a reliable quantitative measure for sarcomere quality, but produces only a single value to describe the complete manually selected area containing multiple sarcomeres.

For assessing the muscle quality by analysis of full SHG images of muscle tissue while preserving local information, we designed a specific algorithm based on the Gabor analysis[40]. In general, the Gabor analysis relies on wavelets to obtain local frequency content and orientation information [40, 120]. This approach is referred to as Gabor decomposition, and has been applied in a broad range of applications in the field of computer vision technology [121, 122]. In the work by Recher *et al.* [91] a bi-frequency Gabor based approach was already introduced to locate single and

double band SHG patterns of manually selected one-dimensional sarcomere intensity profiles. Here we propose to use an alternative Gabor approach in which regular, single band sarcomeres are located by analyzing full images for the frequency related to the average sarcomere length. Sarcomere irregularities such as double band SHG patterns, but also so-called pitchforks [91, 95] or any other type of anomaly will predominantly be described by higher frequency components and hence become automatically detected as the remainder of this single frequency detection. This makes a full Gabor decomposition redundant and substantially speeds up the analysis. In the current study we introduce a fully automated and fast muscle quality assessment tool based on this single frequency Gabor analysis, yielding a per pixel so-called Gabor value to quantify the sarcomere integrity. The analysis includes a new normalization procedure, allowing for easy sarcomere comparison across various imaging platforms and biological conditions. Moreover, the procedure is designed in such a way that image processing such as cropping to representative regions, image rotation and noise reduction is unnecessary.

The newly introduced Gabor analysis is used to study muscle deterioration due to experimental autoimmune encephalomyelitis (EAE), an animal model of multiple sclerosis (MS) [123]. Central nervous system deficit as a consequence of MS is known to result in decreased central motor function, leading to muscle weakness [124, 125], and ultimately decreasing muscle activity. Muscle disuse is known to induce atrophy [126], for which changes on the sarcomere level can occur [127]. To study the relation between EAE severity and sarcomere regularity, muscle tissue from EAE induced rats and healthy rats is compared. First, the data are used to indicate how the Gabor values should be interpreted based on representative SHG intensity profiles. Next, the relation between the disorder related M-band size [36, 157] and the normalized Gabor value is studied to justify the use of the Gabor approach for assessing sarcomere regularity. Finally, we study the correlation between the EAE severity and the sarcomere regularity quantified by our normalized Gabor value.

## 6.3 Materials and methods

### 6.3.1 EAE Rat model

*Flexor digitorum longus* (FDL) muscle samples were isolated from 8 to 10 weeks old residual female Dark Agouti rats. Rats were purchased from Harlan Netherlands B.V. (Horst, The Netherlands). Experiments were conducted in accordance with institutional guidelines and approved by the Ethical Committee for Animal Experiments of Hasselt University.

EAE was induced by a subcutaneous injection at the base of the tail with a 200  $\mu$ l solution composed of 140  $\mu$ g of recombinant human myelin oligodendrocyte glycoprotein (MOG) in complete Freund's adjuvant (F5506, Sigma-Aldrich, St. Louis, MO) supplemented with 2.5  $mg/ml$  H37RA heat-inactivated mycobacterium tuberculosis (Difco, BD Diagnostics, MD). Healthy control animals did not receive any injection. Immunized rats were weighed and received a pain score (*PS*) on a daily basis according to the following neurological scale: 0.5 = partial loss of tail tonus, 1 = complete loss of tail tonus, 2 = hind limb paresis, 3 = hind limb paralysis, 4 = moribund, 5 = death [128]. EAE rats were sacrificed 30 days after immunization.

### 6.3.2 Tissue preparation

All animals were sacrificed by heart perfusion with Ringer solution after Nembutal injection (100  $mg/kg$ ). FDL muscles were immediately removed from both hind limbs, incubated overnight in 4% para-formaldehyde at 4°C, followed by cryoprotection in 30% sucrose in phosphate buffered saline (PBS) at 4°C until the tissue had sunk. Muscles were frozen in optimal cutting temperature compound (Tissue-Tek, Sakura Finetek Europe, The Netherlands) using liquid nitrogen cooled isopentane and stored at  $-80^{\circ}C$ . 14  $\mu$ m thick sections were cut on a cryostat (CL 1990 UV, Leica, Wetzlar, Germany) along the length of the myocytes, mounted onto Superfrost Plus glasses (Menzel-Gläser, Thermo Fisher Scientific, Waltham, MA) and stored at  $-20^{\circ}C$ . Before imaging, sections were washed 3 times 5 minutes in PBS, dipped into milli-Q and a coverslip was placed using Immu-Mount™ (Thermo Fisher Scientific, Waltham, MA). Coverslipped sections were stored at 4°C until imaging.

### 6.3.3 Microscopy

SHG imaging was performed using a Zeiss LSM510 META (Carl Zeiss, Jena, Germany) mounted on an Axiovert 200M and a 20x/0.75 air objective (Plan-Apochromat 20x/0.75, Carl Zeiss). The excitation was provided by a femtosecond pulsed laser (MaiTai DeepSee, Spectra-Physics, CA) tuned at a central wavelength of 810  $nm$ . The SHG signal was collected in forward mode by a condenser with a numerical aperture (NA) of 0.55. After passing through a 400 – 410  $nm$  bandpass filter, the signal was detected by an analogue photomultiplier tube, delivered by Zeiss.

### 6.3.4 Sarcomere profile analysis

Sarcomere analysis based on manually selected profiles was done as previously described[157]. In short, 2728 intensity profiles were manually selected from 68 SHG images, taken from both healthy ( $n = 5$ ) and EAE ( $n = 8$ ) animals. Each profile was analyzed using the supra-molecular model developed by Rouède *et al.* [36], yielding the sarcomere length  $L$ , and the disorder related M-band size  $M$ . Based on our previous observations, the analysis was done using an A-band length of  $A = 1.40 \mu m$ , a refractive index (RI) at the illumination wavelength  $n_\omega = 1.39$  and an RI at the SHG wavelength  $n_{2\omega} = 1.41$ [157]. For the selected objective, the Gaussian point spread function has a lateral size of  $w_{xy} = 0.59 \mu m$  and an axial size of  $w_z = 3.45 \mu m$  (half width at  $e^{-2}$ )[157].

### 6.3.5 Gabor analysis

In general, a Gabor analysis is used to obtain local frequency components in a signal, either in time or in space. In this work, we consider the SHG images of striated muscle as a spatial signal. The main spatial frequency  $f$  present in these SHG images of regular sarcomeres is related to the sarcomere length  $L$ , such that  $f = L^{-1}$ . The purpose of the algorithm is to locate and quantify sarcomere anomalies at the pixel level. Since SHG images of sarcomere anomalies are typically characterized by spatial frequency components  $f'$  other than  $f$ , our algorithm was designed to obtain a local quantifier indicating the relative contribution of  $f$  to the signal, which we refer to as the local Gabor value. Regions consisting of regular sarcomeres will then receive the highest possible Gabor value.

Instead of a relative contribution, a standard Gabor analysis returns the absolute contribution of the considered frequency. Hence regions containing similarly appearing sarcomeres will have undesired differing Gabor values if the signal intensity differs. These intensity variations are likely to occur across samples, but also within a sample due to variations in a real sample's thickness or changes in opacity of features above and below the focal plane. To obtain a relative quantifier, we implemented a new normalization procedure which yields a normalized Gabor value. In the following sections the theoretical basis of the normalized Gabor analysis is given, and a work flow for a fully automated Gabor analysis of SHG images is discussed.

#### Gabor based protocol

In order explain the design of the Gabor based protocol, we start by describing a real SHG image of striated muscle tissue using a phenomenological model. This model is based on the assumption that a sample of striated muscle contains only sarcomeres of length  $L$ , oriented along the  $x$ -direction, such that the base frequency equals  $f = L^{-1}$ . Due to the aforementioned intensity variations, the SHG image  $I(x, y)$  was modeled with spatially varying amplitude  $A(x, y) \geq 0$  and offset  $O(x, y) \geq 0$ , such

that

$$I(x, y) = O(x, y) + A(x, y) [1 + \cos(2\pi f'(x, y)x)]. \quad (6.1)$$

with  $f'(x, y)$  the main local frequency component. For simplicity, the sarcomere SHG intensity was modeled by an harmonic function instead of using the comprehensive model developed by Rouède *et al.* [36]. According to their model, a regular sarcomere profile consists for 98% out of the base frequency  $f$  for the used imaging parameters. This makes eq. (6.1) a good approximation of regular SHG profiles for which  $f'(x, y) = f$ . Anomalies are then dominated by the local frequency  $f'(x, y) \neq f$ , up to  $f'(x, y) \approx 2f$  for double band patterns.

A practical implementation of the Gabor transform is based on the two dimensional convolution of an image with a Gabor kernel. To obtain the local contribution of the frequency  $f$ , the Gabor kernel is defined as[129]

$$G^f(x, y) = \frac{1}{2\pi\sigma_x\sigma_y} \exp\left(-\frac{x^2}{2\sigma_x^2} - \frac{y^2}{2\sigma_y^2} + 2\pi ifx\right), \quad (6.2)$$

with  $\sigma_x$  and  $\sigma_y$  the width of the kernel in the  $x$ - and  $y$ -direction respectively. Due to the position-frequency uncertainty [40], the width along the sarcomere direction is a crucial parameter for the sensitivity of the analysis. For  $\sigma_x \gg f^{-1}$  a high frequency accuracy is obtained with a low positional accuracy, while the opposite holds for  $\sigma_x \ll f^{-1}$ . A good trade-off for frequency matching and localization is valid when  $\sigma_x \approx f^{-1}$ , for which the kernel spans about 3 sarcomere units (see side panels of step 3 in Fig. 6.1). The choice of  $\sigma_y$  is not related to the length of the sarcomeres. The value of  $\sigma_y$  defines the smallest lateral length scale on which changes are detectable. This length is already limited by the point spread function (PSF) of the imaging device. This PSF size can be estimated using the Rayleigh criterion[130]. Yet, using the PSF size to set  $\sigma_y$  requires additional input parameters to the Gabor analysis. Alternatively, we can assume that lateral changes typically occur on a length scale of one sarcomere, such that  $\sigma_y \approx \sigma_x/3$ . For most imaging systems this value is higher than the PSF size, but it will prove to be sufficiently small to detect sarcomere irregularities. The Gabor kernel can then be rewritten as

$$G^f(x, y) = \frac{3f^2}{2\pi} \exp\left(-\frac{f^2x^2}{2} - \frac{9f^2y^2}{2} + 2\pi ifx\right). \quad (6.3)$$

In our study, the Gabor analysis was applied by first convolving the full image with the Gabor kernel of the frequency  $f$  related to the average sarcomere length, and then taking the modulus ( $|\dots|$ ) of this convolution product (\*),

$$G(x, y) = \left|G^f(x, y) * I(x, y)\right|. \quad (6.4)$$

The resulting value  $G(x, y)$  is defined as the local Gabor value. If  $A(x, y)$ ,  $O(x, y)$  and  $f'(x, y)$  are slowly varying with respect to  $f^{-1}$ , then evaluating eq. (6.4) results

in

$$G(x, y) \approx \frac{A(x, y)}{2} \left| \exp(2\pi i f'(x, y)x) \exp \left[ -\frac{(f'(x, y) - f)^2}{2(f/2\pi)^2} \right] + 2 \exp(-2\pi^2) \right. \\ \left. + \frac{2O(x, y)}{A(x, y)} \exp(-2\pi^2) + \exp(-2\pi i f'(x, y)x) \exp \left[ -\frac{(f'(x, y) + f)^2}{2(f/2\pi)^2} \right] \right|. \quad (6.5)$$

The three last terms are negligible small compared to the first term for non-zero oscillation amplitude  $A(x, y)$ , such that

$$G(x, y) \approx \frac{A(x, y)}{2} \exp \left[ -\frac{(f'(x, y) - f)^2}{2(f/2\pi)^2} \right]. \quad (6.6)$$

The local Gabor value thus comprises both the amplitude  $A(x, y)$  and the frequency mismatch  $f'(x, y) - f$  of the sarcomere related intensity oscillation. We introduce a normalization procedure to compensate for the amplitude variation due to instrumental or sample related artefacts, such that only the local frequency contribution is represented by the Gabor value. The normalized Gabor value  $\bar{G}(x, y)$  is defined as

$$\bar{G}(x, y) = 2 \frac{|G^f(x, y) * I(x, y)|}{A(x, y)}. \quad (6.7)$$

This normalized Gabor value ranges from 0 for complete frequency mismatch, to 1 for perfect frequency matching relative to  $f$ , independent of the oscillation amplitude and offset. The local amplitude and offset are obtained from the image by solving the system

$$S(x, y) \equiv I(x, y) * |G^f(x, y)| = O(x, y) + A(x, y) \quad (6.8)$$

$$\Sigma(x, y) \equiv I(x, y)^2 * |G^f(x, y)| = [O(x, y) + A(x, y)]^2 + \frac{A(x, y)^2}{2}. \quad (6.9)$$

Basically, the operations shown in eq. (6.8) and eq. (6.9) represent a Gaussian smoothing, which is only done sufficiently for  $f \lesssim f'$  such that multiple sarcomeres are covered by the smoothing kernel. The resulting local amplitude and offset are given by

$$A(x, y) = \sqrt{2 [\Sigma(x, y) - S(x, y)^2]} \quad (6.10)$$

$$O(x, y) = S(x, y) - A(x, y) \quad (6.11)$$

### Automated analysis work flow

A detailed flowchart of the analysis is shown in Fig. 6.1. The procedure is developed to attain minimal human input throughout the entire analysis. After acquiring

the SHG image (step 1), the mean sarcomere orientation  $\langle\theta\rangle$  with respect to the horizontal edge of the image, and frequency related to the main sarcomere length are estimated. Both frequency and orientation are contained in the first non-central peak of the 2D frequency spectrum obtained by fast Fourier transform (FFT) of the full image (step 2). First, the frequency coordinate of this spectral peak is detected in a range defined by the typical physiological sarcomere working range, being  $1.6\ \mu\text{m}$  to  $3\ \mu\text{m}$  [131]. At this frequency  $f$ , the angular peak position is determined and taken as the main sarcomere orientation  $\langle\theta\rangle$ . Both  $f$  and  $\langle\theta\rangle$  are initial estimates that will be refined later in the procedure. Based on these initial values for frequency and orientation, the initial Gabor kernel is calculated using eq. (6.3) including a rotational basis transformation. The real (Re) and imaginary (Im) part of a typical kernel are shown in step 3 of Fig. 6.1 for illustrative purposes. The resulting Gabor kernel is applied to the image by a convolution, and additionally the normalization procedure is performed as described in the previous section.

For easy data interpretation, all normalized Gabor values belonging to myocytes are condensed into a histogram (step 4). Values of pixels not belonging to sarcomeres, such as areas in between myocytes, are excluded from the histogram by applying a mask. This mask is obtained by considering  $O(x, y)$  in the background regions. For the approach by eq. (6.8)-(6.11), applied to these background regions,  $O(x, y)$  equals the dark background level and  $A(x, y)$  represent the noise amplitude. Therefore,  $O(x, y)$  is always smaller than the average imaging dark noise  $O(x, y) + A(x, y)$ . The average dark noise level is estimated for each image  $\mathcal{I}$  by iteratively determining the value  $i$  for which

$$\text{med}(\mathcal{I}_{\mathcal{I}\leq i-1}) \leq \text{med}(\mathcal{I}_{\mathcal{I}\leq i}), \quad (6.12)$$

where  $\text{med}(\mathcal{I}_{\mathcal{I}\leq i})$  represents the median of pixel values of  $\mathcal{I}$  having intensity lower than or equal to  $i$ . Considering the image intensity histogram, background regions induce a local maximum at low intensity values, which is located by this algorithm. For regions containing sarcomeres,  $O(x, y)$  will be greater than the average dark noise level. Therefore, only pixels obeying  $O(x, y) > i$  are used to create the Gabor histogram.

Using the histogram resulting from step 4, a frequency optimization routine is performed before continuing to step 5. This optimization is needed to cope with possible variations of sarcomere lengths due to different contraction states at the time of sample preparation. A first estimate of the sarcomere length was obtained by the FFT method in step 2. For each image, the optimal frequency ( $f_o$ ), related to the average sarcomere length  $\langle L \rangle$  present in the image, is obtained by maximizing the 90<sup>th</sup> percentile normalized Gabor value. By considering a percentile, multiple Gabor values are simultaneously taken into account for frequency optimization, which is not the case when only the maximal Gabor value would be maximized. The optimization is done by repeating step 3 and 4 with 6 different frequencies near the initial frequency:  $f \pm 7\%$ ,  $f \pm 14\%$  and  $f \pm 20\%$ . In this it is assumed that error on the initial estimate

of  $f$  by the FFT method is maximum 20%, falling within the earlier mentioned physiological sarcomere working range. The resulting 7 values are sufficient to perform a second order polynomial regression, for which the frequency at the polynomial peak is set as the optimal frequency  $f_o$  for the considered image. Due to the restriction to the physiological working range of sarcomeres lengths,  $f_o$  will always represent the main sarcomere length, even when only double band patterns are present in the image.

In step 5, the actual Gabor analysis is performed with the previously obtained average orientation  $\langle\theta\rangle$  and optimal frequency  $f_o$ . However, to allow for local changes in orientation, the Gabor kernel is applied for angles ranging from  $\langle\theta\rangle - 30^\circ$  to  $\langle\theta\rangle + 30^\circ$  with a step size of  $5^\circ$ . When the kernel orientation matches that of the sarcomere, the Gabor value is maximal. This maximum value is selected for each pixel. This procedure is referred to as maximum projection in Fig. 6.1. Finally, the resulting Gabor data are condensed into the final Gabor histogram (step 6).

### Computing system

The Gabor analysis was performed on a standard 64-bit pc with a 3.6GHz quad core processor, extended with an Nvidia GeForce GTX 680 graphical processing unit (GPU). The analysis code was written in MATLAB (Version R2013a, The Mathworks, Natick, MA) of which the parallel processing toolbox was used for its built-in GPU capabilities.

### 6.3.6 Simulations

Theoretical SHG intensity profiles were simulated using the supra-molecular model developed as described before[157]. The one-dimensional profiles were calculated along the  $x$ -direction by the supra-molecular model and copied laterally ( $y$ -direction) to obtain two dimensional images. Gaussian noise resembling that of the used imaging modality was superimposed onto the theoretical profiles. The point spread function, refractive indexes and A-band length were fixed to the previously mentioned values. The sarcomere length was fixed to  $L = 2.2 \mu m$ .

### 6.3.7 Statistics

Data comparison over different conditions was done using the one way analysis of variance (one-way ANOVA) algorithm of MATLAB's statistical toolbox. Differences were considered significant for  $p < 0.001$ . Data correlation was tested by MATLAB's *corrcoef* function, which besides correlation returns the probability  $p$  of incidental correlation. Correlation was taken to be significant for  $p < 0.05$ .

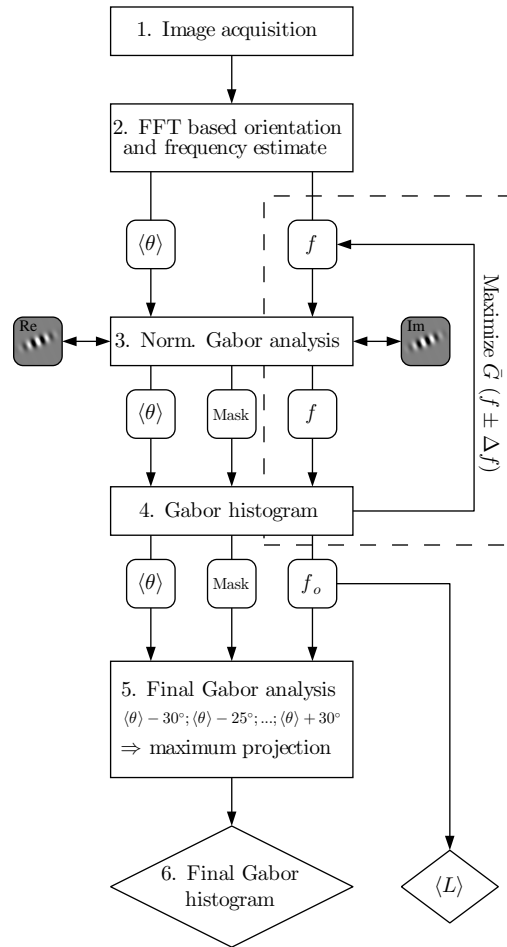


**Figure 6.1:** Automated Gabor analysis flow chart.

## 6.4 Results

### 6.4.1 Typical patterns and their Gabor values

To correctly interpret the resulting Gabor values, the Gabor histograms of representative sarcomere structures and anomalies are given in Fig. 6.2. In panel Fig. 6.2 A and B the difference between the original and normalized Gabor values, respectively, is shown for the same regular sarcomeres. Without normalization, the Gabor distribution contains two distinct peaks with a central value of  $\sim 69$  and  $\sim 55$ , which is a 20% difference. The distinct peaks suggest the image contains structures with different frequencies. However, a one dimensional FFT analysis along the sarcomeres indicates that the frequency mismatch is only apparent (data not shown). The FFT reveals a peak having a width representing a 2.5% frequency spread, corresponding to a 1% normalized Gabor value decrease according to eq. (6.7). After normalization (Fig. 6.2 B), the Gabor histogram contains only one peak at an average value of 0.932. The standard deviation of 0.018 matches a 2% spread and resembles the mismatch deduced from the FFT analysis. This typical example shows the explicit need for the normalization procedure. From here on, only the normalized Gabor values ( $\bar{G}$ ) are considered.

A first type of anomaly that can be detected using the normalized Gabor analysis is a pattern where the signal appears to come from one half of the thick filament (Fig. 6.2 C-D). In these structures, often referred to as pitchforks[91], the A-band splits into two smaller myosin regions. One of these two regions typically has a higher SHG intensity. Both sides of the split A-band recombine with the parts of a neighboring pitchforked A-band, resulting in a different A-band. Pitchforks can occur on both short (Fig. 6.2 C), or longer transversal length scales (Fig. 6.2 D). However, the Gabor values are independent of this length scale and consistently range from about 0.6 in the center of the pattern to above 0.85 near the fully formed sarcomeres.

A second type of anomaly is the double band pattern, which was suggested in previous studies as a typical feature for proteolytic muscle tissue [36, 91]. The double band features will comprise substantial amounts of higher frequency components and therefore results in lower Gabor values, down to a normalized Gabor value of 0.08 when the pattern only contains this doubled frequency. In most cases the double band pattern contains a combination of the reference frequency  $f$  and the doubled frequency, resulting in Gabor values ranging from 0 to 0.6 (Fig. 6.2 E).

The last representative pattern is a technical artifact rather than a sarcomere anomaly. SHG images of sarcomeres will contain myocyte boundaries and background (dark) regions that are also analyzed by the protocol (Fig. 6.2 F). However, these image regions do not contain valuable information on the sarcomere regularity, and, when not properly excluded from the Gabor histogram, even result in an apparent decreased sarcomere regularity. The boundary and background regions are therefore excluded from the Gabor histogram by the mask defined in section 6.3.5,

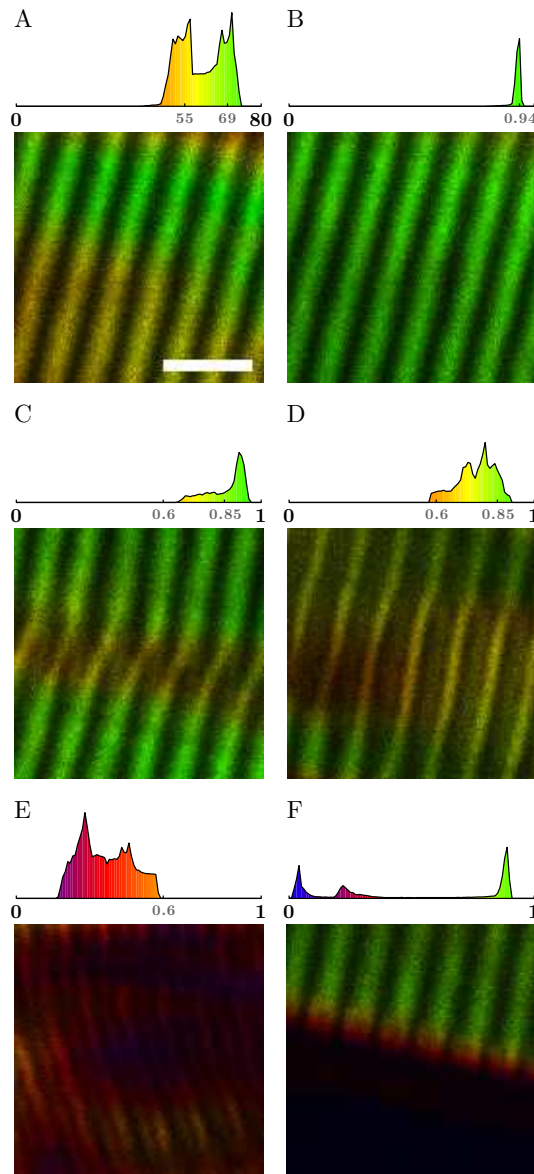


**Figure 6.2:** Typical results of the suggested Gabor filter. The color map represents the Gabor value, as specified in the histogram above each image. Each panel shows a cropped region of a larger image containing background regions. (A) Typical proper sarcomere pattern without normalization ( $G(x, y)$ ). (B) The same data as (A) with normalization ( $\bar{G}(x, y)$ ). Panels C-F also represent the normalized Gabor coefficients. Typical irregularities such as pitchforks (C) and thinned regions (D) show a slight decreased normalized Gabor value. Other typical structures contributing to the Gabor histogram of an image are: (E) double band regions and (F) edge effects and dark regions (no mask applied for illustrative purposes). Scale bar  $5 \mu m$ . All images have the same field of view.

eliminating the additional histogram peaks near  $\bar{G} = 0$ .

In general, all aforementioned patterns contribute to the final Gabor histogram, which represents the sarcomere regularity in the entire SHG image. It appears that a Gabor value below 0.6 always maps disordered sarcomeres. Values between 0.6 and 0.85 indicate myocyte alterations related to an increasing or decreasing number of sarcomeres, indicated by the presence of pitchforks [91]. Finally, values above 0.85 will always represent regular sarcomere patterns and are considered as good and healthy regions.

#### 6.4.2 Gabor value correlates with myosin disorder

In order to link the obtained  $\bar{G}$  to sarcomere disorder, the correlation between the normalized Gabor value and the M-band size was studied. This was done on a set of samples taken from healthy animals, and EAE induced animals for which sarcomere degradation was expected. A broad range of values for  $M$  was obtained by analyzing manually selected intensity profiles from samples of both animal groups. The automatically determined normalized Gabor value corresponding to each profile was taken from the pixel at the profile center. For each intensity profile,  $\bar{G}$  is plotted against the corresponding  $M$  in Fig. 6.3.

For  $M < 0.3 \mu m$ , the normalized Gabor value is essentially constant, indicating no detectable change in the SHG profile. Above this threshold value, a transition from single to double band occurs, resulting in a rapid decrease of  $\bar{G}$ . A correlation between  $M$  and  $\bar{G}$  exists, validating the applicability of our Gabor approach to automatically estimate sarcomere (ir)regularity from entire SHG images. The observed  $M$ - $\bar{G}$  correlation was additionally verified by means of simulations. For each M-band size,

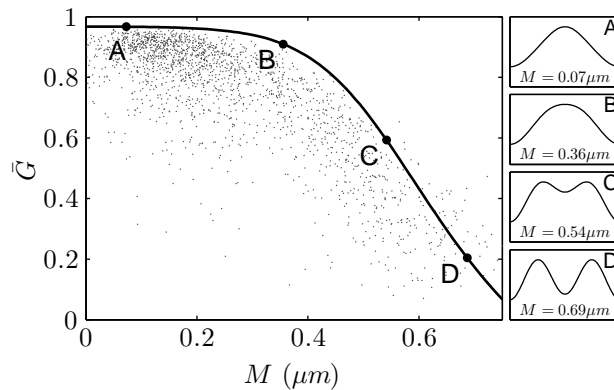


**Figure 6.3:** Sarcomere disorder quantified by  $M$  versus normalized Gabor value  $\bar{G}$  correlation. The maximum possible normalized Gabor value is indicated by the solid line (simulated). Panels A-D show the simulated profile of the given M-band size.

images containing only one type of sarcomere were simulated in accordance with experimental conditions, and analyzed with the normalized Gabor approach. The resulting maximum possible  $\bar{G}$  for each  $M$ , shown by the solid line in Fig. 6.3, clearly indicates the upper limit of the experimental data. The simulations show that the Gabor approach is less sensitive to small M-band sizes, while for  $0.3 < M < 0.75$  the method is highly sensitive.

For the entire data set, the correctness of sarcomere length obtained by the Gabor analysis was additionally evaluated. Besides sarcomere disorder, the analysis of manually selected intensity profiles provides the sarcomere length, which was used as a reference. For all data points shown in Fig. 6.3, the resulting sarcomere length was  $2.2 \pm 0.1 \mu m$  (mean  $\pm$  standard deviation). The sarcomere length resulting from the automated Gabor analysis, averaged over all images, similarly yielded  $2.2 \pm 0.1 \mu m$  (mean  $\pm$  standard deviation). For the entire data set, both methods thus yield the same average sarcomere length, which lies within the physiological working range of sarcomeres[131].

### 6.4.3 EAE affects sarcomere integrity

Using the Gabor histograms, the effect of EAE on sarcomere integrity was studied. For this, the global EAE severity of each animal is measured by the pain score averaged from the day of EAE induction to the day of sample collection ( $\langle PS \rangle$ ). The data used in the previous section were divided into three groups: a healthy control group ( $n = 5$ ), animals with a time averaged pain score below 1 ( $\langle PS \rangle < 1$ ,  $n = 5$ ) referred to as mild EAE, and animals with a time averaged pain score above 1 ( $\langle PS \rangle > 1$ ,  $n = 3$ ) referred to as severe EAE. For each animal, the Gabor histograms of 4 to 6 SHG images from different slices were combined, resulting in one Gabor histogram per animal. These histograms, combined per animal group, are shown in Fig. 6.4.

Relative to the control group, the Gabor histogram shifts towards lower values only for the severe EAE group. According to previous observations (Fig. 6.2), this shift is mainly due to transformation from regular single band SHG patterns into double band patterns. The control, mild EAE and severe EAE histogram cross at values representative for pitchfork structures (see Fig. 6.2) indicating little or no change in their prevalence. The mild EAE group shows no clear difference with respect to the control group. Only small differences are observed at  $\bar{G} > 0.85$ , for which no sarcomere alterations were assumed. Moreover, statistical comparison of the median normalized Gabor values ( $\bar{G}_{1/2}$ ) shows no significant difference between both groups. Only the severe EAE group has a significantly lower  $\bar{G}_{1/2}$  ( $p < 0.001$ ) relative to both the control and mild EAE group.

The fact that severe EAE results in lower median normalized Gabor values than mild EAE suggests that a correlation exists between the EAE pain score on which data grouping was based, and the muscle quality assessed by the Gabor analysis. To emphasize this correlation, the time averaged EAE pain score ( $\langle PS \rangle$ ) is compared to

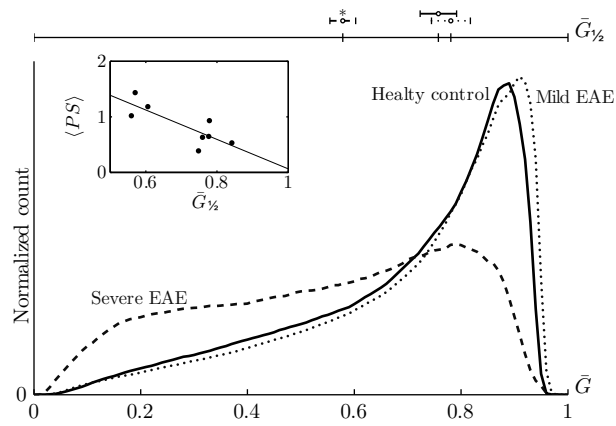


**Figure 6.4:** Gabor histograms of healthy control group ( $n = 5$ ), the mild EAE group ( $n = 5$ ) and the severe EAE group ( $n = 3$ ). As indicated on the upper horizontal axis, a significantly lower median Gabor value ( $\bar{G}_{1/2}$ ) for the severe EAE group is observed ( $p < 0.001$ ). The inset shows the correlation between  $\bar{G}_{1/2}$  and the time average pain score ( $\langle PS \rangle$ ). The solid line is a linear fit serving as a guideline to emphasize this correlation.

the median Gabor value of each animal. The result is shown in the inset in Fig. 6.4. A correlation analysis reveals a correlation coefficient of  $-0.81$  ( $p < 0.05$ ), indicating a strong relation between the average pain score and the median Gabor value.

## 6.5 Discussion and conclusions

We introduced a new and automated method based on Gabor analysis to accurately characterize the sarcomere quality from an SHG microscopy image of skeletal muscle. Instead of performing a full Gabor decomposition, we chose to analyse the image with only one frequency that is related to the sarcomere length, and give interpretation to the resulting normalized Gabor values. First, the Gabor values can be linked to typical sarcomere SHG profiles, either regular structures giving rise to single band profiles, or any of the discussed anomalies that are detectable by SHG microscopy (Fig. 6.2). Second, we showed that the resulting Gabor values relate to sarcomere disorder quantified by the M-band size, giving a structural meaning to the Gabor values. Compared to the analysis of manually selected profiles, previously used to obtain the same structural information, the Gabor method is objective and extremely fast. Our fully automated sarcomere integrity mapping requires only the image as input, provided that it contains a preferential sarcomere direction and a background region. The analysis occurs in less than 5 seconds for a 2048x2048 8-bit image using a graphical processing unit. Moreover, the method gains information on the entire image instead of just a few manually selected intensity profiles.

We believe that the newly introduced normalization method forms the strength of the proposed Gabor analysis. Normalization makes the interpretation of the results independent on imaging properties such as illumination power or detector gain, but also local intensity variations due to opacity properties of tissue above and below the scanning plane are circumvented.

We assumed that all sarcomeres are contracted similarly such that sarcomere length is the same for all sarcomeres, including possibly irregular ones. Moreover, we have not studied the relation between sarcomere integrity and sarcomere length. One could anticipate that for increasing sarcomere length, the base frequency has a lower relative contribution for well ordered sarcomeres because the A-band length remains constant. Since  $\bar{G}$  estimates this relative contribution, longer sarcomeres will yield lower normalized Gabor values, even for well ordered sarcomeres. The normalized Gabor approach thus needs to be revised when considering samples with longer sarcomeres.

This study was limited to images taken with an objective having a moderate NA=0.75. If one would prefer a higher resolution, in spite of our recommendation to use moderate NA objectives [157], typical sarcomere anomalies (Fig. 6.2) might be characterized by different normalized Gabor values. Moreover, the  $M - \bar{G}$  relation (Fig. 6.3) might alter. For regular sarcomeres, this can be expected due to the more pronounced shoulder regions [157]. These shoulder regions are described by higher harmonics, causing a lower relative contribution of the base frequency, and thereby a lower  $\bar{G}$ . Additional work is thus needed to use the approach presented in this work for images obtained through elevated NA objectives.

When introducing the theoretical background of our Gabor approach, we consid-

ered SHG intensity oscillations as a single harmonic function with the base frequency related to the sarcomere length. This is not in accordance with the model developed by Rouède *et al.* [36]. Consequently, the normalized Gabor value will never reach its maximum value of 1, as can also be observed from the simulation results shown in Fig. 6.3. The maximum normalized Gabor value approaches  $\bar{G} \approx 0.97$  for regular profiles ( $M \approx 0$ ), meaning that about 97% of the profile consists out of the base frequency. By inspection of the amplitude spectrum of the SHG profile calculated by the supra-molecular model, we found that 98% of the profile is represented by the base frequency. This indicates that the normalized Gabor value closely resembles the expected value given by the supra-molecular model. Moreover, the simplified phenomenological model is an acceptable 3% off for regular sarcomeres, making our Gabor approach ideal to locate regular, and therefore irregular sarcomeres.

Note that at a given  $M$ , experimental values of  $\bar{G}$  are mainly lower than the theoretical maximum estimated from simulations (Fig. 6.3). This might be a consequence of the single frequency approach which does not cope with small variations in the sarcomere contraction state. Moreover, manually selected profiles might be located close to anomalies which could slightly affect the Gabor values at the profile site due to the lateral kernel dimension  $\sigma_y$ .

We have not thoroughly tested the effect of the imaging noise level on the normalized Gabor values. Yet, because of the selected kernel size, spatial noise will be Gaussian averaged over a range of pixels, improving the signal to noise ratio by a factor of  $\sim 40$  relative to the original imaging noise. Conversely, this approach overlooks irregularities occurring on length scales of individual sarcomeres. However, our approach is still more sensitive to local variations than for instance the grey level co-occurrence matrix method described by Liu *et al.* [93], in which the complete selected region is represented by a single oscillating profile. And although we similarly propose to condense the full Gabor image into a single histogram for easy interpretation, the local information remains present in the initial Gabor analyzed images and can always be referred to.

The applicability of our new Gabor analysis was tested in the context of EAE induced muscle degradation. To our knowledge, this is the first time SHG microscopy was used to assess sarcomere quality in an EAE study. We showed that the Gabor histograms represent sufficient information to compare the different biological conditions. A significant decrease of the median Gabor value is observed for the severe EAE animals with an average pain score above 1. As these animals typically showed multiple relapses before sample collection (data not shown), the number of relapses seems to have an effect on muscle quality. Based on these results, we can however not state that the decreased muscle quality is a direct consequence of muscle disuse. EAE is known as an inflammatory disease of the central nervous system (CNS), and the resulting systemic inflammatory signals mediate the skeletal muscle metabolism, eventually resulting in muscle atrophy [132]. As each relapse coincides with an increased inflammatory state [133], the observed relation between number of relapses

---

## DISCUSSION AND CONCLUSIONS

through the average pain score and the muscle quality suggests indeed that muscle atrophy is related to CNS inflammation rather than muscle disuse. Although additional work is required to prove this statement, the observed relation seems to suggest that relapsing-remitting EAE might not be an appropriate model for studying MS related sarcomere alterations.

In our study only rat muscle samples were used for the verification and application of the new Gabor approach. However, because striations are typical for skeletal muscle of all vertebrae, and because of a low variability of the sarcomere architecture among vertebrate species [134], the Gabor analysis can be directly applied to study skeletal muscle of other vertebrates. This makes the analysis applicable in human studies or in a more clinical context.

Although effects of microscope settings such as illumination intensity and detector gain are taken into account by the normalization procedure, sample collection and handling can still influence the muscle quality. Direct *in vivo* multi-photon micro-endoscopy circumvents this issue [135, 136], making painful biopsy extractions unnecessary and thereby facilitating muscle research in humane studies. The focus of the current work lies at forward directed SHG signals, while micro-endoscopy relies on the collection of backward directed signal. Additional work is therefore required to study the relation between muscle quality and backward directed SHG signals. Still, we strongly believe that micro-endoscopy in combination with our fast Gabor analysis method can be used as a reliable and real-time muscle quality assessment tool for the study and possibly early detection of various diseases affecting the structural integrity of skeletal muscle.

## **Acknowledgement**

We would like to thank drs. Stelios Ravanidis and prof. Niels Hellings for providing us the muscle samples, and dr. Leen Slaets for sharing her insights concerning the EAE rat model.

This research is part of the Interreg EMR IV-A project BioMiMedics ([www.biomedics.org](http://www.biomedics.org)) and is co-financed by the European Union, local governments, research institutes and SMEs. Support by the BELSPO funded IAP-PAI network P7/05 on Functional Supramolecular Systems (FS2) is acknowledged. The Province of Limburg (Belgium) is acknowledged for the financial support within the tUL IMPULS FASE II program, allowing for the upgrading of the laser source used in this work.

## **CHAPTER 7**

---

# **Sarcomere second harmonic generation intensity profile depends on sample thickness**

---

**Paesen, R., Hadraba, D., Bito, V. & Ameloot, M.** Sarcomere second harmonic generation intensity profile depends on sample thickness. *In preparation* (2015)

## 7.1 Abstract

In studying striated muscle by second harmonic generation (SHG) microscopy, thick filament and myofibril misalignment were previously pointed out as possible causes for transition from single band to double band and irregular SHG intensity profiles. The filament disorder is often considered as a measure for muscle degradation due to muscle pathologies or proteolysis. By means of simulations and experimental evidence, we show that, besides filament disorder, the sample dimensions are additionally crucial in defining the SHG intensity profiles. For both thin slices of skeletal muscle and individual cylindrical myofibrils, a thickness or diameter below  $2\ \mu\text{m}$  always leads to double band intensity patterns, even for regularly aligned filaments. This implies that sample slices should always be thicker than an imaging device dependent threshold value to obtain unbiased results when studying skeletal muscle. Additionally, based on our results, the fact that SHG images of healthy cardiac muscle tissue primarily contain double band intensity profiles is explained. Since cardiac muscle fibres are not as aligned as skeletal muscle fibres, and inter-fibre distances are greater due to larger and more mitochondria, we hypothesize that the effect of individual fibril diameters plays a major role in defining the SHG intensity profiles of cardiac muscle tissue.

## 7.2 Introduction

Second harmonic generation (SHG) microscopy is known as an excellent tool to study sarcomeres in striated structures, either originating from cardiac or skeletal muscle tissue [23, 63, 91]. The specificity of the SHG signal allows the detection of alterations in the thick filament [36, 157, 91] and myofibril organization [107]. It was previously shown that nanometer-sized shifts of neighboring thick filaments already induce detectable changes of the SHG intensity profile [36, 157]. Therefore, a detailed analysis of SHG intensity profiles hold promise as a sensitive tool for early detection of pathology related sarcomere alterations.

Sarcomere regularity is typically assessed by the SHG intensity profile along the sarcomere direction. It is known that for bulk regular sarcomeres, found in healthy skeletal muscle tissue, the SHG intensity patterns are so called single banded, with a single intensity peak at the center of the A-band, and a low intensity at the Z-lines [36, 157] (Fig. 7.1a). Two types of structural rearrangement have been identified in which a transition occurs from single to double band intensity patterns. Due to tissue degradation, thick filament disorder causes an intensity drop at the center of the A-band, leading to double peaked intensity patterns (Chapter 5). Besides thick filament disorder, a myofibrillar misalignment is known to induce double band intensity profiles [137]. Yet, we (Fig. 7.1) and others [63, 107] have observed double band SHG patterns in both healthy cardiac muscle tissue (Fig. 7.1b) and individual skeletal myofibrils.

In general, SHG intensity profile changes have been observed experimentally in skeletal muscle tissue and are typically studied using theoretical SHG models for sarcomeres [36, 157, 137]. These so called supra-molecular models are based on the detection of unperturbed, forward directed SHG signals. However, biological tissue

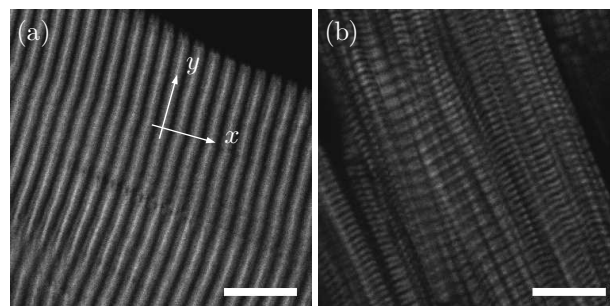


**Figure 7.1:** Typical forward SHG image of skeletal muscle (a) and cardiac muscle (b). The skeletal muscle mainly contains single band patterns, while the cardiac muscle shows predominantly double band patterns. For a description on preparation of skeletal muscle, see Chapter 5. Scale bar 10  $\mu\text{m}$ . The axes indicated in (a) are related to the axes used in Fig. 7.2.

turbidity might induce optical artifacts which alter the forward directed SHG signal, resulting in SHG intensity profiles that do not correctly represent the degree of sarcomere regularity. Moreover, muscle tissue is known to be optically dense, possibly preventing any forward directed signal to be detected at all. To make forward SHG detection of muscle tissue possible, and to be able to unambiguously link the intensity profiles to sarcomere regularity, samples size should be kept low by either making thin slices of bulk muscle tissue, or by extracting single cylindrical myofibrils with a diameter ranging from 1 to 2  $\mu\text{m}$  [63, 107, 138, 139]. However, due to coherence properties of SHG, one needs to be cautious when lowering sample dimensions. Using both simulations and experimental evidence, we here show that limited sample dimensions along the illumination wave vector and sample edge effects undesirably affect the SHG intensity profiles as well, causing regular sarcomeres to appear as double band profiles. This explains the observed double band patterns in *e.g.* healthy micrometer sized myofibrils. The thickness assessment is performed for both cylindrical myofibril shapes found in cardiac muscle tissue, and for slices of bulk skeletal muscle tissue. Based on these results, we can define a lower limit of sample dimensions such that intensity profiles can be interpreted correctly in the context of sarcomere irregularity.

## 7.3 Methods and material

### 7.3.1 Sample preparation

Usage of all animal material was approved by the animal Ethics Committee of Hasselt University, and was in accordance with the national and European legislation. The National Research Council's guide for the care and use of laboratory animals was followed.

#### Skeletal muscle tissue

For this, glutaraldehyde fixed healthy rat *Flexor Digitorum Longus* muscle tissue was used. The muscle tissue was dissected and handled with a standard protocol for making electron microscopy slices. In short, the samples were fixed overnight in 2% glutaraldehyde at 4 °C, and post fixed in osmium tetroxide. Afterwards, the samples were dehydrated in graded concentrations of acetone, and embedded in epoxy resin (Araldite) for slicing. Sections were made on an ultramicrotome (Leica EM UC 6, Wetzlar, Germany), and their effective thickness was measured using a Bruker Dektak XT (Billerica, MA) profiler.

#### Cardiac muscle tissue

Healthy rat hearts were excised, cut transversely and fixed overnight with 4% paraformaldehyde at 4 °C. Afterwards, samples were cryoprotected by saturation with 30% sucrose in phosphate buffered saline. Slices were made using a cryostat (CL 1990 UV, Leica, Wetzlar, Germany), mounted on microscope glasses, embedded in Immu-Mount™ mounting medium (Thermo Fisher Scientific, Waltham, MA) and sealed using a cover slip (Menzel-Gläser, Thermo Fisher Scientific, Waltham, MA).

### 7.3.2 Microscopy

The imaging was done using a confocal Zeiss LSM510 mounted on an Axiovert 200M (Zeiss). A 40x oil immersion objective with numerical aperture (NA) of 1.3 was used (Plan-Neofluar 40x/1.3 Oil DIC, Carl Zeiss, Jena, Germany). Sample illumination was provided by a femto-second pulsed MaiTai-DeepSee (Spectra-Physics, CA) laser tuned at a central wavelength of 810 nm. The forward directed SHG signal was collected by a condenser with a numerical aperture of 0.8. The signal passes a short pass filter with an edge at 660 nm and a narrow band pass filter (400-410 nm), and was measured by an analogue photo-multiplier tube (Delivered by Zeiss).

The point spread function (PSF) dimensions were obtained as described in chapter 5. For the used objective,  $w_{xy} = 0.467 \mu\text{m}$  and  $w_z = 1.946 \mu\text{m}$ .

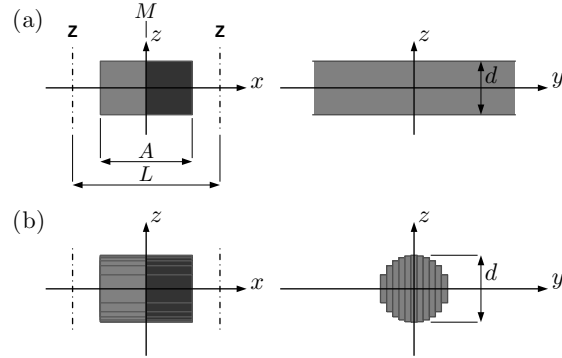


**Figure 7.2:** Simulation framework for thin slices of skeletal muscle (a) and cylindrical shaped myofibrils (b).  $A$ ,  $L$  and  $M$  are defined as in figure 5.1a. The illumination beam travels along the  $z$ -direction. The change in grey level in the  $x$ -direction indicates myosin thick filament direction reversal. The axes definition is additionally illustrated in Fig. 7.1a.

### 7.3.3 Simulations

For a full description of the simulation framework, the reader is referred to the original work by Rouède *et al.* [107], combined with chapter 2. In short, the simulation assumes a Gaussian beam with lateral size  $w_{xy}$  and axial size  $w_z$  that illuminates sarcomere structures which are implemented as solid blocks. Each block gives rise to a specific SHG emission pattern. The SHG intensity for a certain position of the illumination beam with respect to the structure is obtained by summing the emission patterns of all blocks, and integrating this pattern over the full collection angle of the condenser. In our work, the dimensions of the illumination beam are based on a 40x1.3 oil immersion objective, combined with an illumination wavelength of 810 nm. We used a condenser with a numerical aperture of 0.8 to collect the SHG signal in forward direction.

To mimic a slice of the bulk skeletal muscle, we used a single block of thickness  $d$  along the axial direction of the illumination beam ( $z$ ), and a sufficiently large size ( $5 \mu\text{m} \gg w_{xy}$ ) along the lateral  $y$ -direction (Fig. 7.2a). A cylindrical myofibril having diameter  $d$  is implemented as a series of blocks with a size of  $0.1 \mu\text{m}$  in the  $y$ -direction, and a varying size along the  $z$ -direction, as depicted in figure 7.2.b. The thickness effect is studied by performing simulations with varying slice thickness or fibril diameter, ranging from  $1 \mu\text{m}$  to  $2.6 \mu\text{m}$ , related to the typical myofibril diameter range. For both the slab and the cylinder, the  $y$  and  $z$  periods are taken  $15 \mu\text{m}$  in accordance with Rouède *et al.* [107]. After our previous observations for the 40x objective with  $\text{NA} = 1.3$  (Chapter 5), the size of the sarcomere A-band ( $A$ ) is taken  $1.38 \mu\text{m}$ , the M-band length ( $M$ ) is  $0.03 \mu\text{m}$ , and the sarcomere length ( $L$ ) is  $2.2 \mu\text{m}$ . The refractive index at the illumination wavelength is set to  $n_\omega = 1.390$ , and at the

SHG wavelength  $n_{2\omega} = 1.418$ .

## 7.4 Results

### 7.4.1 Simulations of thickness dependence and edge effects

SHG intensity profiles of regular sarcomeres were simulated as a function of sample dimensions. In Fig. 7.3 the intensity profiles are shown for slices of thickness  $1.0\ \mu\text{m}$  upto  $2.6\ \mu\text{m}$  with a  $0.2\ \mu\text{m}$  step size. In Fig. 7.4 the intensity profiles originating from cylindrical geometries, having a diameter ranging from  $1.0\ \mu\text{m}$  upto  $2.6\ \mu\text{m}$  with a  $0.2\ \mu\text{m}$ , are shown. For both geometries, the simulations show that, even for regular sarcomeres, a double band intensity profile exists for low thickness or diameter. At the axial and lateral center of each structure (solid line), a transition from double band to single band occurs for increasing thickness. Using the second order derivative (SOD) value of the simulated intensity profile at the M-line, the single to double band transition point was determined. Double band patterns have a positive SOD value, and single band intensity profiles have a negative SOD values. The single to double band transition point is then given at the value where the SOD changes sign. The transition point lays at  $2.18\ \mu\text{m}$  for the slices and at  $2.21\ \mu\text{m}$  for the cylinders.

Similarly, the lower limit at which sample thickness or diameter does not affect intensity profiles any more can be assessed. We define this limit as the point where the SOD approaches its maximum value. It was found that for a thickness or diameter above  $6\ \mu\text{m}$  the profiles remains unchanged.

Notice that towards the sides of the structures, both in the  $z$ -direction for slices (dashed line) and in the  $y$ - and  $z$ -direction for the cylinder (dotted and dashed line respectively), a double band structure remains present for the studied dimensions. This shows that besides the structure dimensions, also structure edges play a crucial role in defining the SHG intensity profile.

### 7.4.2 Experimental verification of slice thickness

To verify the simulation results for thickness dependence of slices, thin slices of healthy skeletal muscle were imaged and the resulting intensity profiles were compared to the theoretical profiles (Fig. 7.5). For this, we selected a sample thickness below and above the double to single band transition point ( $2.18\ \mu\text{m}$ ). For  $d = 2.38\ \mu\text{m}$  a single band pattern appears, while for  $d = 1.09\ \mu\text{m}$  a double band exists. Note that although we show only a selected area, we were not able to locate any single band intensity profiles in thinnest sample. The dots in Fig. 7.5 are obtained by averaging the representative region over their full sarcomere width (vertical direction inside the image). The solid lines were not fitted to the experimental data. They were calculated using all previously mentioned parameter values and the accordingly measured sample thickness. A remarkably good resemblance exists between the experimentally obtained profiles and the simulated ones, strongly confirming our simulated data.

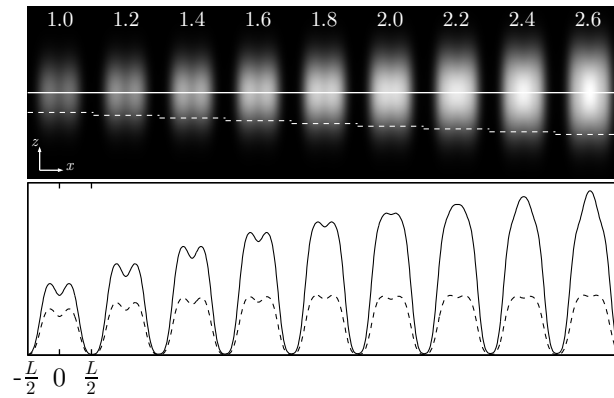


**Figure 7.3:** Simulation results for the SHG scan in the  $x$ - $z$  plane at  $y = 0$  for thin slices of skeletal muscle with varying thickness  $d$ . Each number indicates the sample thickness in micrometers for the given sarcomere. The intensity profile in the center of each sarcomere (solid) and at the axial ( $z$ ) sides of the sarcomere (dashed) are given for increasing sample thickness.

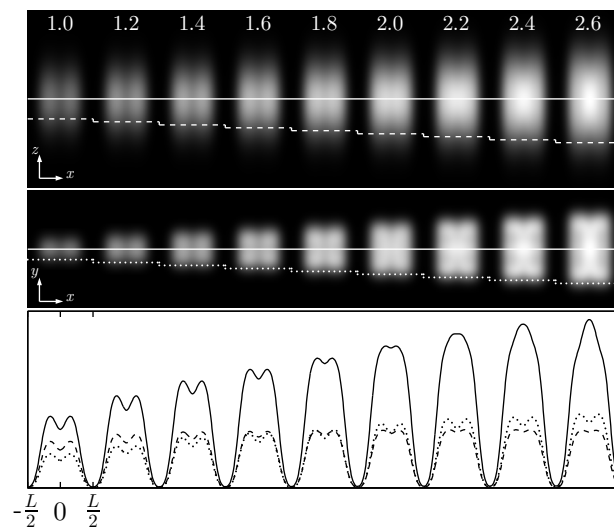


**Figure 7.4:** Simulation results for the SHG scan in both the  $x$ - $z$  plane at  $y = 0$ , and the  $x$ - $y$  plane at  $z = 0$  for cylindrical myofibrils of varying diameter  $d$ . The number in the  $x$ - $z$ -panel indicates the fibril diameter  $d$  in micrometers. The intensity profile in the center of each fibril (solid), and at the axial edge (dashed) and at the lateral edge (dotted) of the fibrils are given.

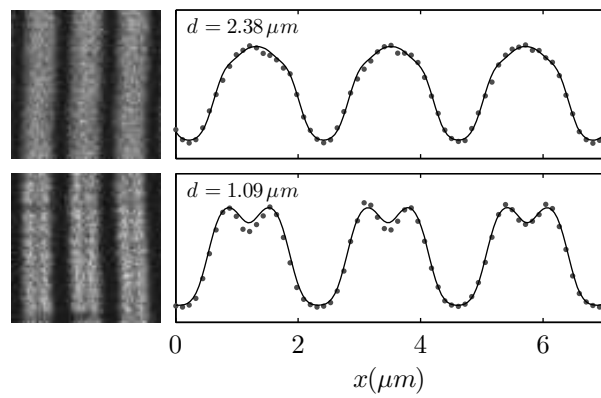


**Figure 7.5:** Experimental verification of the effect of sample thickness on the SHG intensity profiles of healthy skeletal muscle. The dots are obtained by averaging the left images along the full width of the sarcomeres (vertical direction). The solid lines are obtained by simulations using the prior measured thickness.

## 7.5 Discussion and conclusions

Although double band patterns are known to exist in the context of thick filament or myofibrillar misalignment, we (Fig. 7.1) and others [63, 107] show that this specific profile is not limited to pathological situations. Indeed, double band SHG patterns were shown in healthy cardiac muscle tissue as well as in regular individual myofibrils. Using simulations with a supra-molecular model, which were confirmed by experimental evidence, we now showed that for both cylinders and thin slices smaller structure dimensions give rise to double band intensity patterns.

Note that a high NA objective was used in this work. Yet, in our previous work we recommended using moderate NA objectives in order to not induce additional polarization components which are not implemented in the supra-molecular model (Chapter 5). We used the high NA objective in order to observe a clear transition from single to double band patterns at a workable range regarding sample preparation. Based on simulation we know that lowering the objective NA to 0.8 causes the transition point to shift to  $3.14\mu\text{m}$ , for which sample preparation becomes less evident due to equipment limitations. Moreover, high NA objectives are often preferred for their elevated resolution which is required to study individual myofibrils. Taken together, the objective NA affects the transition point meaning that this is not an absolute point, and only holds for the given system and physical parameters.

The results regarding the A-band length, obtained in chapter 5, were used to simulate the theoretical profiles for comparison with experimental data, as shown in figure 7.5. However, both chapters rely on different sample preparation techniques and procedures. In chapter 5, the sample was fixed using PFA. In this chapter, glutaraldehyde was used, a different cross-linking agent, yet with the very same functional aldehyde groups. As the theoretical profiles, based on PFA fixed samples, compare well with the experimental profiles, based on glutaraldehyde fixation, we conclude that possible effects due to different fixation techniques are negligible for SHG microscopy.

The effect of sample dimensions can be used to explain why primarily double band patterns are observed in cardiac muscle tissue. One cause of SHG double bands is found at the typical myofibrillar misalignment [140], which is known to result in intensity profile alterations [137]. However, compared to skeletal muscle tissue, cardiac muscle tissue has more and larger mitochondria located between myofibrils [141], such that cardiac myofibrils may need to be considered individually regarding SHG microscopy. Since the observed transition point of  $2.21\mu\text{m}$  lies out of the range of cardiac myofibrils diameter  $1\text{-}2\mu\text{m}$ , the majority of the fibrils will appear as double band intensity profiles (Fig. 7.1 b). The SHG image of cardiac muscle however contains single band intensity profiles as well. This can be related to coincidental alignment of neighboring filaments.

The lateral changes observed in the  $x$ - $y$ -sections of Fig. 7.4 are also observed experimentally (Fig. 7.1 a). In the simulations, the A-band seems to split toward the

sides. In the experimental data, the A-bands at the myocyte edge also seem to split into two parts, similar to the splitting at the so called pitch-fork structures [91]. This does not occur for all lateral sarcomere edges, even within a single myocyte (Fig. 7.1 a). The effect might be a consequence of the sample slicing. In case an upper or lower cut of a cylindrical myocyte is taken, wedge-like edges become sufficiently thin to induce double band patterns. If a slice is taken from the center of a myocyte, this thinning is not likely to occur.

The insight obtained in this work give rise to some considerations when preparing skeletal muscle samples for forward SHG microscopy. If one is interested in studying the degree of sample degradation by means of double band profiles [36, 158], two items are crucial to obtain unbiased results: the sample slices should be sufficiently thick, and imaging at the upper or lower edge of the slice should be avoided. For the given system parameters, simulations indicate that it is advisable to make slices of at least  $6\ \mu\text{m}$  thickness to cope with both items. Note that thicker samples might result in illumination beam and emission profile distortion, both properties that affect the SHG intensity profile. When studying individual myofibrils or cardiac tissue by SHG microscopy, a double band profile does not necessarily indicate filament or fibrillar misalignment [157, 107]. If one is however interested in quantifying the intensity profiles [96, 98], the results might depend on the selected location: profiles at the edges of myofibrils will differ from those at the center.

To conclude, our results show that sample sizes influence SHG intensity profiles of sarcomeres, both for cylindrical myofibrils and thin slices of bulk skeletal muscle. Also the sample edges affect the intensity profiles, resulting in double band patterns even for regular structures. Both findings elucidate the importance of taking sample dimension into account when studying sarcomere regularity using SHG microscopy.

## **Acknowledgement**

We would like to thank Sophie Smolders, Inez Wens, Dorien Deluyker and Manolo de Hoyos Véga for muscle dissection and preparation, Prof. Ivo Lambrichts and Marc Jans for making thin sample slices, and Ilaria Cardinaletti for measuring the sample thickness.



## **CHAPTER 8**

---

# **General discussion, conclusions and outlook**

---

This chapter is partially based on the following publication:

Sanen, K., **Paesen, R.**, Luyck, S., Phillips, J., Lambrichts, I., Martens, W. & Ameloot, M. Label-free mapping of microstructural organisation in self-aligning cellular collagen hydrogels using image correlation spectroscopy. *Acta Biomater.* **30**, 258 –264 (2016)

## 8.1 General considerations

In this work, we assessed the applicability of existing biophysical SHG models and used them to study specific types of biological samples and tissue. We used those models to develop unbiased and unambiguous data and image analysis techniques to gain insight in properties of biological tissue imaged by SHG microscopy. As SHG microscopy is only possible on those few types of biological tissue, our work mainly focusses on well known endogenous SHG sources: collagen and myosin. Collagen was especially considered in the context of tissue engineering, where collagen type I hydrogels are used more and more often as a starting point for tissue growth. The myosin based research was mainly related to skeletal muscle, with a small note on cardiac muscle. In both these types of striated muscle myosin is present in a highly ordered fashion known as sarcomeres.

As each chapter already contains an in depth discussion and conclusion, we here shortly repeat the main conclusions and give some heads up on possibilities for follow up work. These future perspectives are not only continuations of chapters 4-7, but also contain ideas based on the calculations shown in chapter 2.

Before continuing with a discussion and outlook from a scientific and physical point of view, we first want to emphasize the importance of having hand-on experience with the used imaging device. The development, but mainly the verification of biophysical models starts at a thorough knowledge and decent functioning of the imaging device. Mainly for commercial machines, the user has to rely on information provided by the manufacturer, which is not always complete or correct. Therefore, one needs to design small experiments to test and sometimes disprove the features that were to be taken for granted according to the manufacturer. The condenser testing given in section 3.2 is an example of such an experiment. Besides optimizing the existing hardware, sometimes peripheral devices are required for experiments that are not standardized and implemented by the manufacturer. To perform automated P-SHG experiments, a device was designed that not only physically had to fit into the microscope body, but also needed to communicate with the controlling software. Although microscopes exist with more flexibility and transparency in their design, they suffer from increased complexity in handling. Whether a closed or an open system is preferred depends on the needs of the lab, but maybe more on the type of research that is the lab's core business. It is a trade-off between the researchers with different backgrounds that one encounters in a biophysics group: biologists like to work with a "push the button" device, while physicist prefer to know "what is going on in there". In either way, it often comes down to make do with the means that are at our disposal.

## 8.2 Collagen hydrogels

The tissue engineering part focusses on the structural analysis of collagen type I hydrogels by ICS. ICS can be considered as an image processing tool to obtain statistical information of the visualized features. ICS is a descendant of fluorescence correlation spectroscopy, which immediately makes it clear that the theory behind it relies on the incoherent sources such as fluorescent probes. The ICS theory for SHG of collagen fibrils we developed in chapter 4, also relies on the assumption of incoherent sources. For sufficiently low fibre densities the distance between fibrils makes the impact of this assumption negligible, while for elevated densities the signal coherency must be taken into account and will result in an altered ACF amplitude [85]. Yet, the observed relation between the collagen density and the ACF amplitude is still as expected (see Fig. 4.3), indicating that the working range is at least below the transition region of low to high density. Whether this working range is toward negligible low densities was not tested, although the resulting estimated fibre thickness lies in the expected range. Besides its effect on the ACF amplitude, coherency also affects the resulting images and thereby the shape of the ACF [85]. This can be explained on an intuitive basis using the fact that fibrils have a sense along their direction. Then two oppositely oriented coinciding fibrils will have no net signal, while two fibrils with equal sense interfere constructively, increasing their contribution to the ACF. Furthermore, fibre crossings might result in a constructive or destructive interference, yielding either very bright or very dim crossings, all of them features that contribute to the ACF.

A last point to address is the fact that the ICS technique was developed for a collection of collagen fibrils lying in the imaging plane. By allowing for a length variation, a 3D effect was mimicked. Although it has a detrimental effect on the extracted tensor parameters, the influence of the possible 3D orientation of the fibrils on polarization dependent SHG profile was not taken into account. Considering the same coordinate system as in Fig. 2.5, and assuming that the illumination polarization lies along the  $x$ -axis, the angle  $\alpha$  represents the spatial angle of a rotated fibre with respect to the  $x$ -axis. Then  $\cos \alpha = \sin \theta \cos \phi$  with  $\theta$  the angle with respect to the  $z$ -axis and  $\phi$  the angle between the fibre projected in the  $xy$ -plane and the  $x$ -axis. The polarization dependent SHG intensity can now be rewritten as

$$I(\phi) \sim \frac{1}{\pi} \int_0^\pi 4d_{26}^2 (1 - \sin^2 \theta \cos^2 \phi) \sin^2 \theta \cos^2 \phi + (d_{11} \sin^2 \theta \cos^2 \phi + d_{12} (1 - \sin^2 \theta \cos^2 \phi))^2 d\theta. \quad (8.1)$$

This equation can be used to correct the values obtained by using the in-plane P-SHG expression, or can be implemented directly in the ICS model proposed in Chapter 4 by replacing  $p(\theta)$  in Eq. (4.7) by  $I(\phi)$ . Despite all simplifying assumptions, the theoretical ACF remarkably well resembled the experimental one.

Due to the use of an angular modulation function, which was used to incorpo-

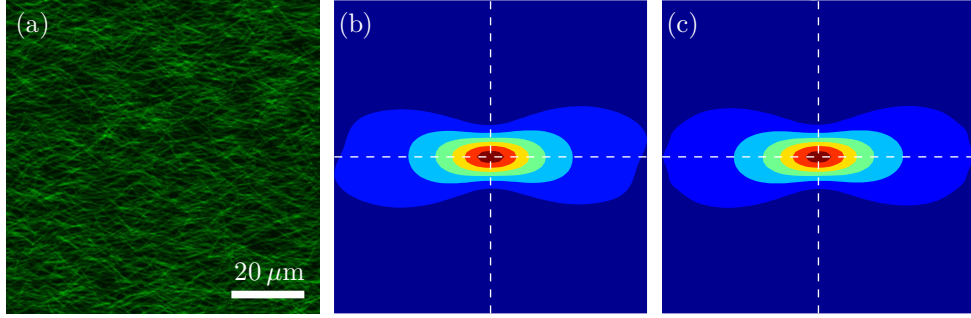


**Figure 8.1:** (a) Simulated hydrogel image based on the simulation method described in Chapter 4, with preferential orientation  $\mu = 0$  and spread  $\kappa = 2$ . (b) ACF of the simulated image shown in (a), and (c) the fit of the ACF shown in (b). The angular distribution related fit results are  $\mu = 0.01$  and  $\kappa = 2.05$ .

rated the polarization dependent SHG intensity, our fibre ICS model can be adapted for other types of applications as well. Our work was limited to full random fibre networks imaged by SHG microscopy. For this, a uniform angular probability distribution can be considered, yielding equal contribution of fibrils for all possible orientation. For other applications, fibrils within hydrogels are not oriented randomly, and a preferential fibril orientation exists [142, 143]. This suggest a non-uniform angular distribution  $\Phi(\theta)$ , which can be incorporated in the ICS model as [144]

$$g(\eta, \xi) = g_{00} \left| \sum_{i=1}^N g_{\theta_i}^1(\eta, \xi) \Phi(\theta_i) \right|. \quad (8.2)$$

Even more, in case these aligned collagen type I hydrogels are imaged by SHG microscopy with linearly polarized light, both the P-SHG effect and the preferential ordering can be included in the ICS model by

$$g(\eta, \xi) = g_{00} \left| \sum_{i=1}^N g_{\theta_i}^1(\eta, \xi) \Phi(\theta_i) p^2(\theta_i) \right|. \quad (8.3)$$

This elucidates the flexibility of the model, yet increasing the number of modulation functions also increases the number of free fit parameters. Using prior knowledge, this number of free fit parameters can be reduces. For instance, we have tested this approach by assuming an Gaussian like, Von Mises based angular distribution given by

$$\Phi(\theta) \propto \frac{e^{-\kappa \cos 2(\theta - \mu)}}{I_0(\kappa)} \quad (8.4)$$

with  $\kappa$  a dimensionless parameter representing the spread of the distribution,  $\mu$  the preferred fibre orientation and  $I_0(\kappa)$  the zeroth order Bessel function of the first kind.

In Fig. 8.1 an overview of these test results are shown. The P-SHG parameters are fixed to the predefined values in the ACF fitting step to keep the number of free fit parameters as low as possible. Only the amplitude, fibril length,  $\mu$  and  $\kappa$  are now the free fit parameters. The fit results look promising, indicating that the technique allows for a good estimate of the angular distribution.

Finally, the proposed ICS technique can be applied to fluorescent cases as well. One specific example is related to bacteria, for instance to estimate the density. Moreover, some bacillus species have a length around  $2\mu\text{m}$ , which lies in the range in which lengths are well estimated using our ICS technique (see Fig. 4.2). Our fibre based ICS model could thus be used to study bacterial growth, for which information on both the average bacterial size and the growth speed through the ACF amplitude is obtained.

## 8.3 Muscle tissue

### 8.3.1 Filament lengths

Striated muscle tissue is one of highest hierarchical biological structures available. Because of its strong SHG capacities, muscle tissue is one of the most studied tissues by SHG microscopy. For the muscle related studies, we spent a great deal of time on the correct interpretation of results obtained by sarcomere analysis by the supra-molecular model developed by Rouède *et al.* [36]. The most intriguing result obtained by the analysis was the shorter than expected A-band length of  $1.40\ \mu\text{m}$ , which was explained by the packing information of individual myosin filaments into a thick filament. This packing similarly explained the apparent M-band length of about  $0.07\ \mu\text{m}$ .

Not many sources report values on filament lengths studied by SHG microscopy. More often, the full width at half maximum (FWHM) is used as a representative value to characterize single band sarcomeres. In the study by Plotnikov *et al.* [63] the FWHM varies around  $1.1\ \mu\text{m}$ , and varies slightly depending on the sarcomere contraction state. As SHG images of skeletal muscle are readily available in literature, we measured the FWHM from those various sources and obtained an average value of  $1.0\ \mu\text{m}$ . In general, this FWHM deviates too much from the EM-related A-band length of  $1.6\ \mu\text{m}$ , indicating that the A-band length measured by SHG-microscopy will never compare to the EM values, even when taking coherency into account as was done in the supra-molecular model.

Note that we have only compared our SHG measurements with literature values of EM data. In this we relied on the low variability of filament length across vertebrate species [134], but also assumed filament lengths are stable and comparable when using different sample preparation methods. A better practice would be to perform both EM and SHG microscopy on the very same sample slices, and even of the very same sarcomere. This is not straight forward since slices for EM are typically only tens of nanometers thick. Besides the sample size effects on SHG profiles shown in chapter 7, we found that these extreme thin samples do not yield detectable SHG signals on the used SHG imaging device. Instead of using the exact same slice for both imaging techniques, single samples could be sliced in an alternate fashion, such that successive cuts can be used either for EM or SHG microscopy. The only remaining hurdle would then be the localization of the very same sarcomeres, which could be facilitated by insertion of markers.

Interpreting the apparent M-band length was less straightforward, even at the level of its definition. According to Luther *et al.* [145], the M-band is the region where neighboring thick filaments interconnect, occurring at the three out of nine central M-lines. The 9<sup>th</sup> or last M-line indicates the end of the bare zone, and therefore the bare zone is called the M-region. The nomenclature adopted by Rouède *et al.* [36] is confusing in two ways. Firstly, their M-band refers to the bare zone, or

M-region, instead of the thick filament interconnecting region. Secondly, when considering SHG signals, the location of interconnecting filaments nor the length of the bare zone are as defining as is the anti-parallel region. We therefore adopted the term apparent M-band length to indicate the effect of the amount of anti-parallel overlapping on the SHG intensity pattern. In retrospect, it would have been better to call this the apparent M-region. Nevertheless, the relation between the anti-parallel region and the M-region seems undefined, in that it depends on the considered packing model. Some models state that the myosin rods overlap completely in the full M-region, while other model propose a partial overlap. This all makes the observed apparent M-band length hard to interpret and compare to literature value. Moreover, the parallel myosin density gradually increase starting from the center of the thick filament, similar to the tapering at the end of the filament, yielding an apparent M-band length that is not the same as the full anti-parallel region. Strikingly, we obtained A-band and M-band length values comparable to the experimental values when considering a packing model with incomplete overlap at the center, and with tapering at the distal parts using the density as observed by Knight [105].

To get more insight in the effect of filament packing on the SHG intensity signal, it would be interesting to consider sarcomeres originating from species other than vertebrae [134]. As myosin packing is still not completely solved for many species, SHG microscopy can aid in this way to verify proposed packing models. Besides studying the packing models, it would be interesting to consider the effect of sarcomere contraction on the estimated filament lengths. Due to contraction, the HMM part (Fig. 5.1) of the myosin rod is known to slightly rotate away from the thick filament backbone, which probably results in a shortened apparent A-band length and differing apparent M-band length. This will be the most clear in the extreme case in which all heads are rotated outwards, which can be achieved by inducing *rigor mortis* [106]. By mechanically fixing the muscle at a certain length while *rigor mortis* sets in, possible effects of sarcomere length variations are ruled out, making a direct comparison of filament lengths in relaxed and *rigor* state straightforward. Finally, the supra-molecular model could be extended to take outward rotation of the HMM part into account. This was already done by Schürmann *et al.* [106] and Nuccioti *et al.* [90] to study the effect of HMM reorganization on the polarization response. Yet, they do not take spatial organization of myosin rods within the thick filaments into account as in Rouède's supra-molecular model, rendering their P-SHG models incomplete to study the filament. In general, extending the supra-molecular model with HMM re-orientation and including the packing models shown in chapter 5 will result in a more complete biophysical model to study spatial SHG patterns originating from striated muscle tissue.

The RI mismatch appeared to be extremely important in defining the SHG intensity profile. Based on the goodness of fit and using existing literature values, we estimated an appropriate value for the RI mismatch to continue our work. Measuring the effective RI properties of the used muscle tissue, whether it is fresh or treated tis-

sue, seems to be indispensable when studying sarcomeres using the supra-molecular model. This can for instance be done by the approach developed by Dirckx *et al.* [101]. For their approach, a confocal microscope is used which is often already available when performing SHG microscopy. The theory behind Dirckx' technique is straightforward, but complete control and detailed knowledge of the used imaging device, such as effective numerical aperture, is required. Moreover, the sample thickness must be accurately known. However, as we are mainly interested in the RI mismatch and not the effective RI (see sec. 5.5), Dirckx' approach in combination with a tunable pulsed laser is probably the best method to measure the RI mismatch. The RI wavelength dependence could be measured over the full wavelength range of the tunable laser, and extrapolated to the SHG wavelength using Cauchy's equation. In this way, possible effects of the high intensity laser pulses [6], required for SHG imaging, are taken into account. We had started to adopt this approach, but the results were unreliable up to now, and more work was to be done to be able to accurately measure the RI mismatch of our samples.

The in depth study of filament lengths obtained by the supra-molecular model forms the basis for applying SHG microscopy on muscle tissue in a more clinical context. In chapter 6 the effect of EAE on the sarcomere regularity was studied. We showed that for severe levels of EAE, the sarcomeres were arranged less regular than in healthy muscle tissue. This experiment could be considered as a top-down type of experiment in which we had no prior knowledge on what the effect of EAE would be on the sarcomere regularity. On the other hand, in chapter 5 we proposed that disrupted M-band filaments and bridges, normally interconnecting neighboring thick filaments in healthy tissue, are the cause of increased M-band and A-band lengths. A nice overview of the clinical and physiological implications on disrupted M-band bridges is given by Agarkova *et al.* [118]. For instance, the disruption might lead to elongation in the active state, also called eccentric contraction. In extreme cases, this eccentric contraction leads to irreparable disrupted sarcomeres, causing reduced muscle performance. This type of information allows us to design bottom-up type of experiments in which we know what the implication of disrupted M-bands are, which could then be tested and verified by SHG microscopy.

### **8.3.2 Muscle degradation assessment**

Due to the label-free capabilities of SHG microscopy, fresh muscle tissue can easily be imaged by this imaging technique. Yet, for several reasons, we mainly used PFA fixation followed by sucrose soaking for cryoprotection to prepare our samples. Due to strong cross-linking, PFA is known to optimally preserve tissue morphology which is of key essence when studying sarcomere regularity [146, 147]. PFA also leaves open the option for future staining steps, something that is not straight forward and requires additional steps when applying e.g. glutaraldehyde fixation[148]. Finally, we found our PFA fixation method was easy to apply, not labor intensive and quick.

These are all essential aspects when thinking of high throughput muscle degradation assessment as a future application of our work.

Label-free implies that the time-consuming staining steps required for fluorescence microscopy are avoided. For this, we know that specific staining of myosin is not straight forward as the antibodies and fluorescent dyes do not penetrate easily into the dense muscle tissue. Those few fluorophores that are specifically bound at their antigen are often rapidly bleached when imaging the samples. It is not impossible to perform the staining, but many optimization steps are required. Besides the label-free aspects, nanometer changes in the molecular arrangement of myosin filaments can be detected by SHG microscopy due to the coherent nature of the SHG process. Only by EM, filament disorder can be visualized and studied with greater detail than SHG microscopy. Yet, the high level of detail obtained by EM comes at the cost of time consuming sample preparation and extreme narrow field of view. Finally, the intrinsic confocal behavior of SHG microscopy allows for imaging only a thin optical section of a few hundreds of nanometers, and yield a slight higher resolution compared to for instance polarized light microscopy. More than other standardized imaging techniques, SHG microscopy of muscle tissue thus offers label-free, possibly high-throughput detection of subtle changes in myosin arrangements. This makes SHG a valuable complementary technique to be applied when studying myosin arrangements in striated muscle tissue.

Since SHG intensity profile analysis is based on a tedious manual profile selection, we sought to develop a fully automated analysis technique to obtain roughly the same information as obtained by the supra-molecular model, but then for the entire SHG image instead of just a few selected profiles. The analysis relies on estimating the apparent M-band length as a sarcomere regularity quantifier. The Gabor transform, a technique often used in signal processing and computer vision technology, proved to be appropriate for the automated analysis, yielding a sarcomere regularity quantifier that could be linked to the M-band size of the supra-molecular model. An additional normalization step allows for an easy-to-interpret quantifier ranging from 0 for complete disordered or irregular sarcomeres, to 1 for highly regular sarcomeres. Considering typical sarcomere irregularities, we gave meaning to all possible values over the full range. Finally, instead of looking at the full image, a histogram of the normalized Gabor values makes it even easier to compare sarcomere organization across experimental conditions.

The applicability of the Gabor analysis was only evaluated for the imaging conditions used in chapter 6. We know however that two features will affect the normalized Gabor values: the sarcomere length and the resolution. The base frequency of the analysis is related to the sarcomere lengths, and the Gabor analysis estimates the relative contribution of this base frequency to the SHG profile to score the sarcomere regularity. However, when longer sarcomeres are considered, the relative prevalence of the base frequency decreases, inducing a lower normalized Gabor value. This occurs because the thick filament length remains fixed, independent of the sarcom-

ere length. A similar explanation holds for the resolution. Increasing the resolution results in additional shoulder regions in the regular intensity profiles (see fig. 5.4), which are contained in higher harmonics. Again the relative contribution of the base frequency decreases, yielding a lower Gabor value. If the Gabor analysis is to be used as a clinical tool, the effects of sarcomere length and resolution need to be addressed. However, when working with a similar resolution as that in chapter 6, and considering sarcomeres in a relaxed state, the proposed approach will always yield reliable regularity scoring. Finally, assessment of alterations in sarcomere regularity due to differing physiological conditions should always be performed relative to a control group. This allows for mutual comparison of Gabor values, instead of considering them as absolute regularity quantifiers.

In chapter 7, we showed that the thickness of the sample plays a role in defining the SHG intensity profile, such that M-band length can not always be used to quantify sarcomere regularity. For thin samples, a regular sarcomere shows up as a double band pattern which, for the standard supra-molecular model, is typically characterized by an increased M-band length. Only when samples are sufficiently thick and the imaging is done away from the axial edges of the sample, the M-band length is useful as a regularity quantifier. We showed that for the used imaging parameters and the for selected sarcomere length, the minimal sample thickness is about 6  $\mu\text{m}$ . The samples used in chapter 5 and 6 were 14  $\mu\text{m}$  thick such that any size effect can be ruled out. Moreover, the images were taken near the axial center of the samples by placing the objective such that the SHG signal was maximal, ruling out the possible axial edge effects mentioned in chapter 7.

### **8.3.3 Point spread function**

For the chapters related to the muscle research, we measured the point spread function by imaging a set of sparsely distributed sub diffraction fluorescent beads on a cover glass using TPEF. The beads were fixed in a fixative with refractive index matching that of glass to limit the effect of the glass interfaces. Although this is a valid approach, our experimental values are larger than values calculated by the equations given by Zipfel *et al.* [50]. Larger than expected point spread function sizes are possibly related to system faults such as beam misalignment or insufficient beam divergence compensation, for instance resulting in a slanted PSF. Also spherical aberrations and Z-drift are known to affect the PSF.

## 8.4 Far field emission profile imaging

One of the most interesting consequences of coherency in SHG imaging is the far field emission profile. Depending on the imaged structure, the emission profiles will show distinct features which contain additional information, similar to *e.g.* an X-ray diffraction pattern of a crystal. However, interpreting these feature is difficult, and a lot of work needs to be done to decipher them. In yet another publication by Rouède *et al.* [137], the far field emission profile was used to reconstruct spatial sarcomere anomalies. Again, their firstly developed supra-molecular model served as a basis to predict the far field emission profiles for various types of sarcomere anomalies.

Here we propose another application in which the emission profile can be useful. It is based on the theory given in section 2.3.2. We derived the angular position of maximum intensity in the far field emission profile using two point sources, or scatterers, separated a distance  $d$  from each other. In the first order approximation of the Gouy phase shift (eq. (2.18)), the angle of maximum SHG intensity was independent of the distance between scatterers. However including the second order approximation, eq. (2.19) becomes

$$dk_{2\omega} \cos \theta \approx 2dk_{\omega} - 2 \left( \frac{d}{z_R} - \frac{d^3}{3z_R^3} \right) \quad (8.5)$$

such that, under the assumption of dispersionless media, the optimal emission angle is given by

$$\cos \theta = 1 - \frac{1}{z_R k_{\omega}} + \frac{d^2}{3k_{\omega} z_R^3}. \quad (8.6)$$

This shows that the optimal SHG emission angle depends on the distance between two scatterers. Inspection of the emission pattern can thus aid in measuring the density of scatterers, which might be applied in the muscle research to estimate the distance between myosin rods laying on a hexagonal lattice [149]. Yet, the effect is small: for a 1 nm change in a 10 nm unit cell, an angular change of only  $10^{-4}$  radians is expected when considering only two scatterers. Nevertheless, the approach based on the far field emission profiles does not rely on the SHG intensity, a parameter that hard to interpret as it depends on a lot of experimental variables such as sample opacity, laser power and detector gain. Moreover, by means of a modulation technique, combined with a lock-in detection scheme, the small changes could be amplified into a detectable range.

Finally, the far field emission profiles can be used to study the SHG related non-zero tensor elements, as shown in equation (2.45)-(2.47). Instead of interpreting the full emission profile, only the effect of the NA on the P-SHG intensity response can be used to study the contribution of various tensor elements to the signal. As was already stated, this approach can be used to study the validity of Kleinman symmetry for the considered materials.



---

## Reference list

---

1. Yount, L. *Antoni Van Leeuwenhoek: First to See Microscopic Life* (Enslow Publishers, 2008).
2. Coons, A. H., Creech, H. J. & Jones, R. N. Immunological Properties of an Antibody Containing a Fluorescent Group. *Exp. Biol. Med.* **47**, 200–202 (1941).
3. Wilson, T. & Sheppard, C. *Theory and Practice of Scanning Optical Microscopy* (Academic Press, London, 1984).
4. Sinha, R. P. & Hader, D.-P. UV-induced DNA damage and repair: a review. *Photochem. Photobiol. Sci.* **1**, 225–236 (4 2002).
5. Masters, B. R. & T.C.So, P. *Handbook of Biomedical Nonlinear Optical Microscopy* (Oxford University Press, 2008).
6. Boyd, R. W. *Nonlinear Optics* 3rd ed. (Elsevier inc., London, 2008).
7. Franken, P., Hill, A., Peters, C. & Weinreich, G. Generation of optical harmonics. *Phys. Rev. Lett.* **7**, 118–120 (1961).
8. Freund, I. & Deutsch, M. Second-harmonic microscopy of biological tissue. *Opt. Lett.* **11**, 94–96 (1986).
9. Tuer, A. E., Krouglov, S., Prent, N., Cisek, R., Sandkuijl, D., Yasufuku, K., Wilson, B. C. & Barzda, V. Nonlinear Optical Properties of Type I Collagen Fibers Studied by Polarization Dependent Second Harmonic Generation Microscopy. *J. Phys. Chem. B* **115**, 12759–12769 (2011).
10. Skubiszak, L & Kowalczyk, L. Myosin molecule packing within the vertebrate skeletal muscle thick filaments. A complete bipolar model. *Acta Biochim. Pol.* **49**, 829–40 (2002).
11. Fanton, Y., Robic, B., Rummens, J.-L., Daniëls, A., Windmolders, S., Willems, L., Jamaer, L., Dubois, J., Bijmens, E., Heuts, N., Notelaers, K., **Paesen, R.**, Ameloot, M., Mees, U., Bito, V., Declercq, J., Hensen, K., Koninckx, R. & Hendrikx, M. Cardiac atrial appendage stem cells engraft and differentiate into cardiomyocytes in vivo: A new tool for cardiac repair after MI. *Int. J. Cardiol.* **201**, 10–19 (2015).
12. Campagnola, P. J. & Loew, L. M. Second-harmonic imaging microscopy for visualizing biomolecular arrays in cells, tissues and organisms. *Nat. Biotechnol.* **21**, 1356–1360 (2003).
13. Psilodimitrakopoulos, S., Santos, S., Amat-Roldan, I., Mathew, M., Thayil K. N., A., Artigas, D. & Loza-Alvarez, P. Polarization dependant in vivo second harmonic generation imaging of *Caenorhabditis elegans* vulval, pharynx, and body wall muscles. *Proc. SPIE* **6860**, 686008–686008–10 (2008).

- 
14. Glas, D., **Paesen, R.**, Depuydt, D., Binnemans, K., Ameloot, M., De Vos, D. E. & Ameloot, R. Cellulose Amorphization by Swelling in Ionic Liquid/Water Mixtures: A Combined Macroscopic and Second-Harmonic Microscopy Study. *ChemSusChem* **8**, 82–86 (2014).
  15. Provenzano, P. P., Eliceiri, K. W. & Keely, P. J. Shining new light on 3D cell motility and the metastatic process. *Trends Cell Biol.* **19**, 638–648 (2009).
  16. Provenzano, P. P., Eliceiri, K. W., Yan, L., Ada-Nguema, A., Conklin, M. W., Inman, D. R. & Keely, P. J. Nonlinear Optical Imaging of Cellular Processes in Breast Cancer. *Microsc. Microanal.* **14**, 532–548 (2008).
  17. Brown, E., McKee, T., diTomaso, E., Pluen, A., Seed, B., Boucher, Y. & Jain, R. K. Dynamic imaging of collagen and its modulation in tumors in vivo using second-harmonic generation. *Nat. Med.* **9**, 796–800 (2003).
  18. Perentes, J. Y., McKee, T. D., Ley, C. D., Mathiew, H., Dawson, M., Padera, T. P., Munn, L. L., Jain, R. K. & Boucher, Y. In vivo imaging of extracellular matrix remodeling by tumor-associated fibroblasts. *Nat. Methods* **6**, 143–145 (2009).
  19. Han, X., Burke, R. M., Zettel, M. L., Tang, P. & Brown, E. B. Second harmonic properties of tumor collagen: determining the structural relationship between reactive stroma and healthy stroma. *Opt. Express* **16**, 1846–1859 (2008).
  20. Bruneel, B., Mathä, M., **Paesen, R.**, Ameloot, M., Weninger, W. & Huyseunne, A. Imaging the Zebrafish Dentition: From Traditional Approaches to Emerging Technologies. *Zebrafish* **12**, 1–10 (2015).
  21. Martens, T. F., Vercauteren, D., Forier, K., Deschout, H., Remaut, K., **Paesen, R.**, Ameloot, M., Engbersen, J. F., Demeester, J., De Smedt, S. C. & Braeckmans, K. Measuring the intravitreal mobility of nanomedicines with single-particle tracking microscopy. *Nanomedicine* **8**, 1955–1968 (2013).
  22. Su, P.-J., Chen, W.-L., Li, T.-H., Chou, C.-K., Chen, T.-H., Ho, Y.-Y., Huang, C.-H., Chang, S.-J., Huang, Y.-Y., Lee, H.-S. & Dong, C.-Y. The discrimination of type I and type II collagen and the label-free imaging of engineered cartilage tissue. *Biomaterials* **31**, 9415–9421 (2010).
  23. Psilodimitrakopoulos, S., Artigas, D., Soria, G., Amat-Roldan, I., Planas, A. M. & Loza-Alvarez, P. Quantitative discrimination between endogenous SHG sources in mammalian tissue, based on their polarization response. *Opt. Express* **17**, 10168–10176 (2009).
  24. Psilodimitrakopoulos, S., Loza-Alvarez, P. & Artigas, D. Fast monitoring of in-vivo conformational changes in myosin using single scan polarization-SHG microscopy. *Biomed. Opt. Express* **5**, 4362–4373 (2014).
-

25. Redon, S., Massin, J., Pouvreau, S., Meulenaere, E. D., Clays, K., Queneau, Y., Andraud, C., Girard-Egrot, A., Bretonnière, Y. & Chambert, S. Red Emitting Neutral Fluorescent Glycoconjugates for Membrane Optical Imaging. *Bioconjug. Chem.* **25**, 773–787 (2014).
26. De Meulenaere, E., Asselberghs, I., de Wergifosse, M., Botek, E., Spaepen, S., Champagne, B., Vanderleyden, J. & Clays, K. Second-order nonlinear optical properties of fluorescent proteins for second-harmonic imaging. *J. Mater. Chem.* **19**, 7514–7519 (2009).
27. De Meulenaere, E., De Wergifosse, M., Botek, E., Spaepen, S., Champagne, B., Vanderleyden, J. & Clays, K. Nonlinear optical properties of mStrawberry and mCherry for second harmonic imaging. *J. Nonlinear Opt. Phys. Mater.* **19**, 1–13 (2010).
28. De Meulenaere, E., Chen, W.-Q., Van Cleuvenbergen, S., Zheng, M.-L., Psilodimitrakopoulos, S., **Paesen, R.**, Taymans, J.-M., Ameloot, M., Vanderleyden, J., Loza-Alvarez, P., Duan, X.-M. & Clays, K. Molecular engineering of chromophores for combined second-harmonic and two-photon fluorescence in cellular imaging. *Chem. Sci.* **3**, 984–995 (2012).
29. De Meulenaere, E., **Paesen, R.**, Psilodimitrakopoulos, S., Ameloot, M., Loza-Alvarez, P., Vanderleyden, J. & Clays, K. Probing live samples in second-harmonic generation microscopy using specific markers and fluorescent proteins. *Proc. SPIE* **8226**, 82263C–82263C–9 (2012).
30. Gomopoulos, N., Lütgebaucks, C., Sun, Q., Macias-Romero, C. & Roke, S. Label-free second harmonic and hyper Rayleigh scattering with high efficiency. *Opt. Express* **21**, 815–821 (2013).
31. Mertz, J. *Introduction to Optical Microscopy* (Roberts and Company Publishers, 2010).
32. Wilt, B. A., Burns, L. D., Wei Ho, E. T., Ghosh, K. K., Mukamel, E. A. & Schnitzer, M. J. Advances in Light Microscopy for Neuroscience. *Annu. Rev. Neurosci.* **32**, 435–506 (2009).
33. Theer, P., Denk, W., Sheves, M., Lewis, A. & Detwiler, P. B. Second-Harmonic Generation Imaging of Membrane Potential with Retinal Analogues. *Biophys. J.* **100**, 232–242 (2011).
34. Sacconi, L., D’Amico, M., Vanzi, F., Biagiotti, T., Antolini, R., Olivotto, M. & Pavone, F. S. Second-harmonic generation sensitivity to transmembrane potential in normal and tumor cells. *J. Biomed. Opt.* **10**, 024014 (2005).
35. Sacconi, L., Tolic-Norrelykke, I., D’Amico, M., Vanzi, F., Olivotto, M., Antolini, R. & Pavone, F. Cell imaging and manipulation by nonlinear optical microscopy. English. *Cell Biochem. Biophys.* **45**, 289–302 (2006).

- 
36. Rouède, D., Recher, G., Bellanger, J.-J., Lavault, M.-T., Schaub, E. & Tiaho, F. Modeling of Supramolecular Centrosymmetry Effect on Sarcomeric SHG Intensity Pattern of Skeletal Muscles. *Biophys. J.* **101**, 494–503 (2011).
  37. Deniset-Besseau, A., Duboisset, J., Benichou, E., Hache, F., Brevet, P.-F. & Schanne-Klein, M.-C. Measurement of the Second-Order Hyperpolarizability of the Collagen Triple Helix and Determination of Its Physical Origin. *J. Phys. Chem. B* **113**, 13437–13445 (2009).
  38. Stoller, P., Reiser, K. M., Celliers, P. M. & Rubenchik, A. M. Polarization-Modulated Second Harmonic Generation in Collagen. *Biophys. J.* **82**, 3330–3342 (2002).
  39. Su, P.-J., Chen, W.-L., Chen, Y.-F. & Dong, C.-Y. Determination of Collagen Nanostructure from Second-Order Susceptibility Tensor Analysis. *Biophys. J.* **100**, 2053–2062 (2011).
  40. *Advances in Gabor Analysis* (eds Feichtinger, H. G. & Strohmer, T.) (Birkhauser Boston, 2002).
  41. Mertz, J. Molecular photodynamics involved in multi-photon excitation fluorescence microscopy. English. *EPJ D* **3**, 53–66 (1998).
  42. Verbiest, T., Clays, K. & Rodriguez, V. *Second-order Nonlinear Optical Characterization Techniques: An Introduction* (Taylor & Francis, Boca Raton, 2009).
  43. LaComb, R., Nadiarnykh, O., Townsend, S. S. & Campagnola, P. J. Phase matching considerations in second harmonic generation from tissues: Effects on emission directionality, conversion efficiency and observed morphology. *Opt. Commun.* **281**, 1823–1832 (2008).
  44. **Paesen, R.**, Sanen, K., Smisdom, N., Michiels, L. & Ameloot, M. Polarization second harmonic generation by image correlation spectroscopy on collagen type I hydrogels. *Acta Biomater.* **10**, 2036–2042 (2014).
  45. Raub, C., Putnam, A., Tromberg, B. & George, S. Predicting bulk mechanical properties of cellularized collagen gels using multiphoton microscopy. *Acta Biomater.* **6**, 4657–4665 (2010).
  46. Raub, C. B., Unruh, J., Suresh, V., Krasieva, T., Lindmo, T., Gratton, E., Tromberg, B. J. & George, S. C. Image Correlation Spectroscopy of Multiphoton Images Correlates with Collagen Mechanical Properties. *Biophys. J.* **94**, 2361–2373 (2008).
  47. Robertson, C. & George, S. C. Theory and practical recommendations for autocorrelation-based image correlation spectroscopy. *J. Biomed. Opt.* **17**, 080801–1–080801–7 (2012).
  48. Abbe, E. Beiträge zur Theorie des Mikroskops und der mikroskopischen Wahrnehmung. German. *Archiv für mikroskopische Anatomie* **9**, 413–418 (1873).
-

49. Kolin, D. & Wiseman, P. Advances in Image Correlation Spectroscopy: Measuring Number Densities, Aggregation States, and Dynamics of Fluorescently labeled Macromolecules in Cells. English. *Cell Biochem. Biophys.* **49**, 141–164 (2007).
50. Zipfel, W. R., Williams, R. M. & Webb, W. W. Nonlinear magic: multiphoton microscopy in the biosciences. *Nat. Biotechnol.* **21**, 1369–1377 (2003).
51. Cox, G. *Optical Imaging Techniques in Cell Biology* (Taylor & Francis, Boca Raton, 2007).
52. Nowack, R. L. & Kainkaryam, S. M. The Gouy phase anomaly for harmonic and time-domain paraxial Gaussian beams. *Geophysical Journal International* **184**, 965–973 (2011).
53. Piston, D. W. Choosing Objective Lenses: The Importance of Numerical Aperture and Magnification in Digital Optical Microscopy. *Biol. Bull.* **195**, 1–4 (1998).
54. Erikson, A., Örtengren, J., Hompland, T., de Lange Davies, C. & Lindgren, M. Quantification of the second-order nonlinear susceptibility of collagen I using a laser scanning microscope. *J. Biomed. Opt.* **12**, 044002 (2007).
55. *Photomultiplier tubes: Basics and applications* 3a. Hamamatsu Photonics K.K. (2007).
56. HJ, K., D, B., R, U. & SW, H. Ca<sup>2+</sup> fluorescence imaging with pico- and femtosecond two-photon excitation: signal and photodamage. *Biophys. J.* **77**, 2226–2236 (1999).
57. Yew, E. & Sheppard, C. Effects of axial field components on second harmonic generation microscopy. *Opt. Express* **14**, 1167–1174 (2006).
58. Asatryan, A. A., Sheppard, C. J. R. & de Sterke, C. M. Vector treatment of second-harmonic generation produced by tightly focused vignetted Gaussian beams. *J. Opt. Soc. Am. B* **21**, 2206–2212 (2004).
59. Gusachenko, I., Latour, G. & Schanne-Klein, M.-C. Polarization-resolved Second Harmonic microscopy in anisotropic thick tissues. *Opt. Express* **18**, 19339–19352 (2010).
60. Bancelin, S., AimãĈÂŕ, C., Gusachenko, I., Kowalczuk, L., Latour, G., Coradin, T. & Schanne-Klein, M.-C. Determination of collagen fibril size via absolute measurements of second-harmonic generation signals. *Nat Commun* **5**, – (Sept. 2014).
61. Psilodimitrakopoulos, S., Amat-Roldan, I., Loza-Alvarez, P. & Artigas, D. Estimating the helical pitch angle of amylopectin in starch using polarization second harmonic generation microscopy. *Journal of Optics* **12**, 084007 (2010).

- 
62. Chang, Y., Chen, C., Chen, J., Jin, Y. & Deng, X. Theoretical simulation study of linearly polarized light on microscopic second-harmonic generation in collagen type I. *J. Biomed. Opt.* **14**, 044016 (2009).
  63. Plotnikov, S. V., Millard, A. C., Campagnola, P. J. & Mohler, W. A. Characterization of the Myosin-Based Source for Second-Harmonic Generation from Muscle Sarcomeres. *Biophys. J.* **90**, 693–703 (2006).
  64. Dailey, C. A., Burke, B. J. & Simpson, G. J. The general failure of Kleinman symmetry in practical nonlinear optical applications. *Chem. Phys. Lett.* **390**, 8–13 (2004).
  65. Zoumi, A., Yeh, A. & Tromberg, B. J. Imaging cells and extracellular matrix in vivo by using second-harmonic generation and two-photon excited fluorescence. *Proc. Natl. Acad. Sci. U. S. A.* **99**, 11014–11019 (2002).
  66. Nikolenko, V., Nemet, B. & Yuste, R. A two-photon and second-harmonic microscope. *Methods* **30**. Visualizing neural networks, 3–15 (2003).
  67. Chou, C.-K., Chen, W.-L., Fwu, P. T., Lin, S.-J., Lee, H.-S. & Dong, C.-Y. Polarization ellipticity compensation in polarization second-harmonic generation microscopy without specimen rotation. *J. Biomed. Opt.* **13**, 014005 (2008).
  68. Amat-Roldan, I., Psilodimitrakopoulos, S., Loza-Alvarez, P. & Artigas, D. Fast image analysis in polarization SHG microscopy. *Opt. Express* **18**, 17209–17219 (2010).
  69. Discher, D. E., Janmey, P. & Wang, Y.-I. Tissue Cells Feel and Respond to the Stiffness of Their Substrate. *Science* **310**, 1139–1143 (2005).
  70. Buxboim, A., Ivanovska, I. L. & Discher, D. E. Matrix elasticity, cytoskeletal forces and physics of the nucleus: how deeply do cells ‘feel’ outside and in? *J. Cell Sci.* **123**, 297–308 (2010).
  71. Lo, C.-M., Wang, H.-B., Dembo, M. & Wang, Y.-I. Cell Movement Is Guided by the Rigidity of the Substrate. *Biophys. J.* **79**, 144–152 (2000).
  72. Hunt, N. & Grover, L. Cell encapsulation using biopolymer gels for regenerative medicine. English. *Biotechnol. Lett.* **32**, 733–742 (2010).
  73. Abreu, E. L., Palmer, M. P. & Murray, M. M. Collagen density significantly affects the functional properties of an engineered provisional scaffold. *J. Biomed. Mater. Res.* **93A**, 150–157 (2010).
  74. Kniazeva, E., Weidling, J. W., Singh, R., Botvinick, E. L., Digman, M. A., Gratton, E. & Putnam, A. J. Quantification of local matrix deformations and mechanical properties during capillary morphogenesis in 3D. *Integr. Biol.* **4**, 431–439 (4 2012).

75. Carey, S. P., Kraning-Rush, C. M., Williams, R. M. & Reinhart-King, C. A. Biophysical control of invasive tumor cell behavior by extracellular matrix microarchitecture. *Biomaterials* **33**, 4157–4165 (2012).
76. Bayan, C., Levitt, J. M., Miller, E., Kaplan, D. & Georgakoudi, I. Fully automated, quantitative, noninvasive assessment of collagen fiber content and organization in thick collagen gels. *J. Appl. Phys.* **105**, 102042 (2009).
77. Eichhorn, S. J. & Sampson, W. W. Statistical geometry of pores and statistics of porous nanofibrous assemblies. *Journal of The Royal Society Interface* **2**, 309–318 (2005).
78. Mir, S. M., Baggett, B. & Utzinger, U. The efficacy of image correlation spectroscopy for characterization of the extracellular matrix. *Biomed. Opt. Express* **3**, 215–224 (2012).
79. Hess, S. T. & Webb, W. W. Focal Volume Optics and Experimental Artifacts in Confocal Fluorescence Correlation Spectroscopy. *Biophys. J.* **83**, 2300–2317 (2002).
80. Thompson, N. in *Topics in Fluorescence Spectroscopy* (ed Lakowicz, J.) 337–378 (Springer US, 2002).
81. Koppel, D. E. Statistical accuracy in fluorescence correlation spectroscopy. *Phys. Rev. A* **10**, 1938–1945 (6 1974).
82. Friess, W. Collagen – biomaterial for drug delivery. *Eur. J. Pharm. Biopharm.* **45**, 113–136 (1998).
83. Tiaho, F., Recher, G. & Rouède, D. Estimation of helical angles of myosin and collagen by second harmonic generation imaging microscopy. *Opt. Express* **15**, 12286–12295 (2007).
84. Ghazaryan, A., Tsai, H. F., Hayrapetyan, G., Chen, W.-L., Chen, Y.-F., Jeong, M. Y., Kim, C.-S., Chen, S.-J. & Dong, C.-Y. Analysis of collagen fiber domain organization by Fourier second harmonic generation microscopy. *J. Biomed. Opt.* **18**, 031105 (2012).
85. Slenders, E., vandeVen, M., Hooyberghs, J. & Ameloot, M. Coherent intensity fluctuation model for autocorrelation imaging spectroscopy with higher harmonic generating point scatterers—a comprehensive theoretical study. *Phys. Chem. Chem. Phys.* **17**, 18937–18943 (29 2015).
86. Stoller, P., Celliers, P. M., Reiser, K. M. & Rubenchik, A. M. Quantitative Second-Harmonic Generation Microscopy in Collagen. *Appl. Opt.* **42**, 5209–5219 (2003).
87. Nadiarnykh, O. & Campagnola, P. J. Retention of polarization signatures in SHG microscopy of scattering tissues through optical clearing. *Opt. Express* **17**, 5794–5806 (2009).

- 
88. Psilodimitrakopoulos, S., Petegnief, V., Soria, G., Amat-Roldan, I., Artigas, D., Planas, A. M. & Loza-Alvarez, P. Estimation of the effective orientation of the SHG source in primary cortical neurons. *Opt. Express* **17**, 14418–14425 (2009).
  89. Kwan, A. C., Dombeck, D. A. & Webb, W. W. Polarized microtubule arrays in apical dendrites and axons. *Proc. Natl. Acad. Sci. U. S. A.* **105**, 11370–11375 (2008).
  90. Nucciottia, V., Stringarib, C., Sacconib, L., Vanzib, F., Fusia, L., Linaria, M., Piazzesia, G., Lombardia, V. & Pavone, F. S. Probing myosin structural conformation in vivo by second-harmonic generation microscopy. *Proc. Natl. Acad. Sci.* **107**, 7763–7768 (2010).
  91. Recher, G., Rouède, D., Richard, P., Simon, A., Bellanger, J.-J. & Tiaho, F. Three distinct sarcomeric patterns of skeletal muscle revealed by SHG and TPEF Microscopy. *Opt. Express* **17**, 19763–19777 (2009).
  92. *The Sarcomere and Skeletal Muscle Disease* (ed Laing, N. G.) (Springer, New York, 2008).
  93. Liu, W., Raben, N. & Ralston, E. Quantitative evaluation of skeletal muscle defects in second harmonic generation images. *J. Biomed. Opt.* **18**, 026005–026005 (2013).
  94. Taub, P. R., Ramirez-Sanchez, I., Ciaraldi, T. P., Gonzalez-Basurto, S., Coral-Vazquez, R., Perkins, G., Hogan, M., Maisel, A. S., Henry, R. R., Ceballos, G. & Villarreal, F. Perturbations in skeletal muscle sarcomere structure in patients with heart failure and Type 2 diabetes: restorative effects of (–)-epicatechinrich cocoa. *Clin. Sci.* **125**, 383–389 (2013).
  95. Garbe, C. S., Buttgerit, A., Schürmann, S. & Friedrich, O. Automated Multiscale Morphometry of Muscle Disease From Second Harmonic Generation Microscopy Using Tensor-Based Image Processing. *IEEE Trans. Biomed. Engineering* **59**, 39–44 (2012).
  96. Garcia-Canadilla, P., Gonzalez-Tendero, A., Iruretagoyena, I., Crispi, F., Torre, I., Amat-Roldan, I., Bijmens, B. H. & Gratacos, E. Automated cardiac sarcomere analysis from second harmonic generation images. *J. Biomed. Opt.* **19**, 056010 (2014).
  97. Odin, C., Guilbert, T., Alkilani, A., Boryskina, O. P., Fleury, V. & Grand, Y. L. Collagen and myosin characterization by orientation field second harmonic microscopy. *Opt. Express* **16**, 16151–16165 (2008).
  98. Boulesteix, T., Beaurepaire, E., Sauviat, M.-P. & Schanne-Klein, M.-C. Second-harmonic microscopy of unstained living cardiacmyocytes: measurements of sarcomere length with 20-nm accuracy. *Opt. Lett.* **29**, 2031–2033 (2004).

99. Squire, J. General model of myosin filament structure: III. Molecular packing arrangements in myosin filaments. *J. Mol. Biol.* **77**, 291–323 (1973).
100. Sjöström, M. & Squire, J. M. Fine structure of the A-band in cryo-sections: The structure of the A-band of human skeletal muscle fibres from ultra-thin cryo-sections negatively stained. *J. Mol. Biol.* **109**, 49–68 (1977).
101. Dirckx, J. J. J., Kuypers, L. C. & Decraemer, W. F. Refractive index of tissue measured with confocal microscopy. *J. Biomed. Opt.* **10**, 044014 (2005).
102. Vo-Dinh, T. *Biomedical Photonics Handbook* (CRC Press, Boca Raton, FL, 2003).
103. Bashkatov, A. N., Genina, E. A. & Tuchin, v. V. Optical properties of skin, subcutaneous, and muscle tissues: a review. *Journal of Innovative Optical Health Sciences* **04**, 9–38 (2011).
104. Ratan, V. *Handbook of Human Physiology* (Jaypee Brothers, Medical Publishers, New Delhi, 2004).
105. Knight, P., Erickson, M., Rodgers, M., Beer, M. & Wiggins, J. Distribution of mass within native thick filaments of vertebrate skeletal muscle. *J. Mol. Biol.* **189**, 167–177 (1986).
106. Schürmann, S., von Wegner, F., Fink, R. H., Friedrich, O. & Vogel, M. Second Harmonic Generation Microscopy Probes Different States of Motor Protein Interaction in Myofibrils. *Biophys. J.* **99**, 1842–1851 (2010).
107. Rouède, D., Bellanger, J.-J., Schaub, E., Recher, G. & Tiaho, F. Theoretical and Experimental SHG Angular Intensity Patterns from Healthy and Proteolysed Muscles. *Biophys. J.* **104**, 1959–1968 (2013).
108. Craig, R. & Offer, G. Axial arrangement of crossbridges in thick filaments of vertebrate skeletal muscle. *J. Mol. Biol.* **102**, 325–332 (1976).
109. Burkholder, T. & Lieber, R. Sarcomere length operating range of vertebrate muscles during movement. *J. Exp. Biol.* **204**, 1529–1536 (2001).
110. Miller, M. S., Dambacher, C. M., Knowles, A. F., Braddock, J. M., Farman, G. P., Irving, T. C., Swank, D. M., Bernstein, S. I. & Maughan, D. W. Alternative S2 Hinge Regions of the Myosin Rod Affect Myofibrillar Structure and Myosin Kinetics. *Biophys. J.* **96**, 4132–4143.
111. Gotthardt, M., Hammer, R. E., Hübner, N., Monti, J., Witt, C. C., McNabb, M., Richardson, J. A., Granzier, H., Labeit, S. & Herz, J. Conditional Expression of Mutant M-line Titins Results in Cardiomyopathy with Altered Sarcomere Structure. *J. Biol. Chem.* **278**, 6059–6065 (2003).
112. Sosa, H., Popp, D., Ouyang, G. & Huxley, H. Ultrastructure of skeletal muscle fibers studied by a plunge quick freezing method: myofilament lengths. *Biophys. J.* **67**, 283–292 (1994).

- 
113. Udd, B. Molecular biology of distal muscular dystrophies - Sarcomeric proteins on top. *Biochim. Biophys. Acta - Mol. Basis. Dis.* **1772**, 145–158 (2007).
  114. Sanoudou, D. & Beggs, A. H. Clinical and genetic heterogeneity in nemaline myopathy – a disease of skeletal muscle thin filaments. *Trends Mol. Med.* **7**, 362–368 (2001).
  115. Fukunaga, T., Miyatani, M., Tachi, M., Kouzaki, M., Kawakami, Y. & Kanehisa, H. Muscle volume is a major determinant of joint torque in humans. *Acta Physiol. Scand.* **172**, 249–255 (2001).
  116. Moss, B., Refsnes, P., Abildgaard, A., Nicolaysen, K & Jensen, J. Effects of maximal effort strength training with different loads on dynamic strength, cross-sectional area, load-power and load-velocity relationships. *Eur. J. Appl. Physiol. Occup. Physiol.* **75**, 193–9 (1997).
  117. Wilson, S. M. & Bacic, A. Preparation of plant cells for transmission electron microscopy to optimize immunogold labeling of carbohydrate and protein epitopes. *Nat. Protocols* **7**, 1716–1727 (2012).
  118. Agarkova, I., Ehler, E., Lange, S., Schoenauer, R. & Perriard, J.-C. M-band: a safeguard for sarcomere stability? English. *J. Muscle Res. Cell Motil.* **24**, 191–203 (2003).
  119. Lange, S., Agarkova, I., Perriard, J.-C. & Ehler, E. The sarcomeric M-band during development and in disease. English. *J. Muscle Res. Cell Motil.* **26**, 375–379 (2005).
  120. Grigorescu, S., Petkov, N. & Kruiyinga, P. Comparison of texture features based on Gabor filters. *IEEE Trans. Image Process.* **11**, 1160–1167 (2002).
  121. Pothos, V. K., Theoharatos, C. & Economou, G. A local spectral distribution approach to face recognition. *Comput. Vis. Image Und.* **116**, 663–675 (2012).
  122. Subbanna, N., Precup, D., Collins, D. & Arbel, T. Hierarchical Probabilistic Gabor and MRF Segmentation of Brain Tumours in MRI Volumes. *Medical Image Computing and Computer-Assisted Intervention. Lecture Notes in Computer Science* **8149** (eds Mori, K., Sakuma, I., Sato, Y., Barillot, C. & Navab, N.) 751–758 (2013).
  123. Furlan, R., Cuomo, C. & Martino, G. English. in *Neural Cell Transplantation* (eds Gordon, D. & Scolding, N. J.) 157–173 (Humana Press, 2009).
  124. Ng, A. V., Miller, R. G., Gelinas, D. & Kent-Braun, J. A. Functional relationships of central and peripheral muscle alterations in multiple sclerosis. *Muscle Nerve* **29**, 843–852 (2004).
  125. Kent-Braun, J. A., Ng, A. V., Castro, M., Weiner, M. W., Gelinas, D., Dudley, G. A. & Miller, R. G. Strength, skeletal muscle composition, and enzyme activity in multiple sclerosis. *J. Appl. Physiol.* **83**, 1998–2004 (1997).
-

126. Urso, M. L. Disuse Atrophy of Human Skeletal Muscle: Cell Signaling and Potential Interventions. *Med. Sci. Sports Exerc.* **41**, – (2009).
127. Heslinga, J., te Kronnie, G. & Huijing, P. Growth and immobilization effects on sarcomeres: a comparison between gastrocnemius and soleus muscles of the adult rat. English. *Eur. J. Appl. Physiol.* **70**, 49–57 (1995).
128. Bogie, J., Stinissen, P., Hellings, N. & Hendriks, J. Myelin-phagocytosing macrophages modulate autoreactive T cell proliferation. English. *J. Neuroinflammation* **8** (2011).
129. Lee, T. S. Image Representation Using 2D Gabor Wavelets. *IEEE Trans. Pattern Anal. Mach. Intell.* **18**, 959–971 (Oct. 1996).
130. Inoué, S. & Spring, K. R. *Video Microscopy: The Fundamentals (The Language of Science)* (Plenum, New York, 1997).
131. Burkholder, T. & Lieber, R. Sarcomere length operating range of vertebrate muscles during movement. *J. Exp. Biol.* **204**, 1529–1536 (2001).
132. Braun, T. P., Zhu, X., Szumowski, M., Scott, G. D., Grossberg, A. J., Levasseur, P. R., Graham, K., Khan, S., Damaraju, S., Colmers, W. F., Baracos, V. E. & Marks, D. L. Central nervous system inflammation induces muscle atrophy via activation of the hypothalamic–pituitary–adrenal axis. *J. Exp. Med.* **208**, 2449–2463 (2011).
133. Zorzella-Pezavento, S. F. G., Chiuso-Minicucci, F., França, T. G. D., Ishikawa, L. L. W., da Rosa, L. C., Marques, C., Ikoma, M. R. V. & Sartori, A. Persistent Inflammation in the CNS during Chronic EAE Despite Local Absence of IL-17 Production. *Mediators Inflamm.* **2013**, 10 (2013).
134. Hooper, S. L., Hobbs, K. H. & Thuma, J. B. Invertebrate muscles: Thin and thick filament structure; molecular basis of contraction and its regulation, catch and asynchronous muscle. *Prog. Neurobiol.* **86**, 72–127 (2008).
135. Llewellyn, M. E., Barretto, R. P. J., Delp, S. L. & Schnitzer, M. J. Minimally invasive high-speed imaging of sarcomere contractile dynamics in mice and humans. *Nature* **454**, 784–788 (2008).
136. Cromie, M. J., Sanchez, G. N., Schnitzer, M. J. & Delp, S. L. Sarcomere lengths in human extensor carpi radialis brevis measured by microendoscopy. *Muscle Nerve* **48**, 286–292 (2013).
137. Rouède, D., Bellanger, J.-J., Recher, G. & Tiaho, F. Study of the effect of myofibrillar misalignment on the sarcomeric SHG intensity pattern. *Opt. Express* **21**, 11404–11414 (2013).
138. Stevens, A., Doedens, G. & Lowe, J. *Histologie van de mens* (Bohn Stafleu Van Loghum, Houten).

- 
139. Shukla, P. *Regulatory Mechanism in Vertebrates* (Rastogi Publications, New Delhi).
  140. Zoghbi, M., Bolaños, P., Villalba-Galea, C., Marcano, A., Hernández, E., Fill, M. & Escobar, A. Spatial Ca<sup>2+</sup> Distribution in Contracting Skeletal and Cardiac Muscle Cells. *Biophys. J.* **78**, 164–173 (2000).
  141. Canale, E., Campbell, G., Smolich, J. & Campbell, J. *Cardiac Muscle* (Springer Berlin Heidelberg, 1986).
  142. Georgiou, M., Bunting, S. C., Davies, H. A., Loughlin, A. J., Golding, J. P. & Phillips, J. B. Engineered neural tissue for peripheral nerve repair. *Biomaterials* **34**, 7335–7343 (2013).
  143. Martens, W., Sanen, K., Georgiou, M., Struys, T., Bronckaers, A., Ameloot, M., Phillips, J. & Lambrechts, I. Human dental pulp stem cells can differentiate into Schwann cells and promote and guide neurite outgrowth in an aligned tissue-engineered collagen construct in vitro. *The FASEB Journal* **28**, 1634–1643 (2014).
  144. Sanen, K., **Paesen, R.**, Luyck, S., Phillips, J., Lambrechts, I., Martens, W. & Ameloot, M. Label-free mapping of microstructural organisation in self-aligning cellular collagen hydrogels using image correlation spectroscopy. *Acta Biomater.* **30**, 258–264 (2016).
  145. Luther, P. K., Munro, P. M. & Squire, J. M. Three-dimensional structure of the vertebrate muscle A-band. *J. Mol. Biol.* **151**, 703–730 (1981).
  146. Matsuda, Y., Fujii, T., Suzuki, T., Yamahatsu, K., Kawahara, K., Teduka, K., Kawamoto, Y., Yamamoto, T., Ishiwata, T. & Naito, Z. Comparison of Fixation Methods for Preservation of Morphology, RNAs, and Proteins From Paraffin-Embedded Human Cancer Cell-Implanted Mouse Models. *Journal of Histochemistry and Cytochemistry* **59**, 68–75 (Sept. 2010).
  147. Paavilainen, L., Edvinsson, A., Asplund, A., Hober, S., Kampf, C., Pontén, F. & Wester, K. The Impact of Tissue Fixatives on Morphology and Antibody-based Protein Profiling in Tissues and Cells. *Journal of Histochemistry and Cytochemistry* **58**, 237–246 (Oct. 2009).
  148. Tagliaferro, P., Tandler, C., Ramos, A., Saavedra, J. P. & Brusco, A. Immunofluorescence and glutaraldehyde fixation. A new procedure based on the Schiff-quenching method. *Journal of Neuroscience Methods* **77**, 191–197 (1997).
  149. Millman, B. M. The Filament Lattice of Striated Muscle. *Physiol. Rev.* **78**, 359–391 (1998).
-



---

## **Samenvatting**

---

Microscopie gebaseerd op het principe van *second harmonic generation* (SHG), of opwekking van de tweede harmonische, is een techniek die verwant is aan fluorescentiemicroscopie wanneer het toegepast wordt in het kader van biologisch onderzoek. Het basisprincipe van beide microscopietechnieken is het visualiseren van specifieke structuren met een zeer sterk contrast doordat het gegenereerde signaal een verschillende golflengte heeft dan die van de belichting. Daar waar fluorescentie vooral gebaseerd is op het inbrengen van fluorescente stoffen die eenduidig gebonden worden op de moleculaire structuur waarin men geïnteresseerd is, berust het SHG fenomeen op intrinsieke symmetrie-eigenschappen van een eerder beperkt aantal biologische structuren zoals bijvoorbeeld collageen, myosine, tubuline, amylopectine of cellulose. De biologische structuren waarop SHG microscopie werd toegepast in dit werk zijn voornamelijk type I collageen, en myosine dat aanwezig is binnen gestreept spierweefsel.

Sinds de introductie van SHG microscopie op biologisch weefsel is er reeds veel onderzoek gebeurd waarbij specifieke structuren voornamelijk morfologisch onderzocht werden. Dit is dikwijls een eerste en eenvoudige aanpak wanneer SHG microscopie wordt toegepast. Maar door het beperkt aantal biologische structuren die de capaciteit bezitten tot SHG, botst men al snel op één van de limieten van deze techniek. Een volgende stap in het toepassen van SHG microscopie is het bestuderen van de moleculaire eigenschappen. Dit gebeurt doorgaans door het opstellen van fysische en biofysische modellen van de onderzochte moleculaire structuren. Daarbij wordt onder meer de ruimtelijke verdeling in rekening gebracht, maar ook de gevolgen van het veranderen van de polarisatie van de belichtingslaser op het SHG signaal worden bestudeerd. In dit werk hebben we een bijdrage geleverd aan dit soort onderzoek, met het oog op de toepassing van de bestaande modellen in een biologische en biomedische context. Hiervoor hebben we de toepasbaarheid van die modellen getoetst voor gerichte biologische doelstellingen, en indien nodig uitgebreid en gekoppeld aan geautomatiseerde analysealgoritmes voor een snelle en eenduidige dataverwerking.

In **hoofdstuk 1** wordt in een algemene introductie een kader geschept voor het gedane onderzoek en de gebruikte technieken in dit werk. In **hoofdstuk 2** wordt de theoretische basis gegeven waarop het voorgestelde werk, en de bestaande biofysische SHG modellen berusten. Bovendien worden er enkele berekeningen getoond die verder niet gebruikt worden in dit werk, maar eerder dienen als een referentie voor verder onderzoek. In **hoofdstuk 3** geven we een beschrijving van het gebruikte microscopiesysteem, samen met de aanpassingen die van belang waren om ons onderzoek uit te voeren.

Het werk dat verricht werd in verband met collageen type I structuren wordt toegelicht in **hoofdstuk 4**. De doelstelling in dit hoofdstuk was het karakteriseren van hydrogelen gemaakt van collageen type I op basis van SHG beelden van zo een hydrogel. Een collageen type I hydrogel bestaat uit een verzameling van allemaal willekeurig georiënteerde collageenfibrillen. Afhankelijk van de dichtheid

---

en de willekeurigheid van die fibrillen, heeft de hydrogel unieke mechanische eigenschappen die van belang zijn voor de ontwikkeling en het gedrag van ingebrachte biologische cellen. Omdat het gaat over willekeuren structuren, en omwille van de bestaande expertise van de onderzoeksgroep, hebben we gebruik gemaakt van beeldcorrelatietechnieken waardoor een beeld op een statistische wijze geanalyseerd kan worden. Aangezien de bestaande correlatietechnieken telkens gebaseerd zijn op puntbronnen, hebben we een nieuw theoretisch model geïntroduceerd waarbij draadachtige structuren in rekening gebracht worden.

In **hoofdstukken 5, 6 en 7** bespreken we de experimenten en resultaten betreffende ons SHG onderzoek op gestreepte spier structuren. Dit werk werd geïnitieerd door het zeer interessante supra-moleculaire SHG model voor skeletspieren, geïntroduceerd door Rouède *et al.* [36]. In dit model worden de ruimtelijke en moleculaire eigenschappen die een rol spelen bij de opbouw van het SHG signaal in rekening gebracht. Aangezien er werd gesuggereerd dat het model van waarde was bij het onderzoeken van sarcomeerdegradatie ten gevolge van een wanorde van myosinemoleculen binnen dikke filamenten, hebben we dit model willen toepassen om ziektegeïnduceerde spierdegradatie te onderzoeken. Maar, door de beperkte kennis van het model, waren we genoodzaakt eerst een grondig onderzoek te doen naar de toepasbaarheid ervan. Dit wordt toegelicht in **hoofdstuk 5**. Hier wordt het effect van de verandering van de brekingsindex tussen belichtings- en signaalgolflengtes bestudeerd, laten we zien wat het effect van hoge vergroting is op de intensiteitsprofielen, en bespreken we dat de manier waarop myosine moleculen geordend zijn binnen de dikke filamenten van sarcomeren een rol spelen bij signaalvorming. De voornaamste conclusie luidt dat de filamentlengtes bekomen door SHG microscopie in combinatie met het supra-moleculaire model niet rechtstreeks vergeleken kunnen worden met die van electronenmicroscopie, zoals nu gangbaar is in de literatuur. Zo is de A-band lengte bekomen bij SHG microscopie  $\sim 1.4\mu\text{m}$  in plaats van de welgekende  $\sim 1.6\mu\text{m}$  bekomen door electronenmicroscopie.

In **hoofdstuk 6** wordt een nieuwe, automatische beeldverwerkingstechniek geïntroduceerd om de regelmaat van sarcomeren binnen het spierstaal in kaart te brengen. Deze analyse is gebaseerd op een Gabortransformatie, en wordt gerelateerd aan de structurele informatie die bekomen kan worden met het model besproken in hoofdstuk 5. Het bijhorende algoritme om de beelden te analyseren wordt in detail besproken, en wordt toegepast op stalen afkomstig van dieren met verschillende gradaties van *experimental autoimmune encephalomyelitis* (EAE), een diermodel dat vaak gebruikt wordt bij onderzoek naar *multiple sclerosis*, en een ziekte die door verlamming een effect zou hebben op de sarcomeerstructuur van skeletspieren.

Als laatste, in **hoofdstuk 7**, hebben we het effect van de afmetingen van een spierstaal op de SHG intensiteitsprofielen bestudeerd. Hier bleek dat, naast de wanorde van myosine binnen het dikke filament zoals besproken in hoofdstuk 5, ook de dikte van het staal het intensiteitsprofiel doet veranderen. Dit betekent dat indien

## CHAPTER 8

---

de afmetingen van het staal te klein zijn, de analyse besproken in hoofdstuk 5 en 6 een vertekend beeld kan geven van de regelmaat van sarcomeren binnen het staal.

---

## **Scientific output**

---

**Publications**

- De Meulenaere, E., **Paesen, R.**, Psilodimitrakopoulos, S., Ameloot, M., Loza-Alvarez, P., Vanderleyden, J. & Clays, K. Probing live samples in second-harmonic generation microscopy using specific markers and fluorescent proteins. *Proc. SPIE* **8226**, 82263C–82263C–9 (2012)
- De Meulenaere, E., Chen, W.-Q., Van Cleuvenbergen, S., Zheng, M.-L., Psilodimitrakopoulos, S., **Paesen, R.**, Taymans, J.-M., Ameloot, M., Vanderleyden, J., Loza-Alvarez, P., Duan, X.-M. & Clays, K. Molecular engineering of chromophores for combined second-harmonic and two-photon fluorescence in cellular imaging. *Chem. Sci.* **3**, 984–995 (4 2012)
- Martens, T. F., Vercauteren, D., Forier, K., Deschout, H., Remaut, K., **R. Paesen**, Ameloot, M., Engbersen, J. F., Demeester, J., De Smedt, S. C. & Braeckmans, K. Measuring the intravitreal mobility of nanomedicines with single-particle tracking microscopy. *Nanomedicine* **8**, 1955–1968 (2013)
- Vanbel, M. K., **Paesen, R.**, Brulot, W., Vandendriessche, S., Asselberghs, I., Markey, K., Valvekens, P., van der Veen, M., Vos, D. D., Ameloot, M., Valev, V. K., Locquet, J.-P. & Verbiest, T. Fast Fourier-Transform Second-Harmonic Generation (FFT-SHG) Provides a Solution for Measuring Nonlinear Effects on Fragile Structures. *Frontiers in Optics 2013*, FTu2F.5 (2013)
- Swinnen, N., Smolders, S., Avila, A., Notelaers, K., **Paesen, R.**, Ameloot, M., Brône, B., Legendre, P. & Rigo, J.-M. Complex invasion pattern of the cerebral cortex by microglial cells during development of the mouse embryo. *Glia* **61**, 150–163 (2013)
- Notelaers, K., Rocha, S., **Paesen, R.**, Swinnen, N., Vangindertael, J., Meier, J., Rigo, J.-M., Ameloot, M. & Hofkens, J. Membrane distribution of the glycine receptor  $\alpha 3$  studied by optical super-resolution microscopy. English. *Histochemistry and Cell Biology* **142**, 79–90 (2014)
- Notelaers, K., Rocha, S., **Paesen, R.**, Smisdom, N., Clercq, B. D., Meier, J. C., Rigo, J.-M., Hofkens, J. & Ameloot, M. Analysis of  $\alpha 3$  GlyR single particle tracking in the cell membrane. *BBA-Mol Cell Res* **1843**, 544–553 (2014)
- Paesen, R.**, Sanen, K., Smisdom, N., Michiels, L. & Ameloot, M. Polarization second harmonic generation by image correlation spectroscopy on collagen type I hydrogels. *Acta Biomater.* **10**, 2036–2042 (2014)
- Glas, D., **R. Paesen**, Depuydt, D., Binnemans, K., Ameloot, M., De Vos, D. E. & Ameloot, R. Cellulose Amorphization by Swelling in Ionic Liquid/Water Mixtures: A Combined Macroscopic and Second-Harmonic Microscopy Study. *ChemSusChem* **8**, 82–86 (2014)

- 
- Bruneel, B., Mathä, M, **Paesen, R.**, Ameloot, M., Weninger, W. & Huyseunne, A. Imaging the Zebrafish Dentition: From Traditional Approaches to Emerging Technologies. *Zebrafish* **12**, 1–10 (2015)
- Pirotte, N., Stevens, A.-S., Fraguas, S., Plusquin, M., Roten, A. V., Belleghem, F. V., **Paesen, R.**, Ameloot, M., Cebrià, F., Artois, T. & Smeets, K. Reactive Oxygen Species in Planarian Regeneration: An Upstream Necessity for Correct Patterning and Brain Formation. *Oxid Med Cell Longev* **2015**, 19 (2015)
- Paesen, R.**, Smolders, S., Notelaers, K., Wens, I., de Hoyos Vega, J. M., Eijnde, B. O., Hansen, D. & Ameloot, M. On the interpretation of second harmonic generation intensity profiles of striated muscle. *J. Biomed. Opt.* (2015)
- Sanen, K., **Paesen, R.**, Luyck, S., Phillips, J., Lambrichts, I., Martens, W. & Ameloot, M. Label-free mapping of microstructural organisation in self-aligning cellular collagen hydrogels using image correlation spectroscopy. *Acta Biomater.* **30**, 258–264 (2016)
- Fanton, Y., Robic, B., Rummens, J.-L., Daniëls, A., Windmolders, S., Willems, L., Jamaer, L., Dubois, J., Bijmens, E., Heuts, N., Notelaers, K., **Paesen, R.**, Ameloot, M., Mees, U., Bito, V., Declercq, J., Hensen, K., Koninckx, R. & Hendrik, M. Cardiac atrial appendage stem cells engraft and differentiate into cardiomyocytes in vivo: A new tool for cardiac repair after MI. *Int. J. Cardiol.* **201**, 10–19 (2015)
- Paesen, R.**, Smolders, S., de Hoyos Vega, J. M., Eijnde, B. O., Hansen, D. & Ameloot, M. Fully automated muscle quality assessment by Gabor filtering of SHG images. *J. Biomed. Opt.* **21**, 026003–1–026003–9 (2016)

**Selected oral presentations**

**Paesen, R.** & Ameloot, M. Polarization-SHG in microscopy. *Interuniversity Attraction Poles Meeting* **Leuven, Belgium** (2011)

**Paesen, R.** & Ameloot, M. Label-free characterization of materials by second harmonic generation. *Interuniversity Attraction Poles Meeting* **Ghent, Belgium** (2013)

**Paesen, R.** & Ameloot, M. Extra cellular matrix and cell metabolism studied by label-free microscopy. *VaRia Progress meeting* **Diepenbeek, Belgium** (2014)

**Selected poster presentations**

**Paesen, R.** & Ameloot, M. Applications of polarization second harmonic generation microscopy. *Joint autumn meeting BSCDB-BSM* **Antwerp, Belgium**. First poster prize (2011)

**Paesen, R.**, Sanen, K. & Ameloot, M. An improved model for image correlation spectroscopy analysis of collagen type I hydrogel images by second harmonic generation microscopy. *Focus On Microscopy* **Veldhoven, Netherlands** (2012)

**Paesen, R.**, Sanen, K., Smisdom, N., Michiels, L. & Ameloot, M. Studying cellular environments by image correlation spectroscopy. *Biomedica* **Aachen, Germany** (2013)

**Paesen, R.**, Smolders, S., de Hoyos Vega, J. M., Hansen, D. & Ameloot, M. Fully automated muscle quality assessment by Gabor analysis of second harmonic generation images. *International Microscopy Conference* **Prague, Czech Republic** (2014)

---

## **Dankwoord**

---

Een doctoraat doe je niet alleen. Om te beginnen moet er iets of iemand zijn die je de kans en de middelen geeft om je eigen onderzoek te kunnen verrichten. De dank voor het iets en de middelen gaat in mijn geval uit naar Universiteit Hasselt, de universiteit waar mijn academische carrière in 2005 begonnen is, en waar ze nu, 11 jaar later, eindigt. De unieke kans om onderzoek te doen heb ik gekregen van mijn promotor, prof. Marcel Ameloot, *waarvoor dank*. Terugkijkend naar het begin, durf ik voorzichtig te zeggen dat het onderwerp van deze thesis voor ons beide een sprong in het duister was. Na wat duw-, trek- en lobbywerk kwamen de lichtpuntjes pixel voor pixel tevoorschijn en kan ik me nu een contrastrijk beeld vormen wat we allemaal te weten zijn gekomen. Ook mijn co-promotor, prof. Dominique Hansen, wil ik *sterk* bedanken. Een *krachtig* deel van mijn werk is voortgevloeid uit uw voornaamste onderzoek. Ook de andere leden van jury, prof. Ivo Lambrichts, prof. Bert Brône, prof. Bart Cleuren, prof. Thierry Verbiest, Dr. Oleg Nadyarnykh en Dr. Marie-Claire Schanne-Klein, zou ik willen bedanken voor hun kritische blik en feedback, die mijn werk alleen maar ten goede zijn gekomen.

Een fysicus die in een biomedisch onderzoekscentrum terecht komt kan je gerust de vreemde eend in de bijt noemen. Maar al snel kwam ik erachter dat er fantastische mensen rondliepen, en nog altijd rondlopen, op BIOMED. Echte keien in hun vak, maar ook daarbuiten. Vaak heb ik te horen gekregen dat jullie *fysica stom vonden* of dat jullie *slecht waren in fysica*, maar zonder – denk ik – te beseffen dat ik het was die jullie nodig had, dat ik het was die moest kunnen rekenen op jullie kennis van jullie vak, zonder was het mij niet gelukt. Bedankt allemaal.

Natuurlijk zijn er een paar mensen die ik het bijzonder wil bedanken. Vaak heb ik het voorrecht gehad te kunnen discussiëren met enkele mensen waarvan ik soms het gevoel kreeg dat ze echt alles wisten van hun vak. Prof. Ivo Lambrichts, u wist me telkens te zeggen waar ik nu precies naar aan het kijken was. Ook prof. Luc Michiels, en prof. Virginie Bito, bedankt voor jullie interesse voor mijn werk, en interessante kijk op mijn werk. I would also like to thank prof. Ventislav Valev, for introducing me to some very interesting theories, for the *great days for science*, and your support. Verder wil ik ook prof. Maarten Roeffaers en Hans Van Oosterwyck bedanken voor hun hulp.

Onze groep, de leden van biofysica, jullie mag ik zeker niet vergeten. Te beginnen met de *anciens*, Nick en Ben, bedankt om mij wegwijs te maken binnen biofysica, in de kelder, in het donker. Ook Kristof, u zou ik nog net bij de anciens kunnen rekenen, bedankt voor de fantastische gesprekken tijdens onze koffiepauzes, zowel over ons werk als over het leven, soms diepgaand, en soms helemaal niet. Het streepje muziek deed soms deugd, en soms helemaal niet. Geef acht, generaal. Kathleen, de onvermoeibare Kathleen, bedankt om me zo vaak verder te helpen. Je bent me net vóór, maar hoe kan het ook anders. Tijd om de fakkel door te geven: Hannelore, Sarah en Eli, veel succes met jullie doctoraten, *doe dat goed!* And not to forget, our *itinerant* group members Mihaela and Daniël, and Rozhin, thanks for sharing your thoughts, but also your culture. Allemaal bedankt voor de leuke groepsfeer, de niet

---

te overtreffen team buildings en de legendarische spelletjesavonden.

Maar ik heb ook veel hulp gehad van collega's buiten onze groep. Hierbij denk ik vooral aan de fysiologen, met in het bijzonder Sophie. Heel erg bedankt om mij wegwijs te maken in de tientallen manieren die er zijn om een stukje spierweefsel te bewaren, te snijden, te kleuren, te benoemen, te bekijken, te labelen...noem maar op. Bedankt voor het geduld om het mij telkens opnieuw uit te leggen, in te springen als het nodig was, en samen die stagestudenten te begeleiden. Ook de stagestudenten zelf zou ik willen bedanken. Vooral Manolo, bergen werk heb je verzet tijdens je master thesis. Werk waar jij veel van geleerd heb, en waarvan ik de vruchten heb mogen plukken. Ook wil ik een paar mensen van REVAL bedanken. Inez, samen met Bert en Dominique heb jij gezorgd dat ik de nodige stalen kreeg. Ik mocht telkens mee op jullie kar springen, en mocht telkens meemaken hoe de immer goedlachse Frank zijn patiënten kon geruststellen om daarna te kunnen kijken wat voor vlees jullie in de kuip hadden. Niet zo zeer op wetenschappelijk vlak, maar wel voor de ontspannende middagen, wil ik Michel en Rik, en al hun vaste en sporadische bezoekers van *de G6* bedanken.

De vele, vele bezoekers die ik heb mogen verderhelpen, en die mij konden verderhelpen. Ik ga er waarschijnlijk een paar vergeten, maar ik ga toch een poging doen ze allemaal op te noemen. Als eerste is er Evelien, jij hebt me als ervaringsdeskundige als een van de eerste goed verder kunnen helpen met SHG microscopy. Bedankt daarvoor. Ik wens je een mooi vervolg van je academische carrière. Ik ben er zeker van dat je het allemaal klaar kan spelen. Ook Maarten Vanbel en zijn bende, Ward, Stefan...en telkens iemand anders waarvan ik me de namen niet meer kan herinneren (sorry). Het waren (h)eerlijke momenten aan de microscoop. Michiel Martens en Pieter Vanden Berghe, Thomas Martens en Kevin Braeckmans, Daan Glas en Dirk de Vos met Rob Ameloot, Bart Bruneel en Ann Huyseunne, Marc Muller, ook jullie bedankt voor jullie bijdragen.

Zoals eerder gezegd is mijn academische carrière begonnen in 2005. Dit was natuurlijk nooit mogelijk geweest mochten mijn ouders me de kans niet gegeven hebben om verder te studeren. Nooit eerder heb ik het jullie gezegd, ervan uitgaande dat jullie het wel wisten: bedankt hiervoor. En dan mijn liefste, mijn Sascha. Ik kan het niet beter verwoorden dan jou: al 13 jaar sta je aan mijn zijde. We hebben het allemaal samen gedaan: samen gestudeerd, samen gedoctoreerd, samen gegroeid, samen gedanst. Je kent mij door en door, en hebt me gesteund zoals alleen jij dat kan: Luisterend, stilzwijgend, met op het juiste moment dat ene juiste woord. Bedankt!

Rik





